3D Printing of Continuous Wire Polymer Composite for Mechanical and Thermal Applications

Yehia Ibrahim

A THESIS SUBMITTED TO

THE FACULTY OF GRADUATE STUDIES

IN PARTIAL FULFILLMENT OF THE REQUIREMENTS

FOR THE DEGREE OF

MASTER OF APPLIED SCIENCE

GRADUATE PROGRAM IN MECHANICAL ENGINEERING

YORK UNIVERSITY

TORONTO, ONTARIO

February 2019

Abstract

Recently, continuous fiber reinforcement has been combined with 3D printing techniques such as fused filament fabrication to create stronger and stiffer printed composite components. The continuous nature of the reinforcing material can improve both mechanical and thermal properties of the polymeric material significantly. However, several parameters can affect the printed composite properties such as filler volume fraction, type of polymer matrix and filler treatment.

The work presented in this study addresses the effect of reinforcing polymers with continuous metal wire on the composite's properties and the potential applications for these composites. In the first part of this study we presented a novel 3D printing technique in which metal wires were combined with polymer matrixes in order to improve both mechanical and thermal properties of the printed components. In the second part, we investigated the tensile and bending properties of the continuous wire polymer composites which was superior compared to the base polymer. In addition, we studied the effect of introducing continuous wires to the polymer matrix on the effective thermal conductivity which was found to increase significantly. In addition, we investigated the use of the fabricated composites as a novel fabrication technique for low-temperature heating elements and explored this technology for de-icing and anti-icing applications.

Acknowledgements

I wish to express my sincere appreciation to my supervisor Dr. Roger Kempers for accepting me into his research group, his valuable suggestions and support throughout this study. I would like to extend my appreciation to Dr. Garrett Melenka for his guidance, support and positive criticism. Furthermore to Prof. Alidad Amirfazli and Dr. Alex Czekanski for their technical expertise and resources.

I would like also to thank my wonderful wife and my parents for their great support, patience and encouragement. Many thanks to Ahmed Elkholy and my colleagues in TF-Lab for their support and the great time we spend together.

Notation

A_l	Equivalent area of a single layer
A_{eq}	Wires equivelant area,
A_w	Wires cross-sectional area
E_c	Tensile modulus of composite
E_w	Tensile modulus of metal wire
E_p	Tensile modulus of polymer
E_m	Tensile modulus of matrixes
H_l	layer height
I_l	Area moment of inertia of single layer
I	Area moment of inertia
I_c	Electric current
k	Thermal conductivity of the material in between the nodes.
k_c	Composite thermal conductivities
k_m	Matrix thermal conductivities
k_p	Polymer thermal conductivities
k_w	wire thermal conductivities
L	Wire length
L_D	Distance between two nodes
L_{th}	Thermal specimen thickness
M	bending moment
N	Number of printed layers

N^*	Number of rasters per layer
P	Bending load
P_{elec}	Dissipated power
Q	Measured input electric power to the primary heaters (P=IV)
q	Heat flux
R_c	Contact resistance
R_{Req}	Required wire resistance
R_{meas}	Measured thermal resistance
R_{th}	Thermal resistance
$R_{c,1}$	Contact resistance between the sample and the main heater
$R_{c,2}$	Contact resistance between the sample and the main cooler
T_{hot}	Primary heater temperature
T_{cold}	Primary cooler temperature
V	Supplied voltage
v_w	Wire volume fraction
v_p	Polymer volume fraction
v_{wp}	Wire volume fraction parallel to the heat flow direction
y	linear distance from the neutral axis
ΔT	Temperature difference between two nodes
ρ	Wire material resistivity
σ_f	Flexural stress at the beam's outer surface
σ_p	Ultimate tensile strength of polymer
σ_t	Ultimate tensile strength of composite

σ_w Ultimate tensile strength of metal wire

Table of Contents

List of Tables

List of Figures

Chapter 1 Introduction and Motivation

1.1. Polymer Composites, Advantages and Limitations

Composite materials have been the focus of considerable research for decades due to their superior mechanical characteristics such as tensile and shear properties and their wide range of applications [1]. The composition of the composite can be controlled by assigning different quantities of the constituents' materials. As an example, polymer composites consist of a polymer matrix to which a quantity of reinforcement material is added. This serves to improve the mechanical, thermal and electrical behavior of the composite beyond that of the constituent materials [2], [3], [4]. Often, one of the main benefits of composite polymers is increased rigidity and strength to an otherwise relatively flexible polymer matrix. Polymer composites have become popular for many applications due to their high-stiffness, high-strength, low-density, and relative ease of manufacture.

Additive manufacturing (AM) and 3D printing technologies such as stereolithography (SLA), poly-jet injection and laminated object manufacturing (LOM) have brought about a new dimension to polymer composites manufacturing. Among these polymers AM processes, fused filament fabrication (FFF) has become one of the most mainstream and commercially accessible 3D printing technologies in recent years due to its flexibility, low-cost hardware, and the large open-source development community. A wide range of thermoplastics can be printed using FFF and recent research has focused on developing polymer composites specifically for FFF feedstock [5], [6], with several commercial products recently available [7]. In addition, various kinds of composite filaments have been

developed with a range of volume fractions such as copper and iron [8], [9]. Chopped fibre reinforced filaments have also been used to improve the mechanical properties of the printed composites [10], [11]. More exotic materials like carbon nanotubes, graphene and diamond were also used as a filament filler [12], [13].

Generally, AM composites exhibit improved mechanical and structural behavior over pure polymer 3D printed components. However, often the limiting factor for further improvement in mechanical stiffness or effective thermal conductivity is the discontinuous nature of the filler materials and particles [14],[15].

To address this shortcoming, a particularly promising fabrication technique extrudes a continuous fibre along with the molten plastic to form directionally controllable continuous fibre composites. From a structural stand point, the continuous network ensures that the contribution of the fibres in the composite properties without being limited by the interfacial interaction between the fibres and the polymer. This will result in an increase in the mechanical properties of the printed components. From a thermal standpoint, the continuous network can act as a continuous thermally conductivity path for heat flow which aids the thermal conductivity of the composite.

Overcoming the structural and the thermal limitations of polymer composites increases their viability for use in different applications as well as the fabrication of more functionalized components. Moreover, 3D printing of continuous fibre polymer will offer more design flexibility and control over the fabricated components' properties.

1.2. Motivation of The Research

Additively manufacturing of lightweight, stiff and thermally conductive polymer composites are of great value in engineering applications for multiple reasons. Their favorable properties as well as the ease of manufacturing and the complexity of the fabricated products make these types of composites attractive for different industries such as automotive and electronic cooling applications. Specifically, polymer heat exchangers can make use of such kind of composite materials with high thermal conductivity which will improve their performance and efficiencies. Different continuous fibres and metal wires can be used to create this kind of materials. So far however, very limited types of continuous fibres have been explored from AM perspective so far; these include Polyacrylonitrile (PAN) carbon fibre, aramid and glass fibres. Furthermore, very little research has studied the effect of these fibres and wires on the thermal properties of the composites.

Oftentimes, 3D printing of continuous fibre polymer composites (CFPCs) involved the use of closed source printers with limited access to the fabrication parameters. The printing process can be improved to allow for more user accessibility and printing flexibility. The use of open source printer can also significantly reduce the total cost of the fabrication process.

Finally, 3D printed CFPCs have a great potential to be used in more than just mechanical and thermal property enhancement. The continuous fibre network can act as a sensory element for mechanical stresses, heat flux, temperature and other sensing. It can also be used as an active element to enable the fabrication of 3D printed structures with embedded

heating elements to be used in low temperature heating applications.

The present work investigates the mechanical and thermal properties of metal wires reinforced composites fabricated using a low-cost open source 3D printer. Further, it illustrates the potential of the fabricated continuous wire polymer composites (CWPCs) in different applications.

1.3. Objectives of The Research

This thesis addresses the development and characterization of continuous wire polymer composites (CWPCs) fabricated using fused filament 3D printing. The main objectives of this research were to:

(i) Surveying literature on polymer additive manufacturing (Chapter 2)

(ii) Develop the technologies and techniques of 3D printing CWPCs using accessible, low-cost 3D printing hardware (Chapter 3).

(iii) Characterize the tensile and flexural properties of 3D printed CWPCs and investigate the effect of matrix material, reinforcement volume fraction and wire surface roughness on the mechanical properties of CWPCs. (Chapter 4).

(iv) Explore the potential of using CWPCs as low-temperature heaters (Chapter 5).

(v) Characterize the effective thermal conductivity of CWPCs (Chapter 6).

1.4. Research Approach and Thesis Organization

The first step towards the achievement of the above-mentioned objectives was to adapt an open-source 3D printer to facilitate the fabrication of CWPCs. This is described in **Chapter 3** and was submitted as a peer reviewed paper under the name "Additive Manufacturing of Continuous Wire Polymer Composites" in *"Manufacturing letters Journal"* [16].

Tensile samples were printed afterwards with different wire materials and tested to characterize the tensile properties of CWPCs. Also, a design of experiment (DOE) study was made on flexural samples to investigate the effect of the matrix material, reinforcement volume fraction and wire surface roughness on the flexural properties of CWPCs. The tensile and bending studies are presented in **Chapter 4** and the results from these two were presented in peer reviewed papers under the names "Fabrication and Tensile Testing of 3D Printed Continuous Wire Polymer Composites" in *"Rapid Prototyping Journal"* [17] and "Flexural Properties of Continuous Wire Polymer Composites" in *"Materials Science and Technology Journal"* (under review)[18].

From an application standpoint, 3D printed heater panels were fabricated and tested for anti-icing applications to demonstrate the significance of using CWPCs as a low-temperature heater. The panels were field-tested in real-life conditions onboard a Norwegian coast guard ship sailing in the arctic circle. The effect of water loading on the ice formation was investigated as well as the effect of the use of a hydrophobic coating performance and energy consumption. This study is presented in **Chapter 5** and was submitted as a peer reviewed journal paper under the name "3D Printed Electro-Thermal Anti-Icing System for Composite Panels" in *"Cold Regions Science and Technology"* (under

review) [19].

Finally, similar to the mechanical properties, the thermal conductivity of CWPCs was investigated by fabricating and testing of thermal samples. The effect of printing direction, matrix material and reinforcement volume fraction on the thermal conductivity were modelled and characterized experimentally. The thermal study is presented in **Chapter 6** and it is under preparation for journal publication.

This body of work is summarized in **Chapter 7** which also discusses the future outlook for this research.

Chapter 2 Literature Review

2.1. Fused Filament Fabrication

Fabrication of polymer composites using additive manufacturing techniques such as 3D printing has recently gained interest due to the advantages that 3D printing introduces to the manufacturing process [20]. This includes ease of manufacturing, high precision and the ability to fabricate complex geometries. The addition of particles or fibres to the polymer matrix permits the fabrication of polymer matrix composites, which are characterized by high mechanical and thermal performance [20]. Fused Filament Fabrication (FFF) also known as Fused Deposition Modeling (FDM) is one of most commonly used techniques to 3D print polymeric material. It has also been used to fabricate polymer based composites by mixing the polymeric material with reinforcement prior to the filament fabrication process [21]. Other polymer Additive manufacturing techniques such as SLA, poly-jet injection and LOM are also available. However, FFF represents one of the cheapest and open source techniques.

2.2. 3D Printed Metal-Polymer Composites

Metal particles such as iron and copper were used as reinforcement for polymer matrixes such as acrylonitrile butadiene styrene (ABS) and nylon. The main objective of utilizing metal powder was to investigate their effect on the thermo-mechanical properties of the composite. Generally, the addition of metal filler particles with higher volume fraction results in higher tensile modulus, lower tensile stress and elongation. Due to the difference in the in thermal expansion coefficients between the metal particles and the polymer ($k_{Fe} \approx$

11.7 X 10^{-6}/°C, k_p ≈ 50-100 X 10^{-6}/°C), the polymer will tend to contract more after deposition causing de-bonding. This will result in crack propagation around the particle during mechanical loading [22]. Nevertheless, it can improve the thermal properties such as the heat capacity and the thermal conductivity of the composites. Nikzad *et al.* [8] found that adding iron particles with 10% volume fraction increased the storage modulus by nearly 40% and that the glass transition temperature of the composite was seven degrees higher. Also, they found that, the iron-ABS composite has significantly lower ultimate tensile strength (less than 50% of pure ABS). Masood *et al.* [22] found that increasing the volume fraction of iron particles in a nylon matrix will further decrease the tensile strength of the composite, In addition, with the same filler volume fraction, usage of smaller metal particles will result in lower ultimate tensile strength. In another study, they studied the effect of the metal particles size on the thermal conductivity. They found that adding 40% of fine iron particles results in a composite with five times higher thermal conductivity [23]. Hwang *et al.* [9] also filled an ABS matrix with iron and copper particles with different volume fractions. They found that both iron and copper particles addition result in a composite with lower tensile strength. At the same volume fraction, the copper-ABS composite was found to have lower tensile strength compared to iron-ABS composite.

2.3. 3D Printed Fibre-Polymer Composites

Fibre fillers are more commonly used with polymer composites since they have significantly higher mechanical properties which can improve the composite properties. In the form of chopped fibres, the filler can be easily mixed with the polymer to produce a printing feedstock. Different types of fibres such as carbon, Kevlar and glass were

implemented to improve both thermal and mechanical properties. Zhong *et al.* [10] used glass fibres with different volume fractions as the reinforcement material for ABS matrix. They found that adding glass fibres significantly improve the tensile properties of the composite as well as the composite brittleness. Ning *et al.* [24] investigated the effect of fused filament fabrication process parameters on the mechanical properties of carbon fibre-reinforced ABS composite. Through performing tensile testing, they found that printing parameters such as speed, temperature, printing angle and layer thickness can be optimized to maximum the tensile properties of carbon fibre reinforced polymer composites. Similarly, Ivey *et al.* [25] investigated the effect of post-printing annealing procedure on the mechanical properties of on the both pure PLA and carbon fibre reinforced PLA composite. As expected, they found that carbon fibre-reinforced PLA has higher elastic modulus and tensile strength. As well, annealing of the PLA and reinforced PLA samples caused an increase in crystallinity, up to a maximum value of 30%. Ferreira *et al.* [26] also investigated the tensile properties of commercial carbon fibre reinforced PLA composite for samples printed with different printing angles. They found that, failure in reinforced PLA happened at lower strains than in PLA, indicating that the reinforced material became more brittle with the addition of short carbon fibre.

2.4. Limitations of Discontinuous Fillers

For pure materials, fracture commonly happens when the material reaches its ultimate strength under static loading. For composites with discontinuous fillers, failure can be more complicated. Since the material is composed of different constituents, the failure will greatly depend on the material ability to distribute the load on its components. In such a

case, the interfacial bonding which defines the adhesion quality between the polymer and the filler plays a great role. If the bonding between the polymer and the discontinuous filler is not strong enough to transmit the stress, the filler material will pull out and the filler strength will not be transmitted to the matrix.

The bonding between the filler and the matrix can be experimentally measured using different techniques such as the fibre pull out test [27]–[29]. Many studies had been made to investigate different techniques to improve polymer-filler adhesion [30], [31]. Ramanathan *et al.* [32] investigated the surface state (acidic and basic surface oxides) of carbon fibres on the interfacial shear strength in an epoxy matrix. Kim *et al.* [31] coated carbon fibres with silica particles. They found that, the introduction of the silica surface coating improves the adhesive strength by approximately 20% while also reducing fibres surface fractures significantly by around 90%. Li *et al.* [31] treated carbon fibre surface with bacterial cellulose to improve its adhesion to the polymer. By performing tensile testing, they found that the process increases the surface roughness of the fibre and increases the composite ultimate strength.

From a thermal stand point, heat transfer in polymer composite is mainly caused by phonon transport [33]. This means that polymer-filler interfacial properties dominate the composite thermal properties, especially thermal conductivity. In addition, filler material, shape and surface treatment can enormously affect the effective thermal conductivity of the composite[34]. Fillers with high aspect ratio help creating bridges between adjacent particles which facilitate phonon and electron transport with the composite and subsequently increase the thermal conductivity [35]. Different types of fillers can also be

mixed together to bring the desired properties of each filler together[36].

The main limitations for improving the thermal conductivity using discontinuous filler arise from the existence of interfacial thermal resistance between the filler and the matrix. The thermal contact resistance is caused by phonon scattering and it has to be minimized to increase thermal conductivity [37], [38]. It can be analytically described using theoretical models such as the acoustic mismatch model [39]. In addition, few experimental methods can be used to determine its value for different materials [40].

Replacing the discontinuous filler with a continuous phase can offer a solution for the shortcomings of discontinuous filler composites. Although adding a continuous filler can create a non-homogeneous or anisotropic composite (especially if the filler is relativity large), the continuous network ensures that the filler will be participating in bearing the load. According to the Halphin-Tsai model [41], which can be used to predict the composite tensile properties, the continuous fiber will exert higher tensile properties with continuous fillers compared with aligned and random discontinuous fillers from the same material. This can be seen in Fig. 2-1 which shows a comparison between aligned and random continuous and discontinuous carbon fiber reinforced PLA matrix. At the same filler volume content (v_f), the aligned continuous filler shows the highest tensile modulus (E). Using continuous filler can also be useful in increasing the thermal conductivity as the existence of a crystalline material with free electrons will allow for more electron transport causing further improvement in the thermal conductivity. Also, there will be minimum phase transitions to impede heat transfer. With minimal contact resistance, higher thermal conductivity is expected.

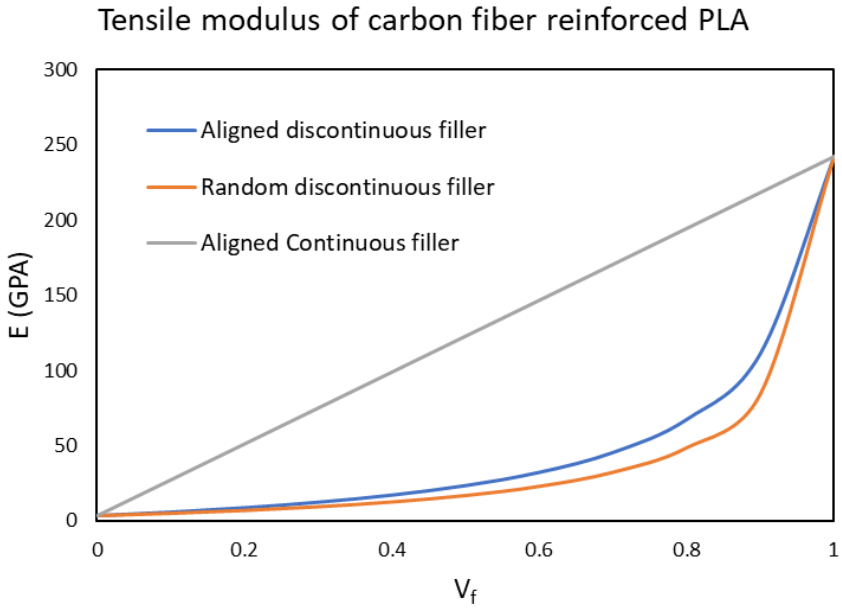

Figure 2-1 Tensile modulus in load direction of discontinuous and continuous carbon fiber filled PLA

2.5. 3D Printing of Continuous Fibre Polymer Composites

In the last few years, attention has been given towards introducing continuous filler networks into a polymer matrix aiming to improve the matrix mechanical performance. Recently, 3D printing techniques, specifically FFF, were used to achieve this task allowing for more shape complexity and design flexibility [42]–[44] . FFF 3D printing with continuous fillers/fibres can be categorized into two main categories. The first category is when a single nozzle is been used to print the fibre and the polymer matrix. In such case, usually the fibres are pre-coated with the polymer prior to printing to form a coated fibre filament. This fibre filament is then fed through the heat block to melt the polymer before extruding it through the printing nozzle. This type of printing does not allow for different filler percentage within the printed parts as the fibre and the polymer are printed together.

Prüß *et al.* [45] designed a novel printing head where the fibres were mixed with polymer inside the heat block just before printing. Li *et al.* [46] also used a single nozzle to mix the polymer with chemically pre-treated fibres. Hu *et al.* [47] used a coaxial coating mold to precoat the fibre filament and a modified 3D printer heat to print fibres with single nozzle. Vaneker [48] used one off-the-shelf commingled yarn of glass fibres and Polypropylene to fabricate a pre-coated fibre filament and used a modified open-source printer to print with.

The second category utilizes dual nozzles where one is used for the pre-coated fibres while the other is used for the polymer matrix. This printing technique is usually utilized with a cutting mechanism to ensure full control on the fibre location and direction independent of the polymer extrusion. Commercial fibre printers such as the Markforged MarkOne printers have adopted this technique in their printer [49]. The company offers few limited fibre and polymer filaments such as carbon, Kevlar and glass fibres and nylon and Onyx (nylon mixed with chopped carbon fibers) matrixes.

Since the usage of conventional 3D printers can only offer 3 axes movement which may limit the complexity of the fabricated structures, researchers were more interested in using robotic arms with 5 or 6 axes of freedom. Eichenhofer *et al.* [44] used a six axis robotic arm to print with continuous fibres by attaching a fibre processing head and a printing nozzle. This technique allowed for the fabrication of free handing fibre reinforced structures and more control over the fibre's locations in three dimensions. They further optimized their fibre printing head to reduce the residual void content of the printed extrudate by over 80% [51]. Hou *et al.* [52] also attached a fibre printing nozzle developed in previous study to a 6-axis arm to print fibre reinforced corrugated composite structures.

2.6. Mechanical and Thermal Properties of CFPCs

The impact of using continuous fibres in reinforcing 3D printed structures has been demonstrated in several studies which investigate the mechanical properties of CFPCs. The focus of these studies was mainly on examining the tensile and bending properties of CFPCs. Using one of commercial fibre printers, Melenka *et al.* [53] investigated the tensile properties of continuous Kevlar fibre-reinforced nylon printed with the MarkForged MarkOne 3D printer. The objective of the study was to evaluate the elastic properties of the fibre reinforced 3D printed structures with different fibre volume fractions. They used an volume average stiffness method to predict the elastic properties of the samples. Der Klift *et al.* [54] used the same printer to investigate the properties of carbon fibre reinforced samples. Dickson *et al.* [55] compared the performance of carbon, Kevlar and glass fibre reinforced samples. The mechanical properties of the composite were evaluated for both tensile and bending. They also investigated the influence of fibre orientation, fibre type and volume fraction on both properties. It was found that the carbon fibre reinforced samples yielded the largest increase in mechanical strength. Camineroa *et al.* [56] investigated the effect of impact damage on the CFPC structure integrity. The objective was to evaluate the effect of build direction and fibre volume fraction on impact performance of fibre reinforced composites. The results show that impact strength increases as fibre volume fraction increases in most cases.

The mechanical properties of CFPCs manufacture using modified open-source printers were also investigated excessively. Tian *et al.* [57] investigated the effect of printing parameter such as printing temperature, layer thickness and feeding rate on the properties

of carbon fibre reinforced CFPCs fabricated using a modified printer. They found that printing with higher temperature and smaller layer thickness creates samples with higher flexural strength. In a follow up study [58] , they recycled CFPCs parts by re-melting the printed part to extract a polymer coated fibre filament and re-print with it. They found that remanufactures parts have a 20% higher tensile strength due to improved interfacial properties of the fibres. Yang *et al.* [59] used the same modified printer to investigate the tensile properties of carbon fibre reinforced samples. Hu *et al.* [47] used another modified printer to examine the flexural properties of carbon fibre reinforced samples. They came up with a mathematical model of relationship between the printing parameter and the flexural strength by performing a design of experiment (DOE) study. Sugiyamaa *et al.* fabricated CFPCs structures with honeycomb, rhombus, rectangle, and circle core shapes as a single piece. They performed a flexural test to investigate the effect of core shape on the structure performance. Goh *et al.* [60] investigated the tensile, flexural, and quasi-static indentation characteristics of glass fibre reinforced samples. In addition, they studied the fracture behavior for the samples of each test using micro computed tomography.

2.7. Summary

The addition of discontinuous filler to a polymer matrix can improve its properties significantly. However, this improvement is limited by the interfacial properties of the polymer and the filler. Continuous fillers do not have this problem since they have a continuous network which preserve the reinforcement properties. This can help Improve both mechanical and thermal properties of the composite making it stiffer and more thermally conductive. Some possible candidates continuous fillers properties are

summarized in Table 2-1.

Table 2-1 Continuous filler materials properties [61]

Filler material	Tensile strength (MPa)	Tensile modulus (GPa)	Thermal conductivity (W/m.K)
PAN Carbon fiber	4137	242	8
Kevlar fibers	3000	112	0.04
Glass fibers	3310	68.9	-
Copper	210	110	398
Nickel-chromium	689	200	15

So far, 3D printed CFPCs have been studied from a mechanical standpoint where the mechanical properties investigation is the primary focus. However, 3D printed CFPCs have limited investigation from a thermal standpoint. We believe that these materials can be of great potential for thermal applications as well and this aspect requires in. In addition, metal fibres and continuous wires have not been utilized in these 3D printed continuous composites and they could potentially allow for improved thermal properties over conventional, discontinuous metal particle laden composite filaments. As such, in this study, we begin by presenting a novel manufacturing technique for CWPC which is believed to offer preferable mechanical and thermal properties.

Chapter 3 3D Printing of Continuous Wire Polymer Composites

An open-source 3D printer (Prusa mk3 i3, Prusa Research, Prague, Czech Republic) was modified to print various polymer materials with embedded continuous metal wires to create CWPC components. The original configuration of the 3D printer prior to modification is shown in Fig. 3-1.

The objective of the modification was to introduce the wire into the molten filament just prior to extrusion. The advantage of introducing the wire to the polymer using this method, instead of using pre-extruded wire-polymer composite filament, is the simplicity of the system and the compatibility with different nozzle diameters. In a wire-polymer filament the minimum nozzle diameter is limited to a value close to the filament diameter. Additionally, wires of different materials and diameters can easily be introduced using this process thus allowing for manipulation of the printed composite mechanical and thermal properties.

From a hardware standpoint, the main modifications consisted of a modified hotend design which allows for the metal wire to be introduced into the molten filament prior to extrusion and the relocation of the filament feeding system to accommodate this new hotend. Other aspects which were also addressed which enabled the fabrication of the CWPCs investigated here include the printing parameters, materials, wire diameters and printer control.

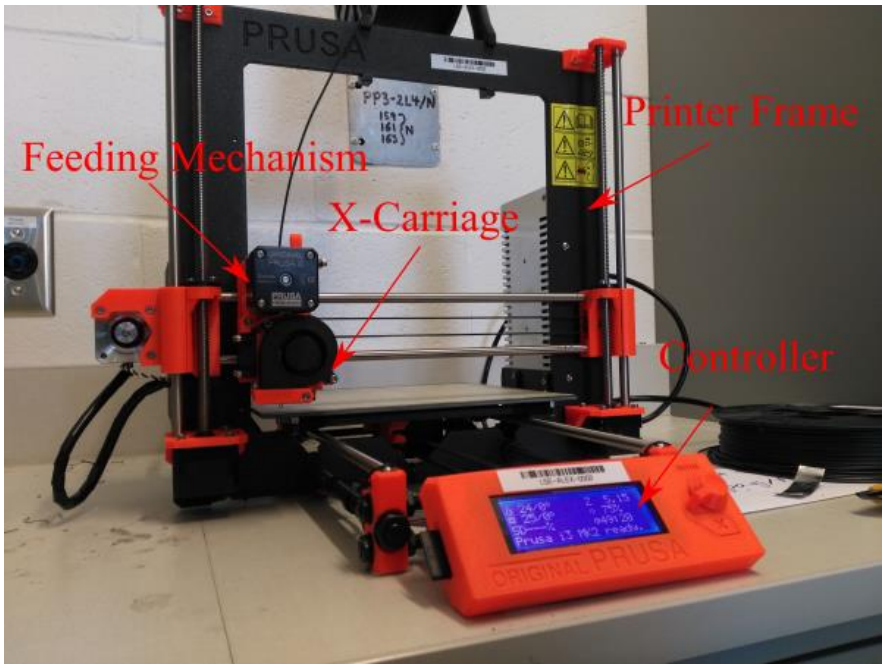

Figure 3-1 Prusa mk2 i3 original printer showing main components

3.1. Hotend and 3D Printer Modification

The hardware modification needed to enable the printing of CWPCs is alternative hotend design which introduces the metal wire to the molten filament prior to extrusion. A schematic of the modified hotend used here is shown in Fig. 3-2 and a section view and dimensions of the heater block are shown in Fig. 3-2 (Plane A). The 1.75 mm filament hotend inlet is altered from the standard 90° orientation to 45° to accommodate the inlet wire which enters the heat block perpendicular to the printing direction and in the center of the modified heater block (E3D -V6 All Metal Hotend, E3D Online, Oxford UK).

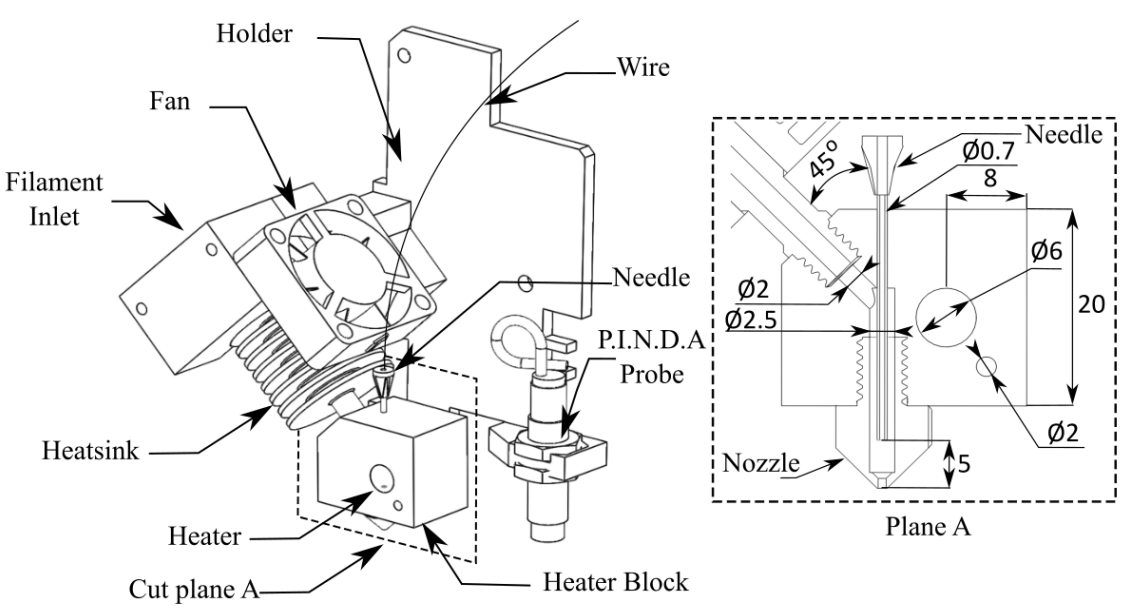

Figure 3-2 Schematic of modified hotend assembly showing critical dimensions

The wire is introduced to the molten filament using a 0.625 mm outer diameter and 0.425 mm inner diameter flat tip 23-gauge stainless steel dispensing needle (McMaster Carr, Ohio, USA) which is inserted into the top of the heater block as shown in Fig. 3-2. The feedstock is melted inside the heat block and meets the wire inside the brass nozzle. The needle tip is located 5 mm before the nozzle exit, as shown in Fig. 3-2 (Plane A), to minimize the polymer flow inside the needle which may cause needle blockage.

The modified heater block was machined from a block of aluminum for its relatively high thermal conductivity. Inside the block, a minimum flow area for the filament was ensured to avoid filament backflow and minimize the required feeding pressure. The filament flow section diameter was 2 mm for the first angled part of the block before meeting the needle and was then expanded to 2.5 mm in the vertical section when it meets the needle to take into account the volume the needle will occupy, as shown in Fig. 3-2. The heater and

thermistor locations were set as indicated in Fig. 3-2 to ensure good heat distribution and fast temperature response. An E3D -V6 standard brass nozzle with 1 mm ID was installed in the block using a standard M6 thread. The standard E3D-V6 heatsink was connected to the block with a 45^{o} tilting angle using an M6 thread.

A new hotend holder was designed to accommodate the new location of the heatsink. At the same time, the printer's standard 30x30 mm cooling fan was relocated, as shown in Fig. 3-2. The holder was designed on SolidWorks CAD software (SolidWorks 2017, Dassault Systems, Waltham, MA) and the output STL file was plugged into the Cura (Cura 2.6.0, Ultimaker, Netherlands) slicing software and printed with PLA.

The filament feeding mechanism was relocated to the printer's metal frame, as shown in Fig. 3-3. From there, filaments were fed into the hotend through a 3 mm ID PTFE tubing (McMaster Carr, Ohio, USA) which acted as a guide tube. A feeding mechanism for the wires was not necessary, as the already printed and cooled rasters adhere to the heated bed which exert enough traction force to pull the wire out of the hotend as the extrusion and printing occurs. The wires were hung above the printer to minimize the traction force needed to extrude them along with the molten filament.

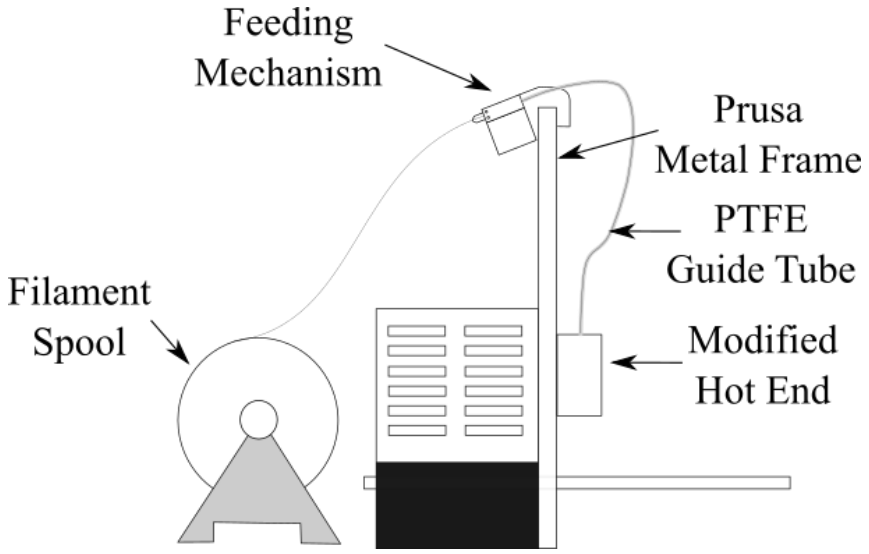

Figure 3-3 New location of the filament feeding mechanism

3.2. Printing Parameters

Experimentation demonstrated that printing parameter adjustment is critical when printing the embedded wires using a 1- or 0.6-mm nozzle. The wire enters the heater block (Fig. 3-2) at room temperature and is heated inside the needle. When the metal wire exits the nozzle, it conducts heat from the heater block through the wire and can potentially delay the cooling and solidification of the polymer matrix. This affect the wire adhesion to the polymer, most notably at the print corners. We speculate that the wire thermal conductivity influences the cooling of the printed part because as the thermal conductivity of the wire increases, more heat will be conducted to the printed component.

Print cooling was provided through two 40mm x 40mm 12v standard cooling fans which aided in the solidification process. The values for the printing parameters of PLA with continuous wire are summarized in Table 3-1. Adjustment of the nozzle affects printing

parameters such as the printing temperature and printing speed; further discussion of the nozzle diameter is presented below. A low printing speeds of 7 mm/s and up to 15 mm/s were found to be more suitable for larger nozzles, while a temperature greater than 190^{o}C caused PLA over-heating. Layer height is also important and should be adjusted according to the wire and nozzle diameters to ensure sufficient traction for the wire out of the nozzle. For this technique, two layer-heights of 0.6 mm and 0.4 mm were found to be the most convenient for printing with the 1- and 0.6 mm nozzles respectively. A range of extruder multiplier can be used to overlap adjacent rasters and ensure the good adhesion between the printed raster. The real amount of extruded material is calculated by multiplying the calculated amount of extruded material for a certain bath by the extrusion multiplier. In the default settings of the slicing software, the first layer height is typically less than the rest. This ensures the printed component adheres to the print heat-bed; however, in this study, the first layer height was set to be the same as the rest, due to the presence of the metal wire.

Table 3-1: Printing Parameters

Extruder Temp.	175-200	°C
Bed Temp.	55-60	°C
Printing Speed	7-15	mm/s
Nozzle Diameter	1 -0.6	mm
Extruder multiplier	1-1.1	
Wire diameter	0.075 -0.05	mm
Needle outer diameter	0.6	mm
Needle inner diameter	0.5	mm
Raster width	1.05- 0.65	mm
Layer Height	0.6- 0.4	mm
First layer height	0.6- 0.4	mm
Fill density	50 -100	%

3.3. Material, wire diameter and nozzle diameter

For most open-source printers, a wide range of filament materials such as ABS, PLA, Polyethylene Terephthalate Glycol (PETG) and nylon can be used, allowing for a range of material properties [62]. For printing with embedded wires, there is a wide range of metallic wires which are suitable for the reinforcement of CWPC, such as copper, nickel chromium, or steel. To allow for successful reinforcement of a 3D-printed structure, the wire should have suitable strength to withstand the force of the printer movement and the shearing friction within the needle. Wire surface roughness and filament material is anticipated to affect the adhesion between the metal reinforcing wires and the polymeric matrix as roughness on the wire surface will increase friction with the polymer. Additionally, adhesion between the continuous metallic wires and polymer matrix can be improved by including metal particles or chopped fibres within the polymer matrix [63] which will exert more friction with the wire and help the wire to adhere to the matrix.

One challenging aspect of the present fabrication technique is the wire diameter. As the wire diameter increases with same nozzle diameter, there is inadequate molten polymer to help advance the wire out of the nozzle. A variety of wire diameters were tested with different nozzle diameters and the results show that the preferred wire diameter is in the range one tenth of the nozzle diameter. Here, two wire diameters were tested, as shown in Fig. 3-4. The first wire diameter was 75μm with 1- and 0.6-mm nozzles which were tested at 0.6- and 0.4-mm layer height respectively (Fig. 3-4 (a)and (c)). The second wire diameter was 50 μm which was tested with 0.6 mm nozzle and 0.4 mm layer height (Fig. 3-4 (b)).

Experimentation showed that a wire diameter of around one-tenth of the printing nozzle is optimum for CWPCs printing. Commercially available wire materials were chosen for testing; nickel-chromium wire was selected for its higher modulus and strength, while copper wire was used for its moderate mechanical properties and higher thermal and electrical properties. PLA was used as the matrix material because of its moderate melting temperature and good thermal stability.

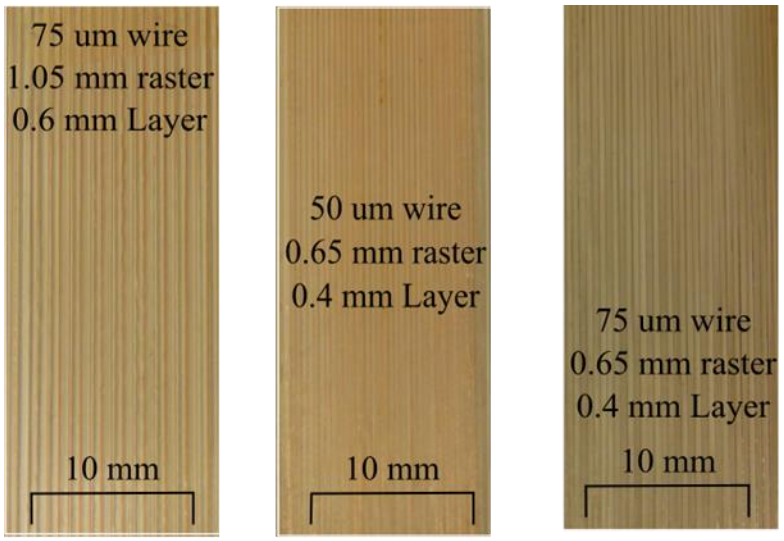

(a) (b) (c)

Figure 3-4 (a) 75 µm wire, 1.05 mm raster width and 0.6 mm layer height (b) 50 µm wire, 0.65 mm raster width and 0.4 mm layer height (c) 75 µm wire, 0.65 mm raster width and 0.4 mm layer height

3.4. Modification significance

The introduction of metal wires to the polymer matrix was expected to improve the mechanical and thermal properties when compared to conventional AM structures.

Additionally, due to the nature of AM structures the continuous wires can be oriented to align with the critical loading directions of the designed part. Alternating reinforcement direction as shown in Fig. 3-5 (a), (b) and (c) can result in a quasi-isotropic structure. This reinforcing technique is not limited to two- dimensional geometries. Many available 3D printing slicing programs have a printing mode known as "Vase Mode" which is ideal for producing thin tubular AM structures. The CWPC reinforcement method can be used while manufacturing components in "Vase Mode" resulting in helical reinforcement as shown in Fig. 3-6. This figure demonstrates that the wire reinforcement occurs around the circumferential direction of the AM structure. The ability to produce continuous axisymmetric components with the CWPC manufacturing method demonstrates the ability to orient wire reinforcement in the critical loading direction of tubular components which will greatly increase the hoop strength of the AM structures allowing for improved performance in radial pressure loading cases.

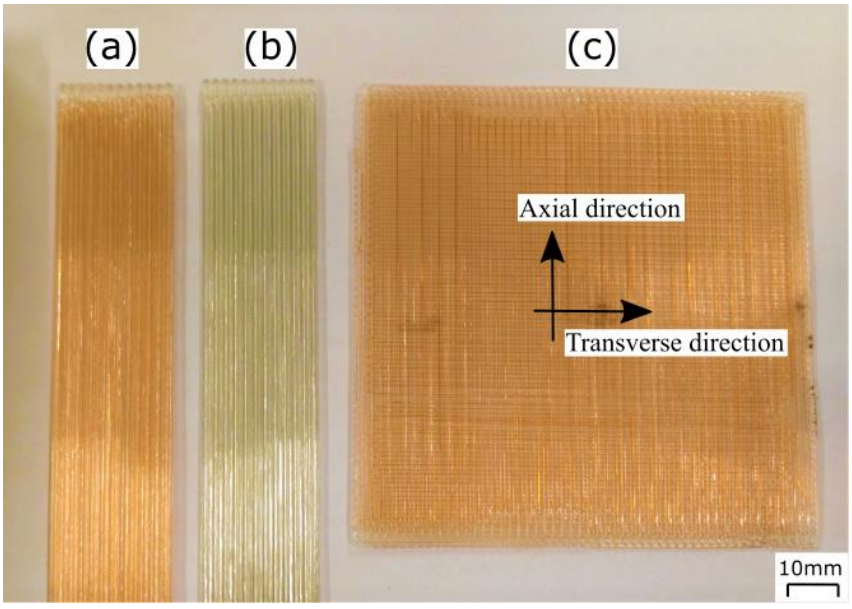

Figure 3-5 CWPC samples (a) Unidirectional copper reinforced sample with axial

reinforcing wires (b) nickel-chromium wire reinforced sample with axial reinforcing wires. (c) copper wire reinforced sample with alternating axial and transverse wire reinforcement.

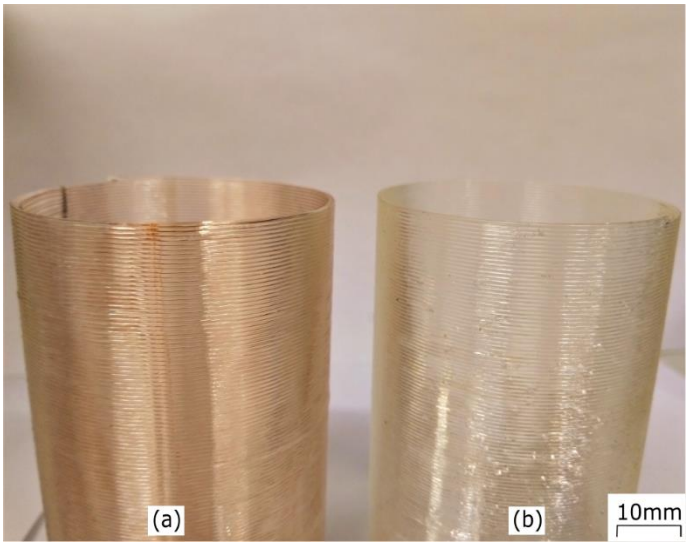

Figure 3-6 3D printed geometries created using “Vase Mode” (a) Wire reinforced and (b) non-reinforced structure.

Chapter 4 Investigation of Tensile and Bending Properties CWPCs

This chapter is dedicated for the investigation of the mechanical properties of CWPCs. Two studies were made to achieve this purpose. In the first study we investigated the tensile properties of copper and nickel-chromium wires reinforced samples printed with different volume fractions. In addition, we initially investigated the effect of the matrix on the tensile properties by changing the used PLA matrix into a copper filled PLA matrix. In the second study, we investigated in more detail the effect of wire volume fraction, matrix material and wire surface roughness on the flexural properties of CWPCs by performing a design of experiment study. Furthermore, the CWPC mechanical performance was modelled analytically using solid mechanics models and compared to the experimental data.

4.1. Investigation of Tensile Properties

To investigate the mechanical properties of wire reinforced composites, we performed a tension test to obtain the tensile properties. Samples with different wire materials and reinforcement volume fraction were tested to investigate the effect of these parameters on the tensile properties. In addition, the composite performance was predicted analytically using a rule of mixture solid mechanics model. The obtained experimental results were then compared to the analytical model prediction.

4.1.1 Tensile Samples Fabrication

To test CWPCs under tensile loading, 18 samples were manufactured. The samples'

geometry, shown in Fig 4-1 (a), were fabricated according to (ASTM D3039 -14, 2014; i.e., standard test method for tensile properties of polymer matrix composite materials) recommendations [64]. Dimensions of the manufactured samples are shown in Table 4-1. A unidirectional 200 mm-long sample was created with 1.8 mm thickness made from three equal layer heights (0.6 mm). All samples were printed with 100% infill and with zero-degree raster printing angle. Two wire materials were used in this study to examine the effect of varying metal wire reinforcement on mechanical properties. Six rectangular samples of non-reinforced PLA were printed using a G-code generated by MATLAB to avoid rasters' overrun which is usually associated with the typical slicing software. Six samples of PLA with continuous copper wire and six samples reinforced with continuous nickel-chromium wire were printed for tensile testing; these are shown in Fig. 4-1 (b).

(a)

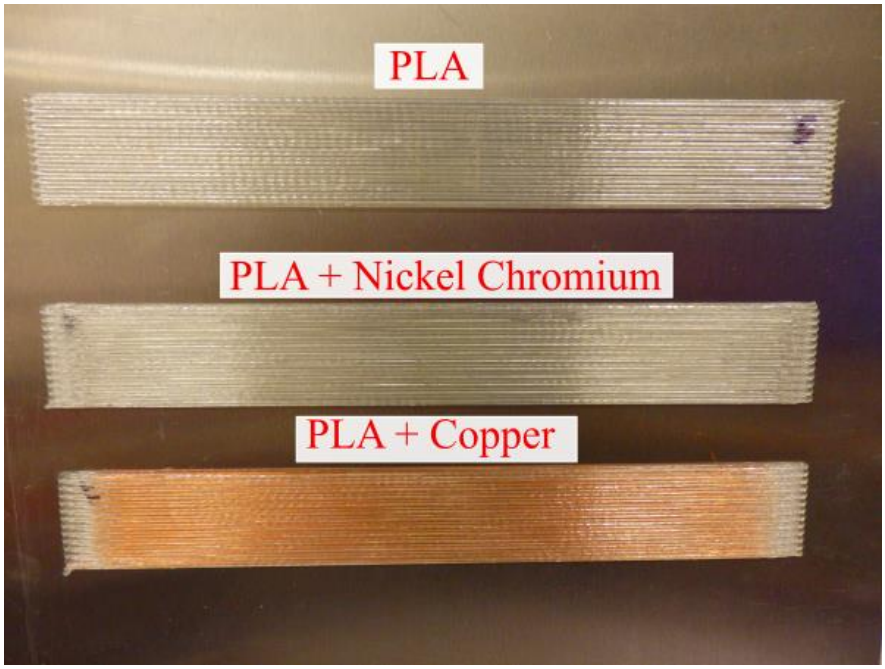

(b)

Figure 4-1 (a) CWPC sample schematic, L= 200 mm, W= 25 mm, T =1.8 mm, b) from top to bottom: Unidirectional PLA, PLA with nickel chromium wire, PLA with copper wire

Table 4-1: Specimen Dimensions

Length (L)	200	mm
Width (W)	25	mm
Thickness (T)	1.8	mm
Printing Angle	0	°
Number of layers	3	
Number of rasters /layers	25	

4.1.2 Sample Preparation and Testing

4.1.2.1 Physical Measurements

Physical measurements of all fabricated samples were collected. For tensile properties, the

sample cross section area significantly affects the prediction of the material properties. Five measurements for width and thickness were taken using a 6.35 mm flat anvil micrometer (Mitutoyo, Canada) for each sample at different positions. Based on these measurements, an average cross section area was calculated and used in stress calculation and model prediction.

4.1.2.2 Tensile Testing apparatus

For tensile testing of the printed samples, once again ASTM D3039-14 standard recommendations regarding samples' dimensions and loading rates were followed. The test was conducted using a universal test frame (MTS Criterion Model 43, Eden Prairie, MN USA) with a load cell of 10 kN maximum load, as shown in Fig. 4-2 (a). To ensure correct sample mounting on the machine, self-alignment grips were used. For measuring the samples' strain, a laser extensometer (LX500 laser extensometer, MTS, Eden Prairie, MN) was used with standard reflective tapes on the samples. A constant head speed test was used with a displacement rate of 0.013 mm/s to achieve nearly constant strain rate in the gauge section; failure occurred in less than 10 minutes, as per the ASTM D3039 standard. A close-up of the test sample, test grips and reflective tape used with the laser extensometer are shown in Fig. 4-2 (b).

Rectangular-shaped samples are more sensitive to stress concentration areas generated by the grips which increase the probability of the fracture occurring in the gripping zone. In addition, the smooth surface of the samples resulted in the sample slipping from the grips. To overcome these two problems, stainless steel rectangular tabs of 50 mm length, 25 mm width and 0.6 mm thickness were utilized. The tabs were bonded to the samples using a

polymercaptan epoxy with an amine curing agent (Speed Set Epoxy, LEPAGE, Canada). A two-sided sandpaper sheet was placed between the sample and the grips to minimize sample slipping. The use of end tabs and sandpaper is recommended in the ASTM D3039 standard to mitigate sample slipping.

(a) (b)

Figure 4-2 (a) Tensile strength test configuration with laser extensometer, (b) close-up of tensile sample showing reflective tape

4.1.2.3 Microscopic Preparation

The microstructure of the CWPC was examined after printing. Printed samples were embedded in a cold curing resin (Amazing clear cast, Alumilite Corp, USA) and allowed to cure for 24 hours within a 27-mm diameter cylindrical holder. The samples were then cut into 15 mm-long cylinders using a high-speed abrasive cutting machine (Mecatome T260, PRESI, Hungary). Next, a sequential polishing method was used to prepare the sample surface. The samples were ground gradually for two minutes on each side using water as a

coolant to minimize the smearing effect and produce a smooth surface. Four stages of grinding were used: 180-grit, 240-grit, 400-grit and 600-grit silicon carbide papers. After the 600-grit grind, the surface was prepared for polishing. There was one polishing stage where a 1 μm Alumina polishing powder was used for five minutes with water as coolant. A grinding and polishing machine (StarGrind™ 200-2V, Microstar 2000, Canada) was used with a 300-rpm rotating speed.

Using a stereo-microscope (LEICA MZ10 F, LEICA, Germany), multiple images for samples cross-sectioned with different magnification were taken after adjusting the scale of the microscope with a 0.01 mm scale. The pictures were then imported to open-source image processing software (ImageJ, National Institutes of Health, Bethesda, Maryland, USA) for measurements. The scale was set, the threshold adjusted, and the pictures were analysed in order to get an accurate area fraction which also represents the volume fraction as all the constituents have the same length. An average size of wire was measured and subtracted from the areas where the wire and air voids intersected to get the actual air voids' volume fractions.

4.1.2.4 Modulus calculation

For each sample, the values for the load-extension testing were used to calculate the values of stress and strain based on the measured average area of each sample. The modulus of tested samples was calculated based on the tensile chord modulus calculations in (4-1), where the slope of the stress strain curve was calculated between two strain points per as ASTM- D3039-14 Table 3 recommendations. This is given as

$$E_c = \Delta\sigma/\Delta\varepsilon \quad (4\text{-}1)$$

The difference in the applied stress values ($\Delta\sigma$) is measured at the two strain points of 0.001 and 0.003 absolute strain, and $\Delta\varepsilon$ is the difference between the two strain points (nominally 0.002).

4.1.3 Analytical Modelling

Due to the composite nature of this structure, the mechanical properties were examined experimentally and analytically. Since this is a polymer matrix reinforced with continuous wires, the structure that is formed classically resembles a composite material and the rule of mixture analytical model was used to evaluate these values [41]. Similar behavior was observed by Melenka *et al.* [53] for continuous Kevlar fibre reinforced structures. To predict the modulus of elasticity for the CWPCs, the properties of the wire used should be well known. Typical values for the modulus and ultimate strength of copper and nickel-chromium wires are shown in Table 4-2 [61].

Table 4-2 Assumed mechanical properties of copper and nickel-chromium wires [61]

Material Properties		
Material	Modulus (E) (GPa)	Ultimate Strength (σ) (MPa)
PLA	3.6	37
copper wire	110	210
nickel chromium wire	200	689

For most fibre reinforced polymers, adhesion between fibre and matrix is one of the main parameters affecting the composite properties [65]. The rule of mixture does not take this factor into consideration as it is only a function of the constituents' properties and the volume fraction of each. This may cause an overestimation of the mechanical properties.

Equations 4-2 and 4-3 can be used to predict samples' modulus (E_t) and ultimate strength (σ_t) respectively, evaluating composite properties with respect to the wire and the polymer properties (E_w, E_p, σ_w and σ_p) and volume fractions (v_w and v_p)

$$E_t = v_w E_w + v_p E_p \tag{4-2}$$

$$\sigma_t = v_w \sigma_w + v_p \sigma \mathrm{p} \tag{4-3}$$

Examples of predicted elastic moduli and ultimate strengths are shown in Table 4-3 and Table 4-4 where the volume fractions are based on the wire and samples' nominal dimensions.

Table 4-3 Predicted elastic moduli for continuous wire polymer composite

Rule of mixture for modulus							
Wire material	Wire Diameter (mm)	Sample dimensions (WxT) (mm x mm)	v_w %	v_p %	E_w (GPa)	E_p (GPa)	E_t (GPa)
Copper	0.075	25x1.8	0.7	99.3	110	3.6	4.34
nickel-chromium	0.075	25x1.8	0.7	99.3	200	3.6	4.97

Table 4-4 Predicted ultimate strength for continuous wire polymer composite

Rule of mixture for modulus							
Wire material	Wire Diameter (mm)	Sample dimensions (WxT) (mm x mm)	v_w %	v_p %	σ_w (MPa)	σ_p (MPa)	σ_t (MPa)
Copper	0.075	25x1.8	0.7	99.3	210	37	38.21
nickel-chromium	0.075	25x1.8	0.7	99.3	689	37	41.56

4.1.4 Result and Discussion

4.1.4.1 Optical Microscopy

Fabricated samples were examined using optical microscopy to quantify the wire volume fraction and voids within the printed structure. Optical microscope images of cross sections of the CWPC samples are shown in Fig. 4-3. Here images of the internal structure of the PLA demonstrate non-uniformity in the air voids within the sample, which is typical for fused filament fabrication, especially with a larger nozzle diameter (1 mm) used here. In Fig. 4-3 (b), the air voids are smaller as the incorporated metal reduces the voids when compared with the PLA-only samples. Although the air voids are smaller in Fig. 4-3 (c), wires seem not to be fully surrounded by polymer for a certain raster due to the higher volume fraction of the wire within the raster, which introduces a small void above the wire.

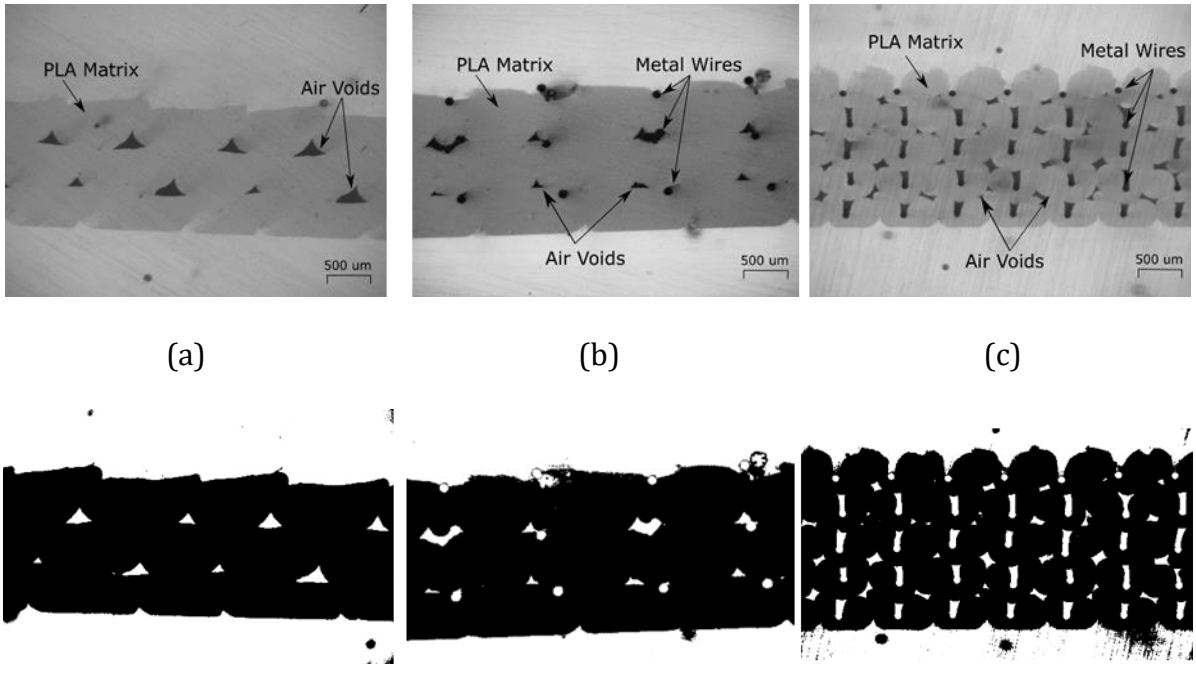

(a) (b) (c)

(d) (e) (f)

Figure 4-3 Cross section microscopy, a) PLA using 1 mm nozzle size, b) PLA with 75 µm wire using 1 mm nozzle, c) PLA with 75 µm wire using 0.6 mm nozzle and d), e) & f) the processed images respectively

The image processing analysis for the cross-section images showed some deviation with the nominal volume fraction calculations. The measured volume fractions shown in Table 4-5 address the values for the volume fraction measured by ImageJ tools. As mentioned, there are fewer air voids in the samples with wires extruded through the 1 mm nozzle (1.63%). For the 0.6 mm nozzle, air volume fraction is much higher (5.58%).

Table 4-5 Image processing results for different volume fractions

PLA (1mm nozzle)	
PLA	96.68%
Air	3.32%
PLA+75 µm wire (1mm nozzle)	
PLA	97.39%
Air	1.63%
Wire	0.98%
PLA+75 µm wire (0.6mm nozzle)	
PLA	92.94%
Air	5.58%
Wire	1.48%

4.1.4.2 Mechanical properties' statistics

Average values for the measured elastic modulus (E_t) and ultimate stress (σ_t) for the six samples are reported in Table 4-6. A comparison of the PLA, PLA + nickel-chromium and PLA+ copper wires is shown in Fig. 4-4. The figure shows the experimentally measured values for elastic moduli as well as the theoretical values calculated using equation (2). Regarding the modulus, the nickel-chromium wire reinforced samples showed superior enhancement with an average of 3.833 GPa compared with the 2.945 GPa for non-reinforced PLA. On the other hand, copper

reinforced samples showed much less improvement with 3.216 GPa. Therefore, an improvement in the modulus of the PLA of 30% is obtained with the nickel chromium and 9% for the copper wire with a 0.7% wire volume fraction.

A comparison of the measured and predicted ultimate strengths for the fabricated samples is shown in Fig. 4-5. The deviation between the results and the model is believed to be due to wire slipping inside the matrix. The values for the ultimate strength (Fig. 4-5) showed greater deviation with the model, especially for the copper reinforced samples as the copper wire surface seems to be smoother compared with the nickel-chromium one; this might be attributed to the potentially smoother surface offered by the polyamide coating.

Table 4-6 Average modulus and ultimate strength values

Material	Wire volume. fraction	Average E_t (GPa)	STD %	Average σ_t (MPa)	STD %
PLA	-	2.945	1.188	49.4	3.52
Ni-ch/PLA	0.007	3.833	4.93	51.15	2.77
copper/PLA	0.007	3.216	5.69	47.4	4.32

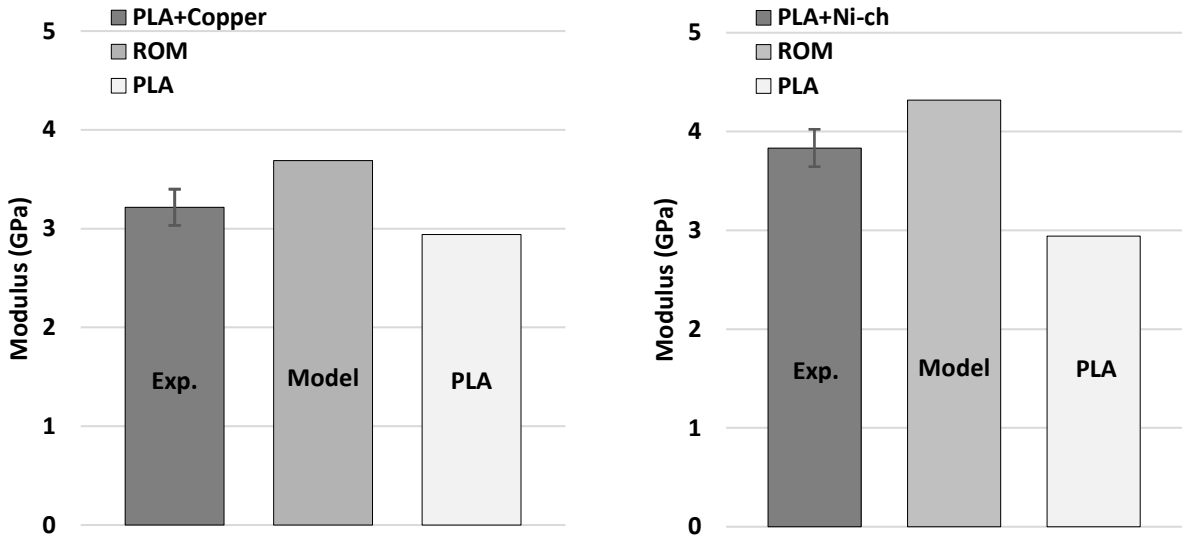

(a) (b)

Figure 4-4 a) Modulus of PLA+copper compared with PLA, b) Modulus of PLA+Ni-ch compared with PLA using 1mm nozzle

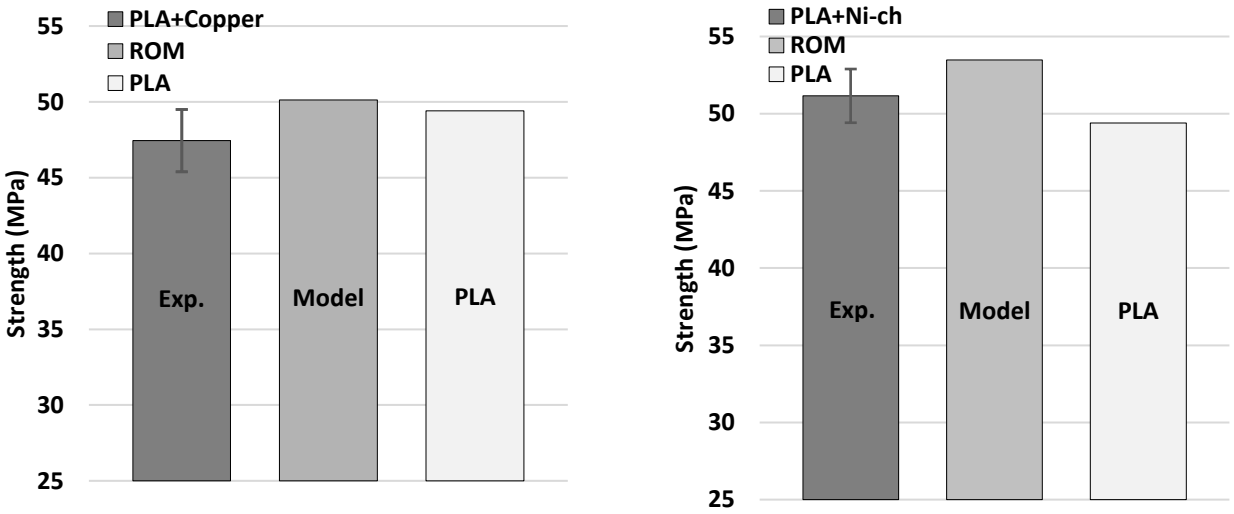

(a) (b)

Figure 4-5 a) Ultimate strength of PLA+copper compared with PLA, b) Ultimate strength of PLA+Ni-ch compared with PLA using 1mm nozzle

4.1.4.3 Smaller Nozzle Diameter and Metal Powder Reinforced Filament

Further investigation was performed to explore the effect of the reinforcement wires' volume fraction. Three samples of 75 μm nickel-chromium wire reinforced PLA were printed with a 0.6 mm nozzle and 0.4 mm layer height. The wire nominal volume fraction was 1.7%. The test samples show similar behavior to the ones reported in section 4.2 with the 1mm nozzle, with an improved higher modulus of 3.93 GPa, a 33% improvement compared with pure PLA samples and a slight decrease in the ultimate strength of 50.1 MPa (Fig. 4-6). One reason for the larger deviation between these samples and the analytical model compared with the ones printed with the 1 mm nozzle is that the used value for the modulus and ultimate strength of PLA is for the one printed with the 1mm nozzle. In addition, it can be noticed from the microscopic images (Fig. 4-3 (c)) that the volume fraction of air is larger in these samples. Thus, less polymer and more air are surrounding the embedded wire, which means less contact between the wire and the matrix and an increase in the probability of wire slipping under different types of loads.

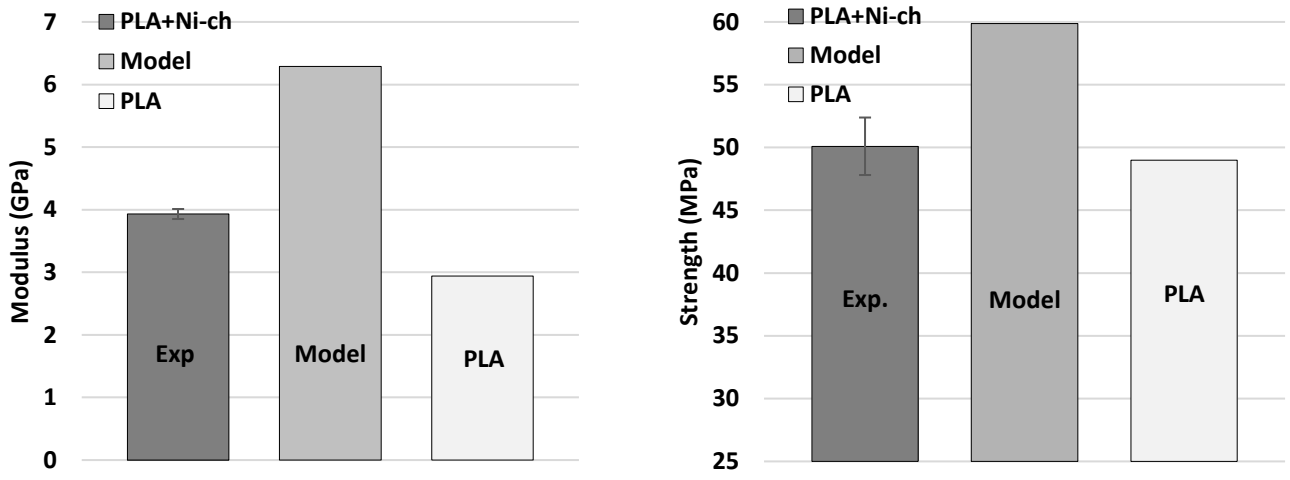

(a) (b)

Figure 4-6 a) Modulus of PLA+Ni-ch compared with PLA, b) Ultimate strength of PLA+Ni-ch compared with PLA using 0.6mm nozzle

To study the effect of different matrices on the mechanical behavior of the CWPCs, three hybrid reinforced samples of 75 μm nickel-chromium wire were printed with metal powder reinforced filament using a 0.6 mm nozzle, and three were printed without the wire (Fig. 4-7 (a)). In this case, the matrix was already reinforced with metal filler. The 1.75 mm metal x PLA blend filament (SainSMART, Kansas, USA) was used as a matrix. The reinforced filament contains a spherical-shaped copper particle which is believed to exert more friction and adhere better to the metal wire. The metal powder reinforced samples were tested first, and the values of the tensile modulus and ultimate strength were recorded; on average, a tensile modulus of 2.98 GPa and ultimate strength of 31.9 MPa were recorded for the three samples which have a slightly higher modulus (2.945 GPa) and

a lower ultimate strength (49.4 MPa) compared with non-reinforced PLA. This comparison shows that the copper filler exerts almost no effect on the matrix modulus. These values were used as an input for the analytical model to predict the behavior of wire reinforced samples. Samples with wire reinforcement were then tested and the stress-strain values were obtained (Fig. 4-7 (b)). The samples showed closer values to the analytical model (Fig. 4-8 (a)) as it is believed that the composite filament exerts more adhesion to the wire. Regarding strength (Fig. 4-8 (b)), an average ultimate strength of 40.55 MPa which was lower than the model was obtained. It is noticeable that the ultimate strength shows better fit with the model when substituting the volume fraction obtained by the image processing. The modulus and ultimate strength showed 50% and 27% improvement, respectively, compared with the metal powder reinforced samples.

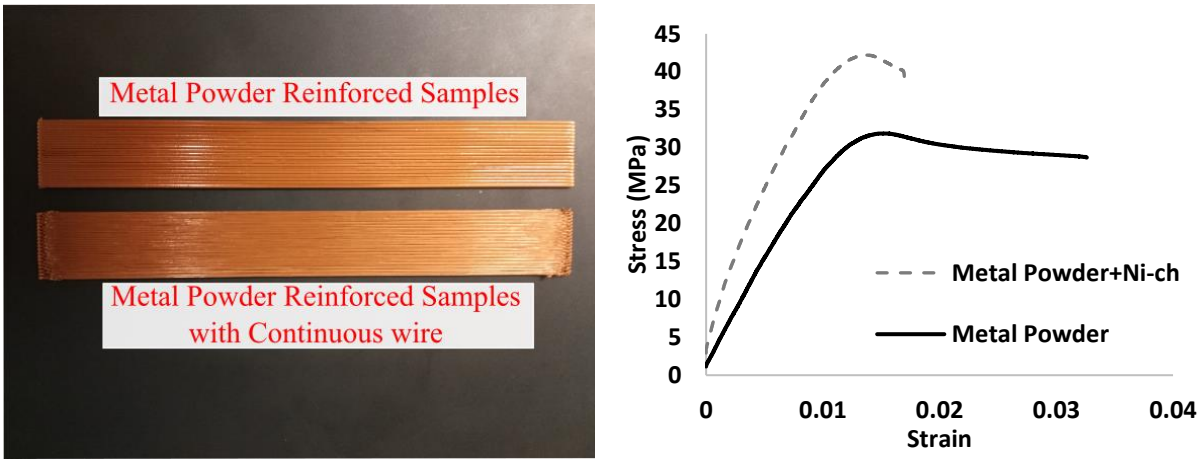

(a) (b)

Figure 4-7 a) Metal powder reinforced samples, b) Experimental stress-strain curve for the nickel chromium wire – metal powder reinforced sample compared to metal powder reinforced sample

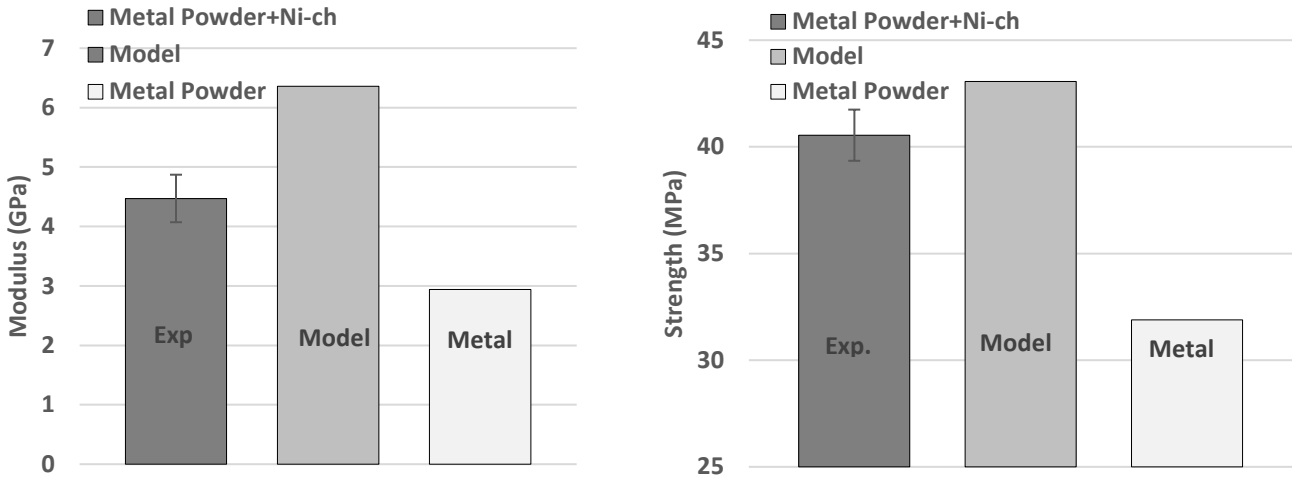

(a) (b)

Figure 4-8 a) Modulus of nickel chromium – metal powder reinforced sample compared to metal powder reinforced sample, b) Ultimate strength of nickel chromium – metal powder reinforced sample compared to metal powder reinforced sample using 0.6 mm nozzle

4.2. Investigation of Flexural Properties

To further investigate the effect of printing parameters on the mechanical properties of CWPCs, we performed a bending test. By making a design of experiment (DOE) study, we investigated the effect of wire volume fraction, wire surface roughness and matrix material on the flexural properties of CWPCs. The composite properties were obtained experimentally and predicted analytically. In addition, a common solid of mechanics model was customized to predict the composite flexural properties as a function of the print geometry and printing parameters.

4.2.1. Flexural Samples Fabrication

Three-point bending samples were printed using the method previously described in Chapter 3 to investigate the effect of different parameters on the flexural properties of CWPC beams. Wire-reinforced and non-reinforced samples were printed with three different filaments. The different matrix materials are summarized in Table 4-7 and included: PLA, PLA reinforced with chopped carbon fibre (denoted as CF), and PLA reinforced with aluminium particles (denoted as Al). A 75 μm nickel-chromium wire (McMaster-Carr, Ohio, USA) was used as the continuous reinforcement material for all samples. To create different wire volume fractions within the samples, two nozzle diameters of 1 mm and 0.6 mm were used. A photograph of the reinforced and non-reinforced samples printed using different matrix materials is shown in Figure 4-9.

Table 4-7 Matrix materials and supplier

Filament	Supplier
1.75 mm PLA	Spool 3d, Canada
1.75 mm PLA + CF (CF)	Proto-pasta, ProtoPlant Inc, Vancouver, Canada
1.75 mm PLA + Al (Al)	SainSMART, Kansas, USA

The CWPC samples for the three-point bending tests were 3D printed according to the dimensional standards set out in ASTM D790-17 [66]. For high-strength reinforced composites and high orthotropic materials the standard recommends a span to height ration of 60:1 to eliminate the effect of shear stress. For the 1mm nozzle diameter, samples of three layers with 0.6 mm layer height were printed while for the 0.6 mm nozzle, samples of four layer with 0.4 mm layer height were printed. Samples length was 200 mm to comply with the 60:1 ratio for the nozzle diameters. Sample dimensions are summarized in Table

4-8.

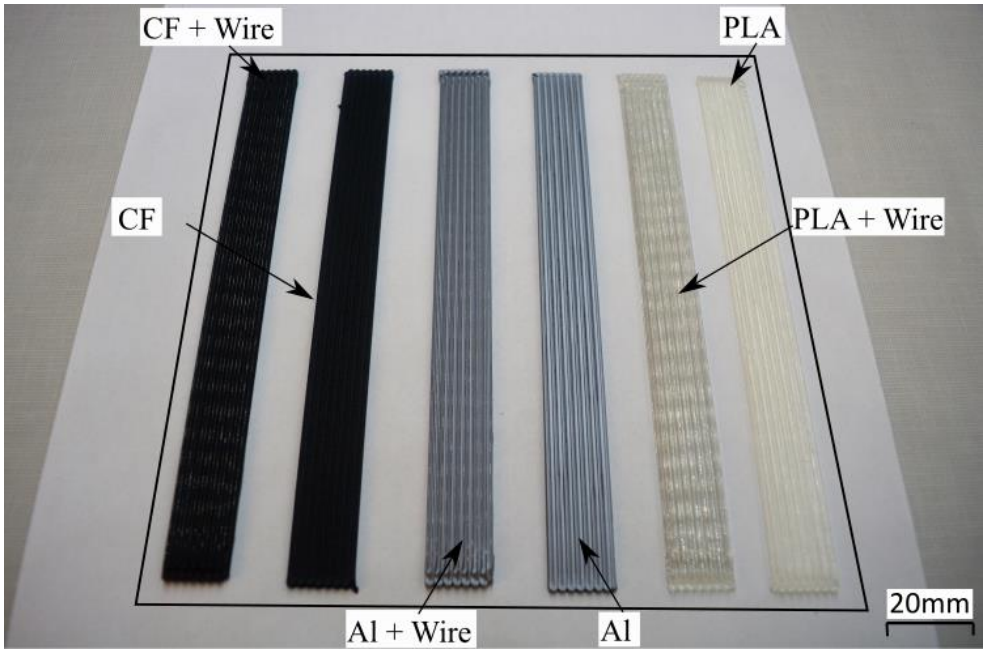

Figure 4-9 Reinforced and non-reinforced samples of different matrix materials

Table 4-8 Flexural samples dimensions

Length (L)	200	(mm)
Width (W) (mm)	15	(mm)
Height (H) (mm)	1.8 – 2.0	(mm)
Wire diameter (mm)	0.075	(mm)

Printing parameters were selected as shown in Table 4-9. Although PLA and Al matrix samples can be printed with a lower printing temperature, the temperature was set to 200 ˚C for all the filaments because the CF matrix requires a higher printing temperature. The printing code of the samples was generated using a MATLAB script to specifically create unidirectional samples without creating any overlap between rasters and to eliminate the need for wire cutting. The calculated extrusion volume per raster was multiplied by a 1.05

extruder multiplier to create partial overlap between adjacent rasters to improve adhesion.

Table 4-9 Main printing parameters

Extruder Temp.	200	(°c)
Bed Temp.	55	(°c)
Extruder Multiplier	1.05	
Printing Speed	7	(mm/s)
Raster width (mm)	1.05 – 0.65	(mm/s)
Layer height	0.6 – 0.4	(mm)

4.2.2. Wire Treatment and Roughness Measurements

For CFPCs, the adhesion and interaction between the fibres and the polymeric material is crucial and can affect the composite's final properties [67], [68]. Continuous reinforcement can improve the material properties significantly if perfect bonding exists. However, weak bonding can degrade the material properties because the reinforcements act as voids and stress concentration locations within the composite material [69]. We can expect the same to be true for CWPCs and, therefore, to investigate the effect of wire surface roughness of the flexural properties, a wire treatment process was developed to etch and thereby roughen the wire for improved bonding to the polymer. The wire treatment mechanism is shown in Fig. 4-10. Here, a stepper motor controlled by a A4988 micro-stepping driver and an Arduino Mega 2560 R3 board pulls the wire through a 42% solution of ferric chloride to etch the wire surface before being collected on a secondary spool. The wire was pulled through the treatment bath at 2 mm/s resulting in soak time of approximately 50 seconds. This approach was chosen as the solution is not easily saturated since the etched material settles down the treatment path and because minimal mechanical or thermal stresses are applied on the wires through the process.

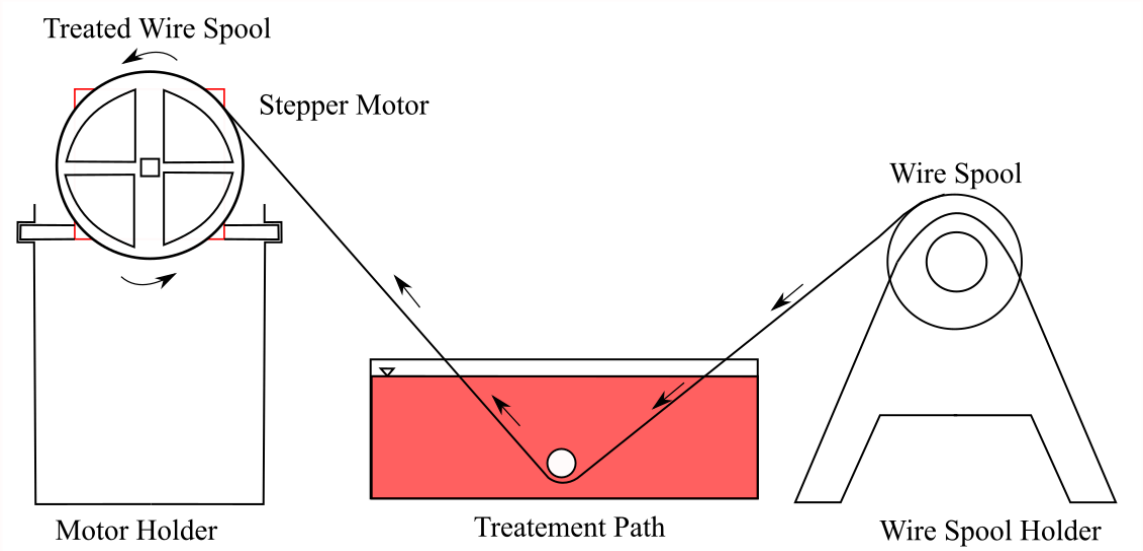

Figure 4-10 Wire treatment mechanism for altering the surface roughness of reinforcing wires used in the fabrication of CWPC structures

Wire surface roughness was measured using a Bruker ContourGT optical profilometer (Bruker, Massachusetts, United States). The cylindrical feature was used to flatten the wire curvature and an arithmetic mean roughness (R_a) value was obtained. Twelve measurements were recorded for different positions upon the treated and non-treated wires and the uncertainty in the R_a value found after computing the standard deviation of these measurements was based on 95% confidence level (i.e., 1.96 standard deviations).

4.2.3. Design of Experiments (DoE)

The CFPCs or CWPCs created using fused filament fabrication (FFF) technique can be greatly affected by the printing parameters as well the matrix and reinforcement properties as observed by in the tensile testing. Ahn *et al.*[70] and Melenka *et al.* [71] have studied the effect of different printing parameters on the tensile properties of non-

reinforced polymers as a part of DoE studies. The objective of the present study is to investigate the effect of different CWPC printing parameters on flexural properties. Although printing temperature, printing speed and raster width can affect the final properties of the CWPC, it is believed in the current study that the matrix type, wire volume fraction and wire treatment will have more significant impact on the final properties of the CWPC as per observations made previously in Section 4.1.

The three parameters of the process were input as variables in a DoE study, while the ultimate flexural strength and flexural modulus were selected as the response. Table 4-10 shows the input variables and the studied level for each. Three levels of matrix materials were implemented while two levels were chosen for the wire volume fractions and the wire treatment conditions. The DoE study was carried out in two steps: First, the wire-reinforced PLA matrix was compared against the wire-reinforced CF filament. In the second stage, the wire-reinforced PLA matrix was compared against the wire-reinforced Al filament. A 2^3 full factorial design was created using the open source software R (R Foundation for Statistical Computing, Vienna, Austria) for each stage.

Table 4-10 DOE variables and levels

Variable	Levels	
	Low (-)	High (+)
Matrix	PLA	CF or Al
Wire volume fraction	0.70%	1.70%
Wire treatment	Not-treated	Treated

The experimental testing procedure is shown in Table 4-11 where all the possible combinations of the studied variables are tabulated. Three replicates of each variable combination were performed to establish repeatability and uncertainty.

Table 4-11 DoE experimental testing sequence

Run	Filament	Nozzle diameter (mm)	Wire volume fraction (%)	Wire Treatment	No. of replicates
1	Al	0.6	1.7	Treated	3
2	Al	1	0.7	Not-treated	3
3	PLA	1	0.7	Treated	3
4	PLA	0.6	1.7	Not-treated	3
5	Al	1	0.7	Treated	3
6	Al	0.6	1.7	Not-treated	3
7	PLA	1	0.7	Treated	3
8	PLA	0.6	1.7	Not-treated	3
9	CF	0.6	1.7	Treated	3
10	CF	1	0.7	Not-treated	3
11	PLA	1	0.7	Treated	3
12	PLA	0.6	1.7	Not-treated	3
13	CF	1	0.7	Treated	3
14	CF	0.6	1.7	Not-treated	3
15	PLA	1	0.7	Treated	3
16	PLA	0.6	1.7	Not-treated	3

4.2.4. Samples Preparation and Testing

4.2.4.1 Sample Measurements

In stress analysis experiments, dimensions and area are crucial for proper evaluation of stress and deformation. The bending samples described previously were measured and the samples' length, width, and height were recorded. Using a 6.35 mm flat anvil micrometer (Mitutoyo), three measurements across the samples were made and average values were calculated to implement in stress calculations. The uncertainty in the cross-section areas was found to be less than 0.26%, which shows that the samples' dimensions were consistent.

4.2.4.2 Test Frame and Procedure

A universal test frame (MTS Criterion Model 43, Eden Prairie, Minnesota, USA) was used to conduct the bending tests. A custom three-point bending apparatus made of steel was attached to the machine grips (Fig. 4-11 a). The force was measured using a 10 kN load cell, while the deformation was measured using laser extensometer (LX500 laser extensometer, MTS, Eden Prairie, Minnesota, USA). Two reflective tape strips were attached to the loading nose and the fixed support (Fig. 4-11 b). The distance between the two fixed points of the test fixture was set to 160 mm to maintain a span-to-height ratio of 60:1 for all samples.

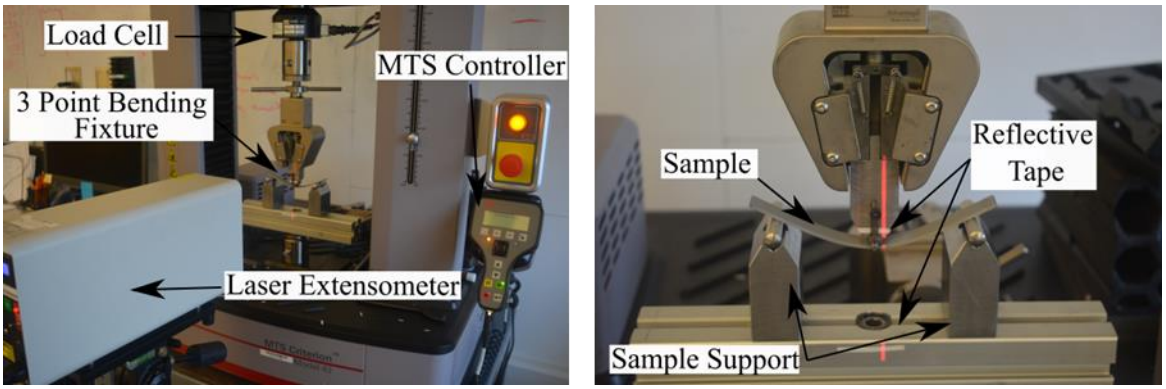

(a) (b)

Figure 4-11 Mechanical testing apparatus for evaluating the mechanical properties of CWPC structures (a) Bending test apparatus (b) Bending samples under deformation

The recommendations of ASTM D790-17 standard for reinforced and unreinforced plastic testing procedures were followed for testing. The rate of the crosshead was 0.35 mm/s as per the equations described in the standard. Simultaneous load deflection measurements were recorded using MTS (Testworks, MTS, Eden Prairie, Minnesota, USA) software with the extensometer readings added. The test was terminated when a sample failed or

reached a strain of 0.05 mm/mm as per the ASTM D790-17 guidelines [66].

4.2.4.3 Microscopy Sample Preparation

The mechanical properties of FFF fabricated CWPC components can be greatly be affected by their internal structure, geometrical aspects and reinforcement-polymer interaction. Due to the nature of FFF, air voids usually exist within the printed parts where the size and the shape of these voids affects the final mechanical properties [72]. Furthermore, raster overlap can also be a significant parameter that affects the product properties (Fig. 4-12). Although using open-source and low-cost 3D printers has obvious benefits for the creation of CWPC components, sample quality and precision cannot be guaranteed and needs to be examined subsequent to printing. Moreover, for precise properties and analytical modelling of these samples, an accurate reinforcement volume fraction is needed. To this end, microscopic images were captured of the flexural samples' cross-sections in order to better understand their internal structure and quantify volume fractions. One sample each of the reinforced and non-reinforced samples were sectioned and polished in a similar fashion to the tensile samples in Section 4.1.2.3. The same stereo-microscope (LEICA MZ10 F, LEICA, Germany) was used to capture the cross-section images and ImageJ (National Institutes of Health, Bethesda, Maryland, USA) used for image processing.

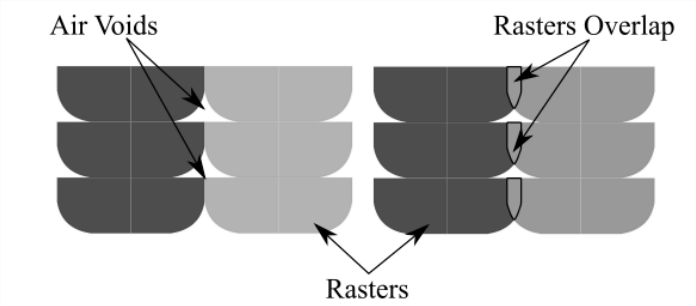

Figure 4-12 Unidirectional rasters schematic showing rasters overlap and air voids

4.2.4.4 Stress and modulus calculations

The reinforced nature of CWPCs makes them well suited for bending applications; however, the flexural strength of CWPC structures has not been investigated. The maximum stress is expected at the midpoint of the beam because this point is subjected to the biggest moment value. According to the ASTM D790-17 standard, the maximum flexural stress for a rectangular homogeneous beam with a span-to-length ratio greater than 16:1 can be presented in the form of (4-4) as a function of the load and dimensions [66].

$$\sigma_f = \frac{3PL}{2bd^2}[1 + 6(\mathrm{D/L})^2 - 4(d/L)(D/L)] \qquad (4\text{-}4)$$

For flexural strain (ε), the change in the length of an element at the outer surface can be presented in the form of (4-5).

$$\epsilon = \frac{6Dd}{L^2} \qquad (4\text{-}5)$$

The chord flexural modulus described in (4-6) was used to calculate the samples' moduli

where 0.001 and 0.02 mm/mm strain values were selected to find the chord modulus between them. The pre-specified strain values were chosen because the stress-strain curves gave the best linearity in this region and it was compatible with all types of matrix materials used in the present study.

$$E = \frac{(\sigma_2 - \sigma_1)}{\epsilon_2 - \epsilon_1} \tag{4-6}$$

4.2.5. Analytical Modelling

Understanding the stress distribution within a beam section is vital for design purposes. The ultimate stress that a beam under bending moment can withstand is mainly limited by the beam's material properties. Beam shape and construction can play a significant role in reducing stresses that the beam is subjected to. For homogeneous materials, the bending stress across the beam cross-section can be described as a function of the linear position *y* of a point that the stress has been calculated for by (4-7).

$$\sigma_f = \frac{My}{I} \tag{4-7}$$

Even though (4-7) can describe the stress distribution, material homogeneity can still be an issue, especially with composites. Considering a composite material as a homogeneous material depends on the scale of the study. On a macro scale, certain composite materials can be considered to be a homogeneous material while simultaneously considered to be heterogeneous on a micro-scale. Heterogeneous materials create non-uniformity in the stress distribution within the material, which leads to an over-estimation of the stress across the beam.

Another approach involves the transformed section method and can be used to create an equivalent homogeneous cross-section where (4-7) can be applied without the aforementioned homogeneity concerns. This method is commonly used for composite beams made of different materials where the reinforcement material area is replaced by an equivalent area of the matrix material [73]. This approach gives more accurate stress distribution upon the cross-section and the stress values within the wires and the matrix because the stress distribution is no longer linear across the cross-section after adding the wires. The existence of air voids shall be disregarded in order to apply this model. The wire reinforcement equivalent area can be calculated using (4-8).

$$A_{eq} = \frac{E_w}{E_m} A_w \tag{4-8}$$

The condition for the transformed area method is that the equivalent cross-section should occupy the same height as the original, because the strain distribution must be preserved. Figure 4-13 (a) shows the original cross-section while Fig. 4-13 (b) shows the equivalent cross-section where both have the same height, H; D_w is the wire diameter, H_l is the layer height, and W is the sample width.

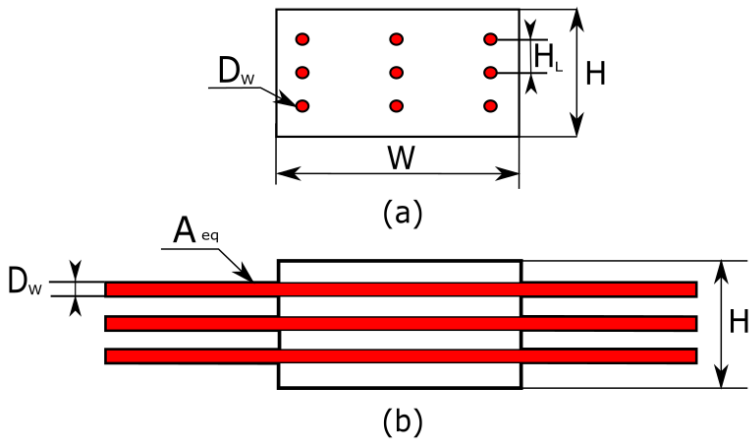

Figure 4-13 (a) Original and (b) equivalent sample cross-sections

Using the equivalent area method, (4-7) can now be applied on the equivalent cross-section without concern for homogeneity. The main difference is the new value of the area moment of inertia which can reduce the value of the stress significantly. An analytical model has been developed specifically in equations (4-9) to (4-12) for CWPC that describes the area moment of inertia of the equivalent cross-section as a function of the constituent material's geometrical parameters and properties.

The area moment of inertia for the unidirectional samples described in Fig. 4-13 for both odd and even layers count given by:

$$I = I_l + 2\sum_{n=1}^{\frac{N-1}{2}} I_l + A_l(nH_l)^2 \qquad (4\text{-}9)$$

For N= 3, 5, 7, …

$$I = 2\sum_{n=0}^{\frac{N-2}{2}} I_l + A_l\left[(n+\tfrac{1}{2})H_l\right]^2 \qquad (4\text{-}10)$$

For N= 2, 4, 6, …

The equations describe the area moment of inertia of the cross-section *I* as a function of a single layer area moment of inertia shown given by

$$I_l = \frac{wD^3}{12} + \frac{\pi N^*}{48}\left(\frac{E_w}{E_M} - 1\right)D^4 + \frac{w(\frac{H-D}{2})^3}{6} + w(H-D)(\frac{H+D}{4})^2 \qquad (4\text{-}11)$$

$$A_l = w(H_l - D) + wD + \frac{\pi N^*}{4}(\frac{E_w}{E_m} - 1)D^2 \qquad (4\text{-}12)$$

The analytical model presented can be a useful design tool for a CWPC subjected to bending stresses as it can be fed directly to (4-7) where the maximum bending moment can be inferred by replacing σ with the ultimate flexural strength of the matrix material if perfect bonding between the matrix and the wire exist. The model disregards air voids existence within the matrix. For which, experimental results are to be used to verify the results obtained by the presented model.

4.2.6. Results and Discussion

4.2.6.1 Microscopy

The wire reinforced and non-reinforced PLA sample cross-sections were 3D printed as described above. Figure 4-14 shows the captured images with the matrix material, air voids, and the wire reinforcement indicated in each. For the 1 mm nozzle samples shown in Fig. 4-14 (a), despite using a 1.1 extruder multiplier, poor raster adhesion and large air voids occurred. However, when the 0.6 mm nozzle was used, samples showed better adhesion between rasters, yet with relatively larger air voids (Fig. 4-14 (b)). As the same

printing code was used for both wire-reinforced and non-reinforced samples, it can be noticed in Fig. 4-14 (c) and (d) that the wire-reinforced samples show better raster adhesion and less air voids compared with the non-reinforced samples. The presence of the wire within the matrix pushes the matrix material to fill in the air voids which reduces the overall void volume fraction.

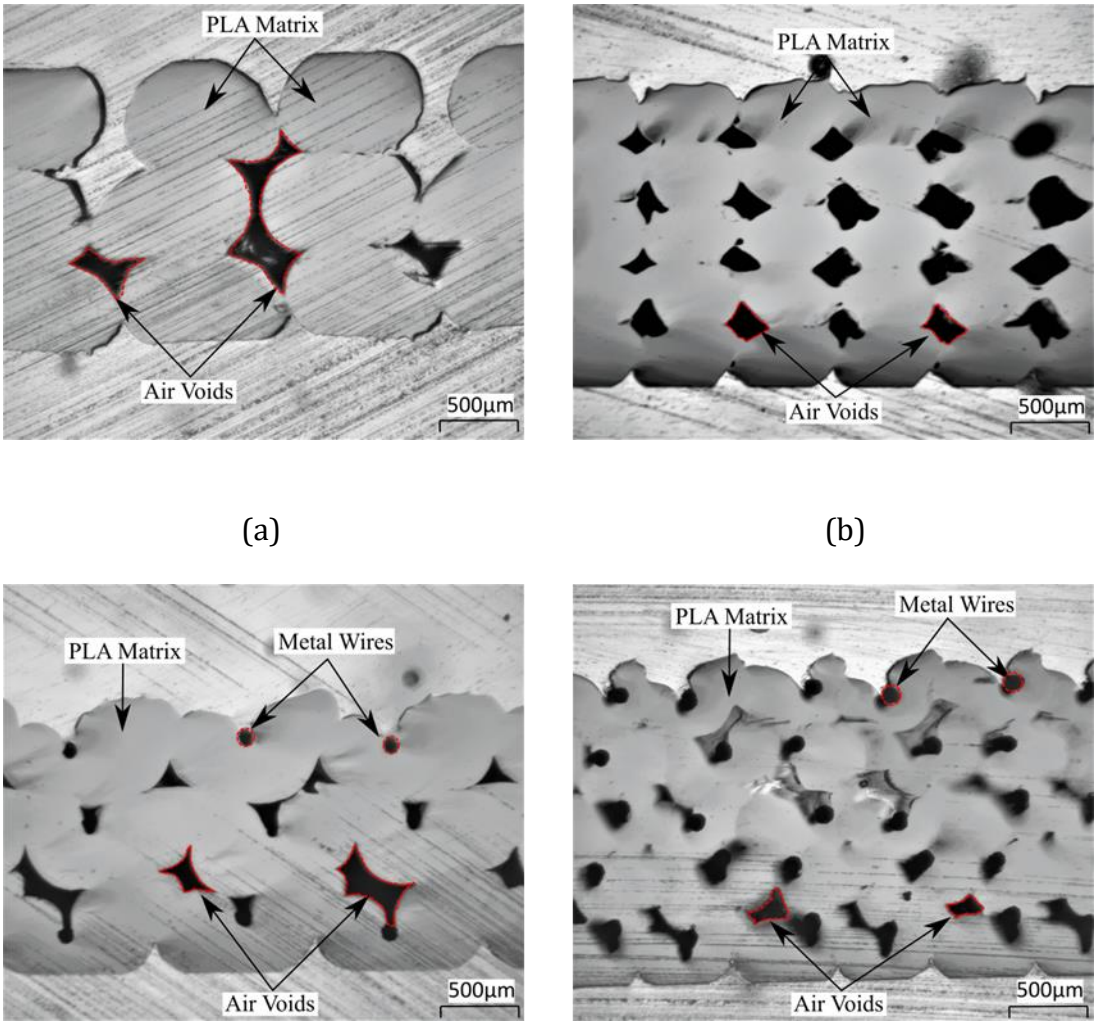

Figure 4-14 PLA samples microscopy (a) 1mm nozzle non- reinforced, (b) 0.6 mm nozzle non-reinforced, (c) 1mm nozzle wire reinforced, (d) 0.6 mm wire reinforced sample

The images were processed using ImageJ as described above to quantify the wire volume fraction. Table 4-12 shows the measured wire volume fraction compared with those calculated from the printing input parameters. Measured volume fractions are higher than the calculated values. This could be due to several factors including deviation between the input parameter and the output of the printer which may be determined by the precision of the printer. Moreover, input parameter calculations consider the raster as a rectangle with a width and height equal to the raster width and height, while the actual raster shape is not rectangular as shown in Fig. 4-14

Table 4-12 Wire volume fraction

Sample	Void fraction (%)	Measured wires fraction (%)	Calculated wires fraction (%)
a	15.41046	--	--
b	14.39577	--	--
c	7.115797	1.173765	0.7
d	13.46879	1.750934	1.7

4.2.6.2 Wire Roughness Measurements

The surface roughness of the treated wires was measured using an optical profilometer and compared with the untreated wires. Six measurements were made at different positions along the wires. The measurements in Table 4-13 show higher R_a values for the treated wires. The measurements of the untreated wires comply with the value provided by the manufacturer which was 0.2 μm. The higher value of the standard deviation for the treated wires is believed to be caused by variability in the etching process where some sections may be etched more than others.

Table 4-13 Surface roughness measurements

Not-treated wires		Treated wires	
Average R (μm)	STD (μm)	Average R (μm)	STD (μm)
0.267	0.0477	0.821	0.131

4.2.6.3 Failure Modes

Understanding of failure behavior for CFPCs and CWPCs is crucial for mechanical property characterization and for design purposes. Due to the continuous nature of the reinforcement which limits the dispersion of the reinforcement within the filament, adhesion between the matrix and reinforcement cannot be perfect. Matrix dominated failure was expected to occur in the composite samples due to the large difference between the matrix and the continuous reinforcement properties. This means that the matrix tends to detach from the reinforcement and fail when the bonding is not sufficient. Sample failure images shown in Fig. 4-15 (a) were captured to investigate matrix failure. For the CF filament, it was noticed that for the non-reinforced sample, a complete failure occurs within the testing limits because the material seems to be brittle. This explains the matrix dominated failure in the wire-reinforced sample as shown in Fig. 4-15 (b). On the other hand, the Al matrix did not fail completely during the test because the strain limitation was reached, which also happened with the corresponding wire-reinforced samples with a preserved deformation. For the PLA sample, the matrix did not fail completely. However, complete failure was noticed for the corresponding wire-reinforced samples as in in Fig. 4-15 (c). In the light of this information, better understanding of the values of the flexural properties can be obtained.

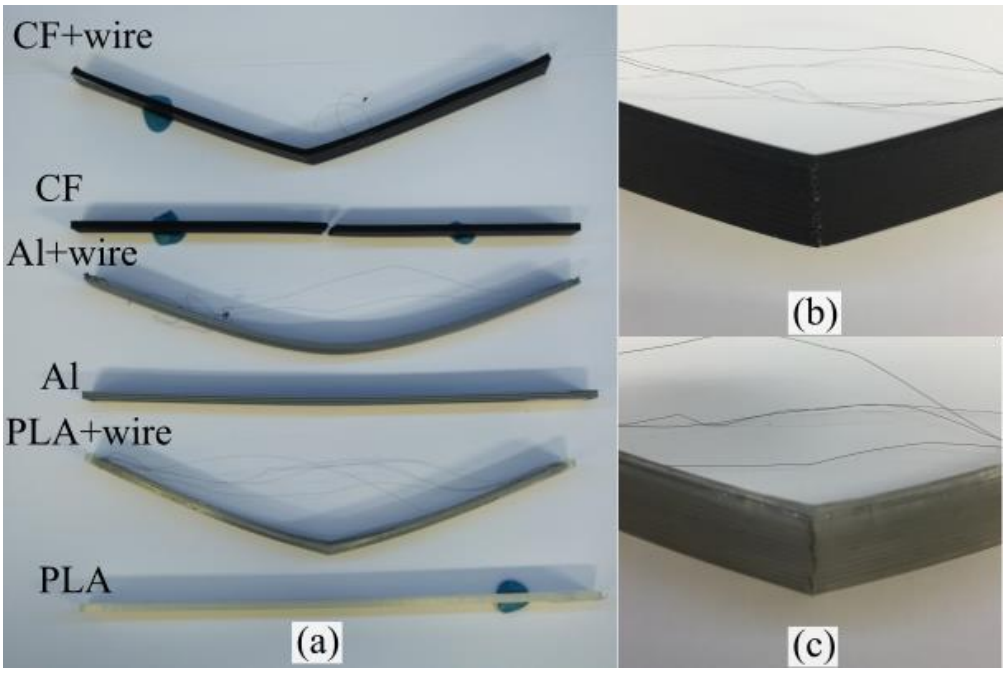

Figure 4-15 (a) Failure for each sample, (b) close up of reinforced CF sample failure, (c) close up of reinforced PLA sample failure

4.2.6.4 DoE Results

The testing sequence described in Table 5 was followed and the results obtained were input into the R software to create the main effect plots for the three variables of the flexural modulus and ultimate strength as shown in Fig. 4-16. The values of ultimate flexural stress and flexural modulus were calculated using equation described in Section 4.2.4.4 and the plots show the effect of each parameter separately.

The wire treatment showed almost no effect on both modulus and ultimate strength of the reinforced samples while the two other variables showed significant effect. For the CF compared to the PLA reinforced samples in Fig. 4-16 (a), It is noticed that the chopped fibre within the matrix improve the CWPCs ultimate strength and even more improvement on

the modulus as in Fig. 4-16 (b). On the other hand, an increase in the wire volume fraction showed an increase in both ultimate flexural strength and flexural modulus.

The aluminum particles within the matrix in the Al samples showed less effect on the ultimate strength and modulus compared to the chopped carbon fibres. As shown in Fig. 4-16 (c) & (d), the wire volume fractions showed more significant effect on both strength and modulus.

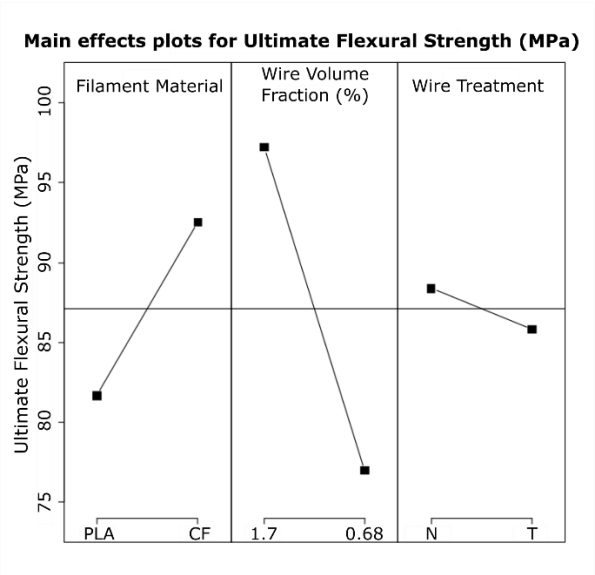

(a)

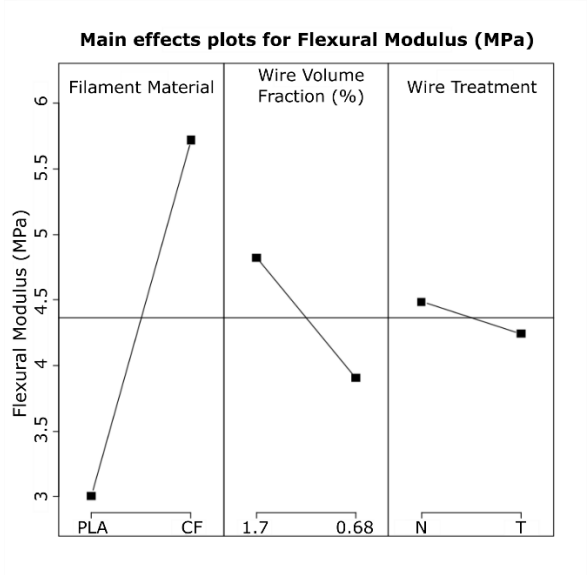

(b)

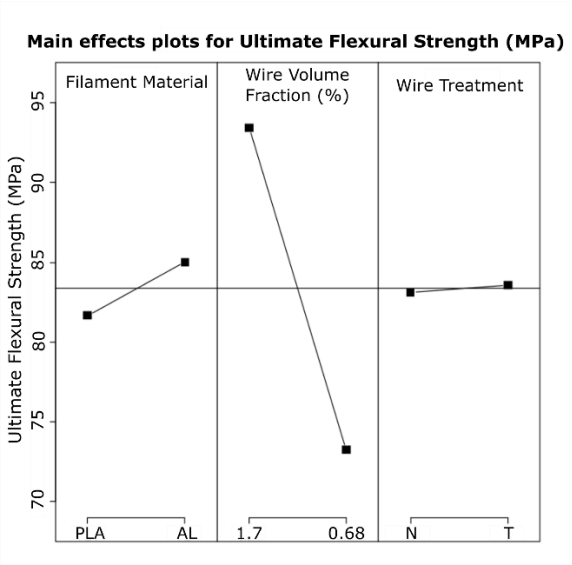

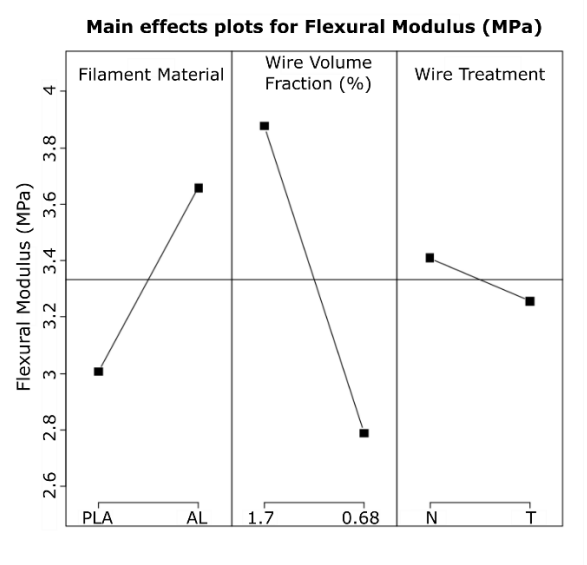

(c) (d)

Figure 4-16 (a)Main effects plots for ultimate flexural strength of reinforced PLA and CF(b)Main effects plots for ultimate flexural strength of reinforced PLA and AL (c) Main effects plots for flexural modulus of reinforced PLA and CF (d) Main effects plots for flexural modulus of reinforced PLA and Al

4.2.6.5 Flexural Results

Proper stress calculation is necessary for proper design of construction beams. As discussed previously, stress calculation for CFPC or CWPC samples will be subject to the material homogeneity. If the samples are to be considered as a homogeneous material, the approach of calculating ultimate stress described in Section 4.2.4.4 – (4-7) is to be valid. The values of the ultimate flexural strength and modulus shown in Fig. 4-17 can be used for CWPC beams design. The figure shows the values of the ultimate flexural ultimate strength and modulus for the reinforced samples printed with two different wire volume fractions.

The 1.7% wire volume fraction exerted higher modulus and strength compared with the 0.68% as expected for a higher reinforcement volume fraction.

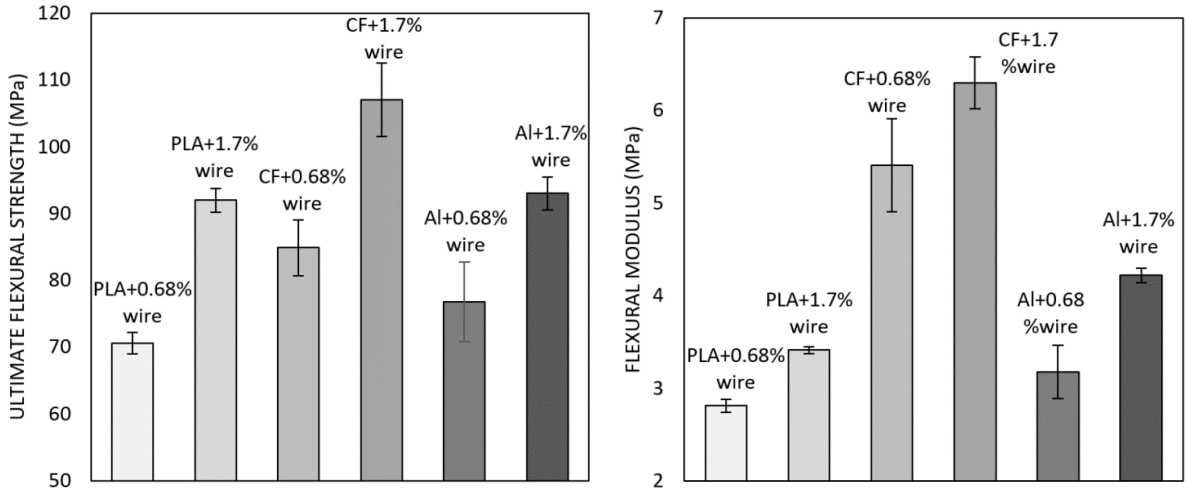

(a) (b)

Figure 4-17 (a) Flexural ultimate strength and (b) flexural modulus for reinforced and non-reinforced matrix materials printed with 0.68% and 1.7% wire volume fraction

The second approach is to find an equivalent cross-section of the matrix material as described in Section 4.2.5. In this case, the ultimate flexural strength and modulus values of the matrix material can be used as reference values for beam design purposes. This approach can give a better prediction for the stress distribution on the beam cross-section. However, this assumes perfect bonding between the matrix material and the reinforcement, which may not be the case. By changing the value of the area moment of inertia with another corresponding to the equivalent cross-section area, the value of the stress drops significantly, as shown in Fig. 4-18. This figure shows the stress-strain relation in the elastic zone for a PLA+ wire sample printed with the 0.6 mm nozzle. The stress is

calculated using the sample original cross-section area and presents higher values compared with the one calculated with the equivalent cross-section area described above. At the same strain value, the continuous wire helps to reduce the stress value because it is equivalent to a larger area of the matrix material.

The ultimate flexural strength using the equivalent area approach was calculated and compared with the experimental values obtained from the non-reinforced samples. The ultimate flexural force for the reinforced samples was used in conjunction with Equations (4-9) to (4-12) to calculate the ultimate flexural strength. The values were expected to be the same for the non-reinforced samples if perfect bonding existed. Figure 4-19 shows the expected values and the experimentally obtained ones where deviation between the values was obtained. It is believed that the deviation was caused by the deficiency in adhesion between the wires and matrix material. The fact that the failure is dominated by the matrix material as discussed previously also explains the deviation. Furthermore, qualitatively, it was apparent that the CF matrix material was much rougher than the other two materials, which may explain the least deviation between the measured and modelled values for this case because the rough surface may adhere better to the wires.

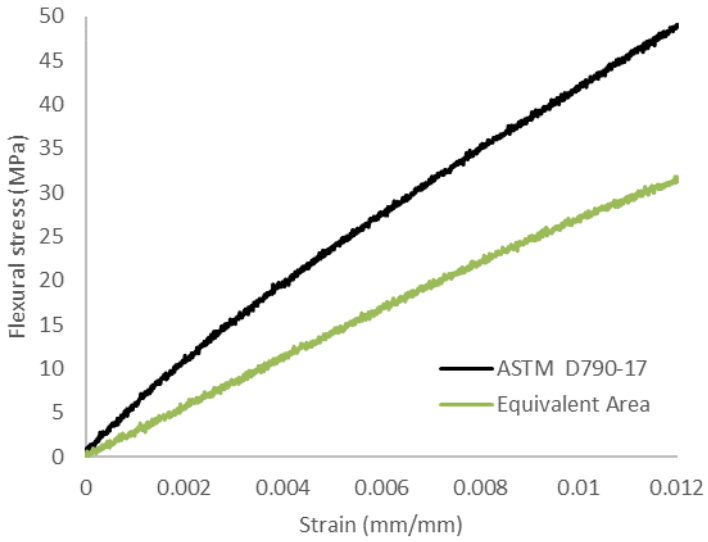

Figure 4-18 Stress-strain relation for original and equivalent cross -sections through the elastic region

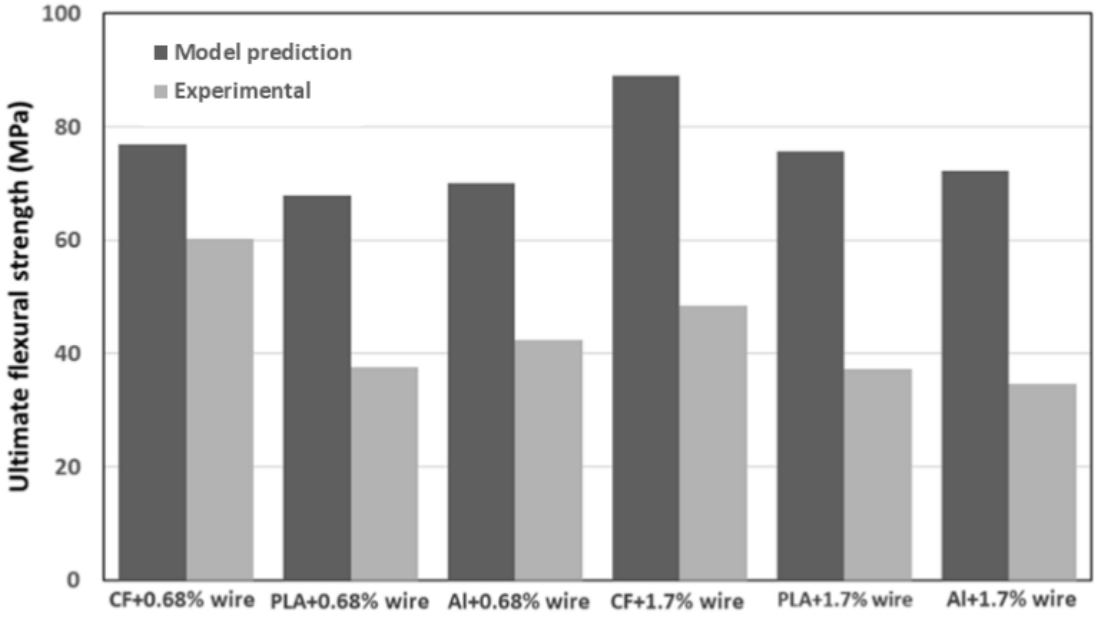

Figure 4-19 Ultimate flexural strength of printed samples

In addition to assuming perfect bonding between the matrix and the wire, the equivalent area approach uses the maximum stress theory to predict the failure. As the failure is

dominated by the matrix material, the composite will tend to follow the maximum strain theory where the composite initially fails when one of its components reaches its maximum strain then the loading continues until the other component fails known as progressive failure. In the current study, the matrix material failed initially as shown in Fig. 4-19 while the wires were still intact. Further loading would have been possible until the wires fail completely. However, the tests were stopped when the 0.05 mm/mm strain limit was reached according to the ASTM D770-17 standard [66].

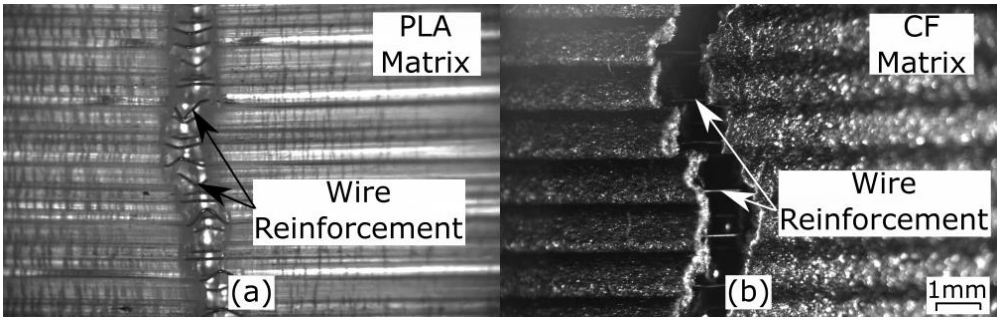

Figure 4-20 Fracture surfaces for (a) PLA and (b) CF wire reinforced samples

4.3. Summary

3D printed CWPCs samples showed improved mechanical properties compared with the non-reinforced polymer samples. The reinforced samples exhibited a 9% improvement in the tensile modulus using copper wires and 30% improvement using nickel-chromium wires for a 0.7% nominal wire volume fraction. The effect of the wire volume fraction was investigated for the nickel-chromium wires where 1.7% wire volume fraction samples were created; these showed a 33% modulus improvement compared with the non-reinforced PLA samples. Metal powder reinforced filament was implemented to investigate

the effect of the matrix type on the samples' behavior and showed superior enhancement. The CWPCs based on the reinforced filament showed a 50% modulus improvement and 27% ultimate strength improvement compared with the reinforced filament without wires.

Flexural properties of 3D printed CWPCs were also investigated to characterize the effect of matrix material, continuous wire reinforcement volume fraction and wire surface treatment on both ultimate flexural strength and flexural modulus. DoE was employed to study the effect of each parameter separately on the flexural properties. Matrix materials which included chopped carbon fibres and aluminum particles in conjunction with the continuous wires showed significant improvement on the flexural strength and modulus compare to wire reinforced PLA samples. Nozzle diameter which dictates different wire volume fractions showed similar improvement on the flexural properties, namely that higher the volume fraction of the wire, the higher the ultimate flexural strength and modulus will be. On the other hand, wire surface treatment showed an insignificant effect. It is believed that the method used for wire treatment had the effect of weakening the wire by effectively reducing the wire cross-section area.

Generally, the wire CWPC samples showed flexural properties enhancement for both pure and discontinuous composite filaments. Wire reinforced carbon fibre matrix specifically yielded the maximum ultimate strength of 107 MPa when printed with the 1.7% wire volume fraction while the non-reinforced sample resulted in a maximum ultimate strength of 89 MPa when printed with the same wire volume fraction. Similarly, the flexural modulus was 6.2 MPa for the reinforced samples compared to 5.5 MPa for the non-reinforced ones.

Two approaches for flexural stress calculation were described to modelling CWPC bending: The first considers the CWPC as a homogenous material while the other uses transformed section method to find an equivalent area of the reinforcement. Both approaches have their own limitations: the first approach assumes homogenous material while the second approach one assumes perfect bonding—neither assumptions are strictly valid. However, values for ultimate flexural strength and modulus were obtained by the two approaches which can be used as a reference for the design of CWPC beams.

Progressive failure was expected for the created samples as the wires where still intact after the matrix material failure. However, it was not experimentally quantified as the current study followed the ASTM D790-17 for bending of reinforced plastics which limits the maximum strain to a 0.05 mm/mm strain limit.

The introduction of continuous wire reinforcement to 3D printed components to create CWPCs has demonstrated improvement to the tensile and flexural properties of the fabricated components. This technique can be extended to create CWPC supporting beams like T, C and L sections (Fig. 7-1). Future work in this area should address enhancement of the adhesion between the wire reinforcement and the matrix material by exploring alternative wire treatment methods. Moreover, the progressive failure of these kind of composites should be examined.

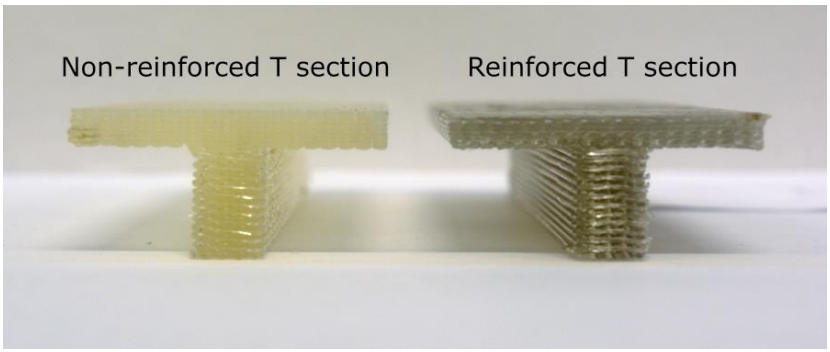

Figure 4-21 Wire reinforced and non-reinforced T sections

Chapter 5 Fabrication and Testing of CWPC Heater Panels for Anti/De-Icing Application

In this chapter, we extended the application of the proposed manufacturing process to develop a method of designing and manufacturing 3D printed heaters for low temperature applications and to demonstrate this system for an electrothermal anti/de-icing system. Design elements such as polymer and wire materials, wire diameters, printer modifications, as well as shape, pattern and number of layers for printing heating elements were considered. Analytical thermal analysis of the system was made prior to fabrication to predict the temperature distribution across the panels and ensure compatible temperatures with the materials used and these details are discussed herein. The feasibility of this heater fabrication technique was evaluated by constructing rectangular test panels and characterizing their icing mitigation capabilities during a field test on board a ship sailing in the Arctic Circle. The active system was combined with a hydrophobic coating passive technique to examine the possibility of reducing power consumption of the panels.

5.1. Design and Manufacturing Technique Of 3D Printed Heater Elements

The proposed fabrication technique of CWPCs offers wide range of application. This includes, not only mechanically reinforced structures, but also 3D printed heaters. The continuous network of wires within the CWPCs can be used to supply heat to the printed components thanks to the Ohmic resistance. Since the wire is intact, electric current can be supplied to the wire's terminal in order to act as a heating element. This will facilitate the

fabrication of components with embedded electric heating elements or 3D printed heaters.

This fabrication approach for a heating element affords a great deal of flexibility in terms of design space. Design parameters such as the polymer and wire materials, nozzle and wire diameters and overall heating element length, shape, pattern and number of layers can all be varied through the design process depending on the application requirements.

The heating element design process goes through different stages as shown in Fig. 5-1. The total resistance (R_{Req}) of the wire and the current through (I_c) can be inferred based on the required dissipated power (P_{elec}), heater shape and the available voltage source (V) given by

$$R_{Req} = \frac{V^2}{P_{elec}} = \frac{P_{elec}}{{I_c}^2} \tag{5-1}$$

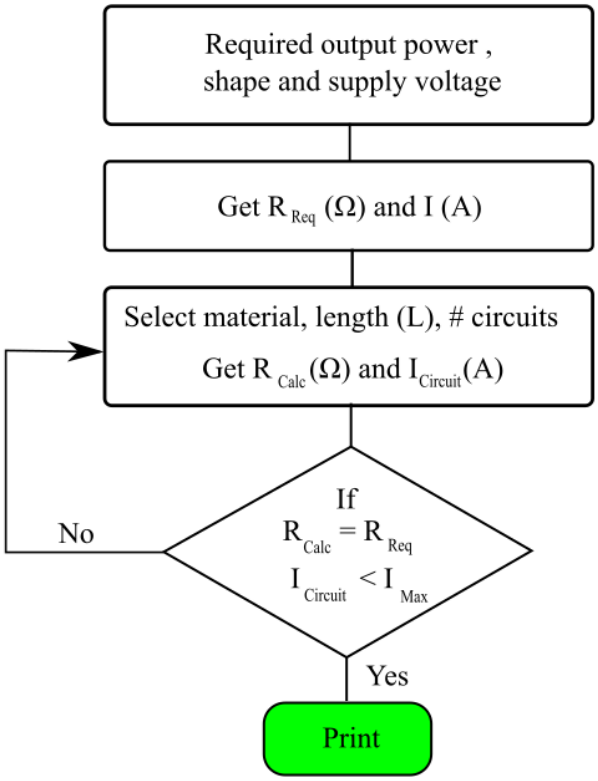

Figure 5-1 Heating elements design process.

The wire material, which defines the wire resistivity (ρ), and Area (A_w) and length (L) are then selected to achieve the required resistance based on the wire material resistivity as

$$R_{Calc} = \frac{\rho L}{A_w} \qquad (5\text{-}2)$$

Thereafter, the configuration of the calculated wire length can be designed to obtain the best heat distribution upon the heating element. Good distribution of the wires across the printed part will ensure even heat dissipation and temperature uniformity. The location of the embedded wires and the polymer layers are controlled by the printing code which defined all the printer movement.

For example, in this study a heat flux of 10 kW/m^2 over an area of 0.06 m^2 was required. The maximum voltage of our power supply was 120 VDC, therefore the required resistance of the heating element should be 23 Ω and the current drawn was 5 A.

Although the printing technique offers a range of wire materials and diameters, in some cases the required power is unachievable due to the constrains on the maximum allowable current for a given wire diameter or the availability of the wire material to have the required resistance with a reasonable length as described in Chapter 3. One solution is to use a different voltage source to reduce the past current through the wires. Alternatively, the 3D printed circuits can be divided into smaller sub-circuits which can be connected in parallel to reduce the total resistance of the heating element. Parallel sub-circuits can also offer better heat distribution control across the heating element as it can offer more wire material per unit area without increasing the total resistance of the heater. Furthermore, it divides the total current which result in lower current in each sub-circuit ensuring that the drawn current is less than the maximum current (I_{Max}) the wire can tolerate (Figure 5-1).

Printing with a polymeric material can be advantageous with regards to the ease of manufacturing of complex shapes and because polymers are electrically insulating which helps minimizes the chance of short circuits between adjacent wires. However, the main challenge for the printed heaters is the low melting temperature of the polymer which limit the applications of the created heaters. FFF printers usually utilizes polymer filaments with melting temperature ranging from 120 °C for wax up to 270 °C for fluorinated ethylene propylene (FEP) [61]. Thus, low temperature heaters such as those used in anti-/de-icing systems are an appropriate application of such a heater fabrication technique. The

technique presents a wide range of power supply range with very flexible geometrical aspects. In addition, anti/de-icing systems work at very low temperature which eliminates the risk of the polymer matrix melting. The fabrication process of 3D printed heated panels for anti/de-icing applications is described in the following section.

5.2. Design and Fabrication of the 3D Printed Electro-Thermal Anti-/De-icing System

5.1.1. Design Requirements

The proposed fabrication technique for heater elements using 3D printed CWPCs was applied to the manufacture of rectangular panels for an anti-/de-icing application. The panel's dimensions were 210 X 297 mm deemed to be suitable for field tests. Since anti/de-icing electrothermal systems implement relatively high-power consumption, this can increase the amount of current passing through the heating element wires. As such, the heating element was divided into two zones as shown in Fig. 5-2 (a) to split the current over two circuits. Another main design aspect was that the heater should provide a maximum heat flux of 10 kW/m^2 to maintain the heater surface temperature above freezing under sea-spray, winds and low ambient temperatures anticipated in arctic circle in late winter. The selected heat flux value was based on the available marine icing on offshore structures studies [74]–[76]. M. Mohsen *et al.* used 8.3 kW/m2 of heat flux for an electrothermal anti-icing system to keep an airfoil structure ice free at an 0.2 kg/min water loading rate for a lab-based experiment [77]. The design heat flux was selected to have an overhead power range for the worst-case scenario. Furthermore, the surface temperature of the panels was monitored and controlled using external power controller to minimize

the risks of overheating the panels.

5.1.2. Heating Element Fabrication

To meet the design requirements, the heating elements were 3D printed using continuous nichrome wire (McMaster-Carr, Ohio, USA) embedded in a PLA matrix (Spool 3d, Canada). The nichrome wire was selected as it has the suitable resistivity that achieves the required power density without exceeding the wire's current limit. A wire diameter of 75μm was used with a 1 mm nozzle diameter for the printing head. The polymer composite design was made to create flat heaters made of one layer of polymer with a thickness of 0.6 mm. The heaters were printed with a unidirectional rectilinear printing configuration with a printing angle of 90° to obtain an evenly distributed heat flux from the surface.

At the design power density (10 kW/m^2), the heater, which consists of two heating zones, draws 5 A which can easily melt the small heating wires in a single circuit. Subsequently, each heating zone was divided into nine sub-circuits to limit current draw when using for the 120 VDC power supply as described in Section 2. Each of the 18 heating circuits therefore draw only 0.27 A. The sub-circuits were connected in parallel as shown in Fig. 5-2 (a) by soldering the nichrome leads to a common copper tape which served as the terminal connection to the heater. 12 AWG lead wires were then soldered to the copper tape to establish external connections to the power supply.

The 3D printed heating elements and soldered terminals were then covered with a 0.03 mm thick layer of Kapton film as shown in Fig. 5-2 (b) to ensure electrically isolation between the nichrome wires, terminals and the carbon fibre cover installed in the next

step.

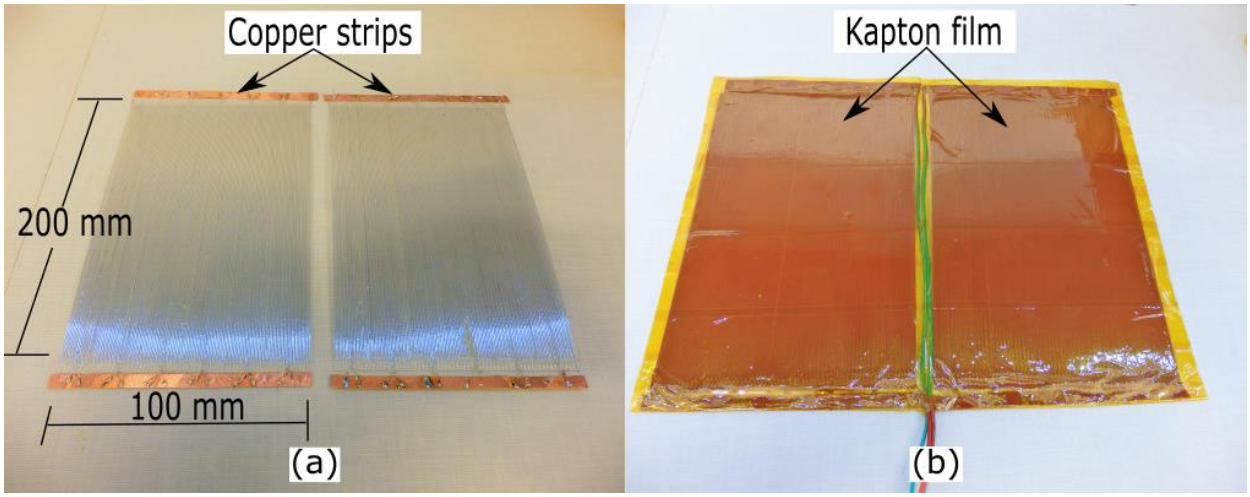

Figure 5-2 (a) Two parts of the printed heating element (b) Wire connections and Kapton film layer.

5.1.3. Heater Panel Fabrication

To fabricate a test material that can demonstrate the applications of anti/de-icing systems such as telecommunication dishes and wind turbine blades, which usually utilizes composite sandwiches, the printed heaters were sandwiched between two layers of 0.27 mm thick carbon fibre pre-preg (Rock West Composites, UT, USA) as shown in Fig. 5-3. Since uniform heat distribution is crucial for effective de-icing system, carbon fibre was selected due to its preferable thermal conductivity. Samples were autoclaved in a vacuum bag in a furnace at 100 °C. Before autoclaving, three T-type thermocouples were embedded in the panels between the heating element and the pre-preg to allow for estimation of the surface temperature of the heater at three different locations. The thermocouples were located at the centre of each heating zone and one at the top left corner of the panel as shown in Fig. 5-3.

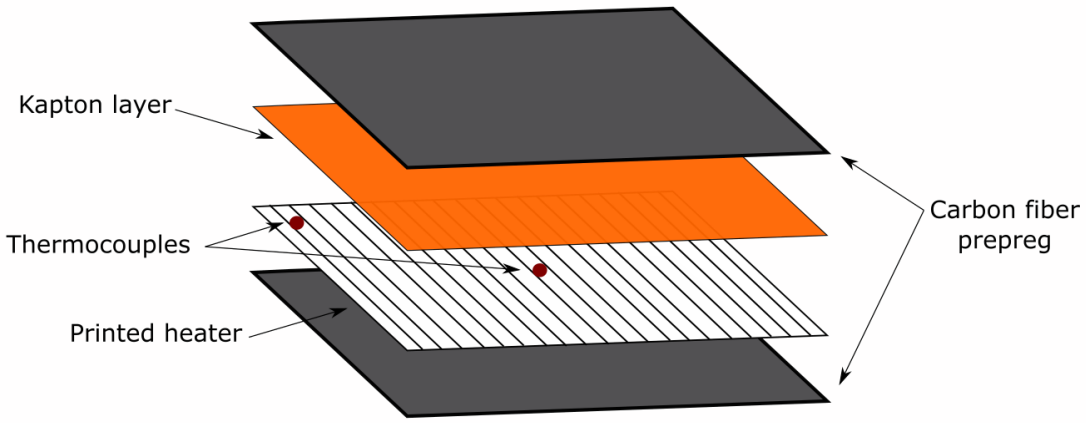

Figure 5-3 Heated panels layers schematic of one of the heating zones, i.e. the upper heating zone

5.1.4. Thermal Modelling and Analysis of Heater Panels

The temperature distribution in the heaters and the location of the maximum temperature was modeled analytically to ensure that the maximum internal temperature does not exceed the glass transition or the melting temperature of the polymer which could cause heating element dislocations when the heaters are energized.

A cross-section of the proposed heating panel is shown in Fig. 5-4 (a). Here the 3D printed heater element, which consists of the metal wires embedded in the printed polymer, was sandwiched on both sides by a layer of pre-preg carbon fibre.

Heat transfer in the panel was modelled by considering a single 2D unit-cell of the panel (Fig. 5-4 (a)) and representing heat transfer using the network of thermal resistances as shown in Fig. 5-4 (b). The individual thermal resistances in this model depend on the material's thermal properties and the designed dimensions of the wire and the matrix. The temperature values at all the circuit nodes, which represent different locations across the

heater, can be calculated using the simple form of Fourier law shown in Eq. 3 and 4.

$$q = \frac{\Delta T}{R_{th}} \tag{5-3}$$

$$R_{th} = \frac{L_D}{k} \tag{5-4}$$

For an ambient temperature (T_∞) of -20 °C and an outward surface heat flux of 10 kW/m^2, which were anticipated for the field testing, the corresponding maximum wire temperature inside the panel was found to be less than 70 °C which is lower than the glass transition temperature of the PLA plastic used to fabricate the CWPC heater elements. This means that the rigidity of the panels will be ensured at the anticipated testing conditions.

After fabrication, the internal structure of the heater panels was investigated to ensure that the selected unit-cell represents the real matrix-wire configuration. Figure 5-4 (c) shows a cross-sectional view of the fabricated panels showing the similarity between the selected unit cell and the actual panel configuration. Compared to the microscopic images made in Section 4.1.41 and 4.2.61, the wires were somewhat closer to the upper surface of the polymer. This might be caused by the autoclaving process because the temperature was higher than the glass transition temperature of the PLA and because of the vacuum effect.

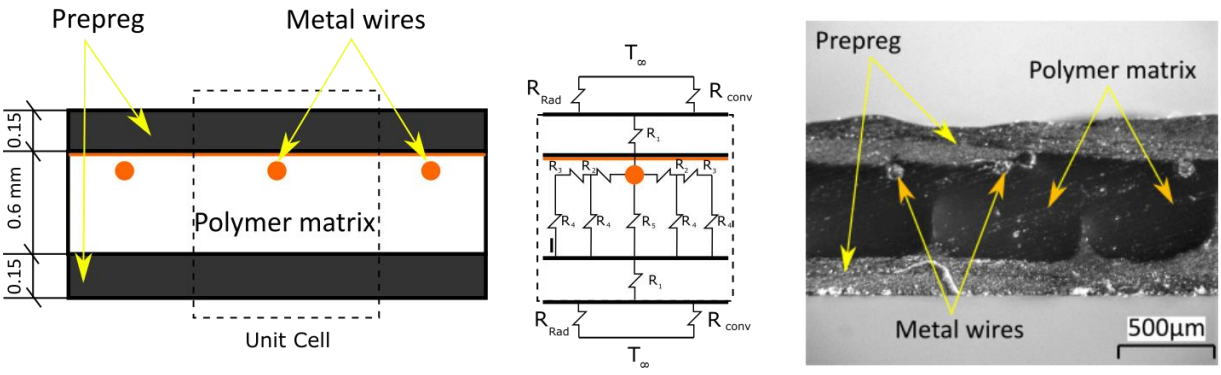

(a) (b) (c)

Figure 5-4 (a) Schematic unit cell for thermal analysis (b) Simplified thermal circuit (c) Microscopic image for heater panel cross-section.

5.1.5. Heater Panel Treatment

The energy required to keep the panels ice free depends mainly on the amount of ice formed or water loading on the panels. Therefore, using surfaces with low tendency of water to stick can reduce the amount of energy required [78]. Since super hydrophobic surfaces repel water, a commercially available super hydrophobic coating (NeverWet, Rust Oleum, USA) was used to cover two panels manufactured using the process described above. A comparison between the coated and un-coated panels is shown in Fig. 5-5. Here the hydrophobicity of the coated panel is clearly demonstrated by the beading of water droplets whereas water droplets tended to stick and wet the un-coated panel.

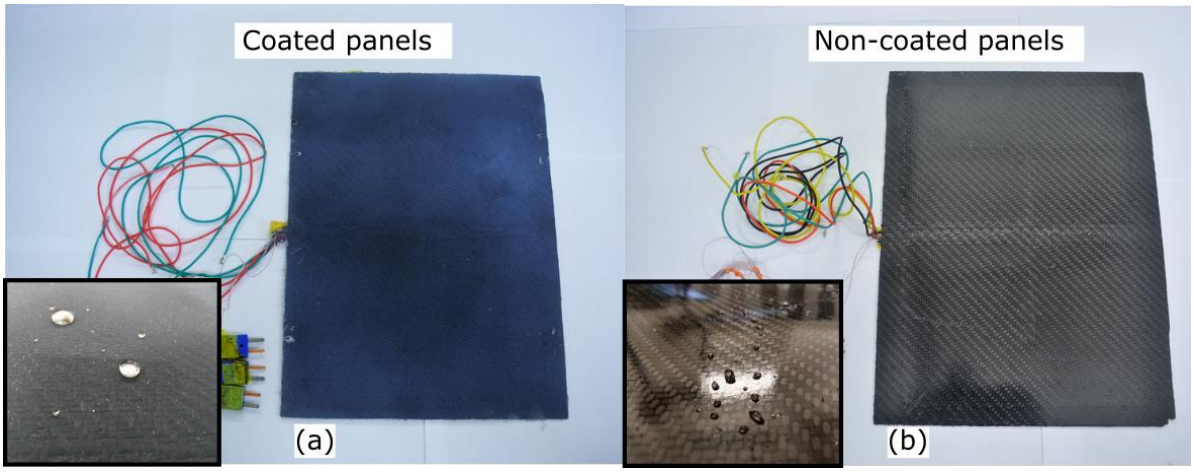

Figure 5-5 (a) Hydrophobic coated panel showing water droplets beading on the surface (b) Non-coated panel showing water droplets somewhat wet the surface.

5.1.6. Heater Panel Control

A simple "bang-bang" power control scheme was used to control the heater panel operation which supplies power to the system with a constant value as long as the temperature of the system is less than the set temperature and turns the power off when the temperature exceeds the set temperature. This on-off control scheme was implemented in MATLAB which controlled the DC power supply. The MATLAB script read the thermocouples temperature output and calculated the average temperature across the three thermocouples to decide whether to supply power to the system or not.

5.3. Field Testing

To demonstrate the feasibility of the 3D printed heating elements and composite heater panels in a real-world scenario, a field test was conducted on board a Nornen-class patrol vessel (The *NoCGV Farm*) in the arctic circle between March 5-8, 2018. The ship

experiences ice formations on different parts during its patrol duties, as shown in Fig. 5-6 (a) due to sea spray at sub-zero temperatures. The objective of the field test was to keep the surfaces of the fabricated panels ice free under severe conditions of sea spray, wind and low temperatures. Of particular interest was the difference in ice formation between the hydrophobic coated panels and the non-coated panels and how this affected the amount of energy required to keep the panels ice free.

The ship sailed in approximate route shown in Fig. 5-6(b). As the ships sails towards the north, the average temperature during the day dropped from -6 °C to -20 °C. The power control of the panels was designed to have a broad range of supplied power to make sure it can handle different temperatures and water loading conditions.

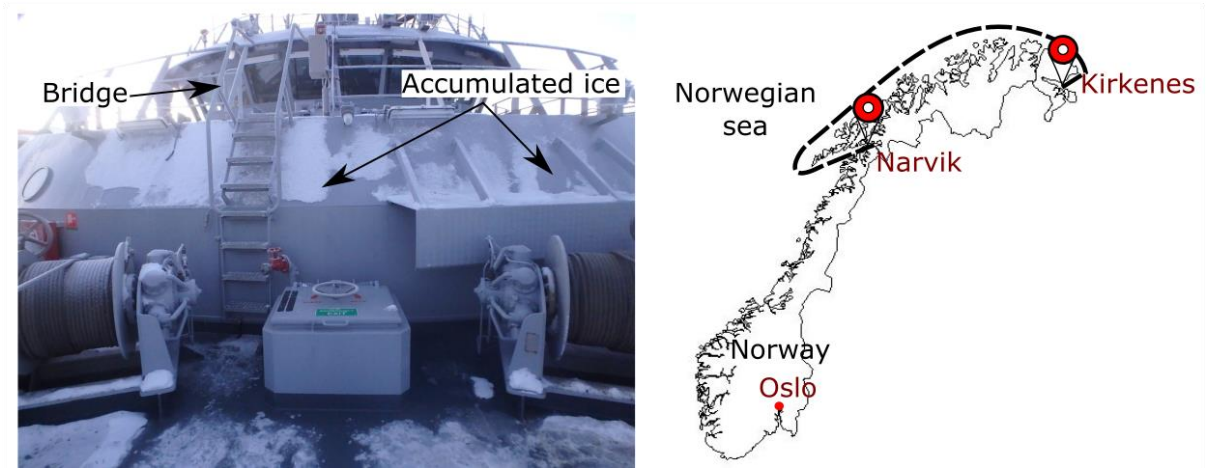

(a) (b)

Figure 5-6 (a) Ship deck showing ice formation on different ship equipment
(b) Field trip map showing route in dash line.

For the field test, four panels fabricated using the described method in section 3 were attached to the top surface of waterproof insulation boards as shown in Fig. 5-7. Panels P1

and P2 were un-coated while panels P3 and P4 were coated. Furthermore, panels P2 and P3 were energized and temperature controlled while panels P1 and P4 were not powered to evaluate the effect of active heating. The waterproof insulation board was fixed onto an Aluminium profile frame with adjustable facing angle. The frame angle was set to 90 degrees with respect to the ship deck by adjusting the frame arms. The panels were set to face the bow of the ship as it was the expected to be the direction most affected by the sea spray. One thermocouple was located in a sheltered position on the back side of the insulation board to record the ambient temperature throughout the tests.

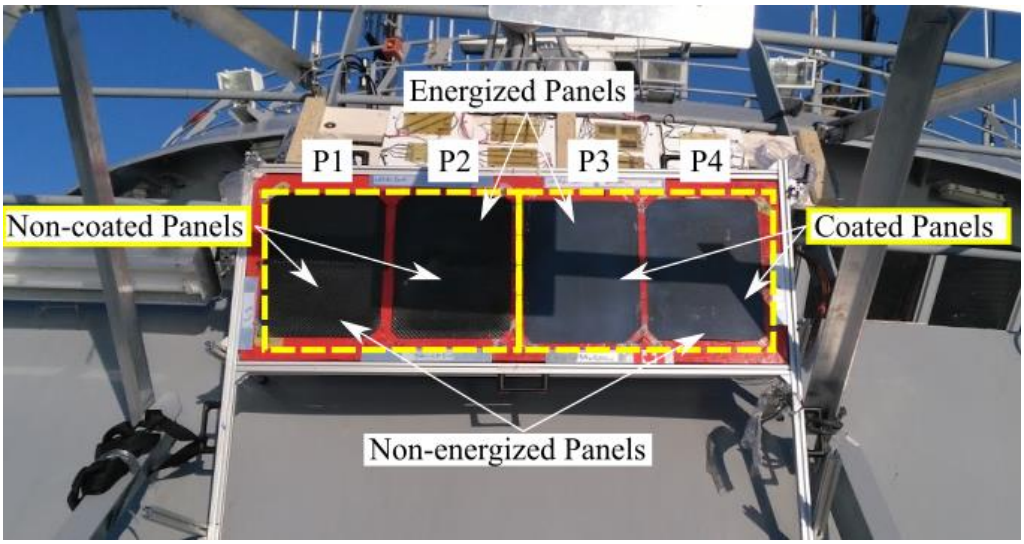

Figure 5-7 Coated and non-coated panels configuration mounted on the upper deck facing ship bow.

Two modes of operation were tested: de-icing and anti-icing. In de-icing mode, the ice was already formed on the panels and the power was supplied to melt the ice. This mode was operating in the early morning of the two days of testing where the ice accumulated on the panels during night. In the anti-icing mode, the system was set to run continuously over a given period to prevent any ice accumulation on the panels.

5.4. Results & Discussion

5.1.1. Temperature Distribution of Heater Panels

Pilot testing of the printed heaters under natural convection conditions showed uniform temperature distribution on the panels. Since the heating elements were closely stacked owing to the printing pattern used, the temperature distribution was expected to be fairly uniform. Using a thermal camera (FLIR systems, Inc., Oregon, USA), thermal images were taken for the panels. When the power was supplied to the system, heat is generated equally in the wires creating uniform heat flux upon the panels. The uniform heat flux over the panel creates almost equal temperatures on the panels except for the edge which has higher heat loss to the surrounding. Fig. 5-8 (a) shows the temperature distribution just after suppling power to the system and (b) after reaching the set temperature. The two heating zones were supplied with the same voltage and both coated and non-coated panels showed similar temperature distributions. From Fig. 5-8, a clear discontinuity in temperature is visible between the two heater zones due to the absence of any heating element in this region. Yet, the carbon fibre pre-preg helps conducting heat from the heated zones to the non-heated zones as it has higher thermal conductivity compared to the PLA resulting in minimizing the temperature drop in the gap in between.

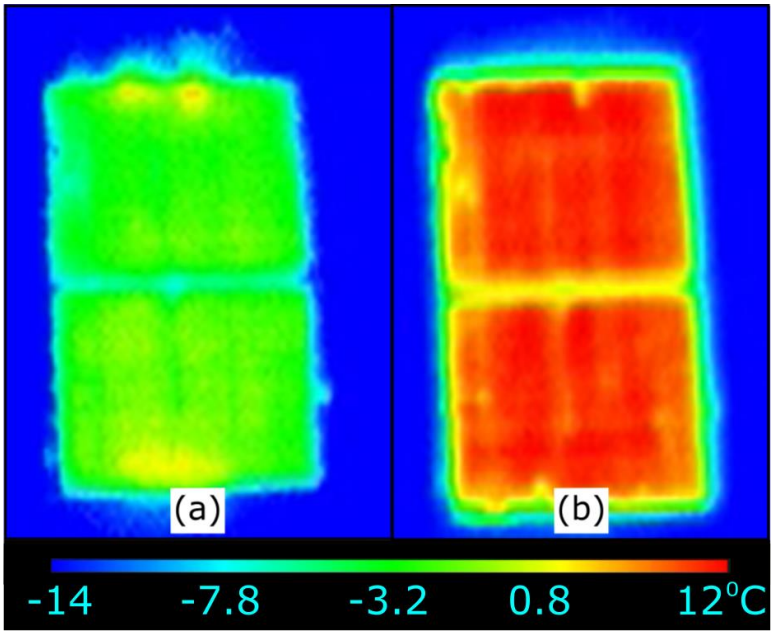

Figure 5-8 Temperature distribution for the heated panels (a) at the beginning of trial test (b) after reaching set temperature (10°C).

5.1.2. Ice Formation on Panels

At sea and overnight, the ambient temperature dropped significantly, and the turbulent conditions of the sea created a higher load of sea spray over the ship. At an average ambient temperature of -6 °C, it was found that ice easily accumulates on the non-coated panel in a non-uniform, roughly circular shapes with large diameters as shown in Fig. 5-9 (a). For coated panels, sea spray droplets freeze on the panels in the form of uniform small circular particles as shown in Fig 5-9 (b). Although the panels were coated and set on a vertical position, which help water droplets to shed easily in normal laboratory conditions, it seems that small water particles froze sufficiently fast to stay on the surface of the coated panels. It was noticed that the ice formed on the coated panels was easily removed using small brush while the ice on the non-coated panels was strongly stuck to the panel. This is

very similar to lab tests reported by Mangini *et al.* [22].

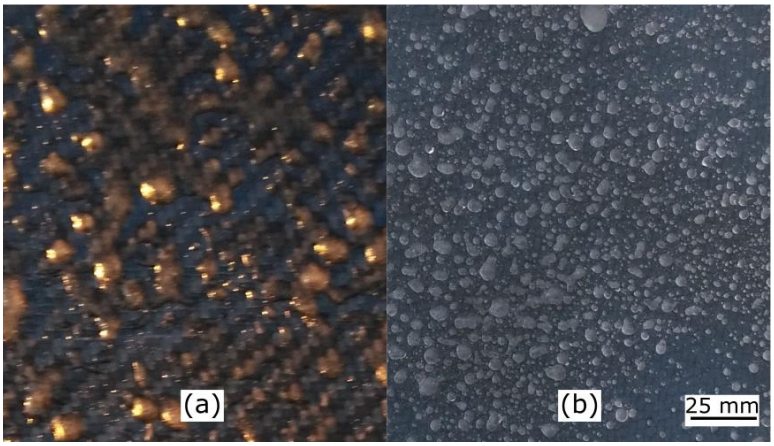

Figure 5-9 Ice formation at -6°C average temperature on (a) Non-coated panel (b) Coated panel.

Under different icing conditions when the average temperature dropped to -16 °C for test No. 2, again ice was found on both coated and non-coated panels. In this case, the ice found on both panels was in the form of very fine particles as shown in Fig. 5-10. The density of the ice formed on the non-coated panel was higher than that of coated panels. This means that the coating was effective in reducing ice formation on the panel. Despite absence of the exact sea conditions and size of droplets impinging on the panels, it was anticipated that the droplet size generated by sea spray and wind in the second day was finer which created smaller diameter ice particles.

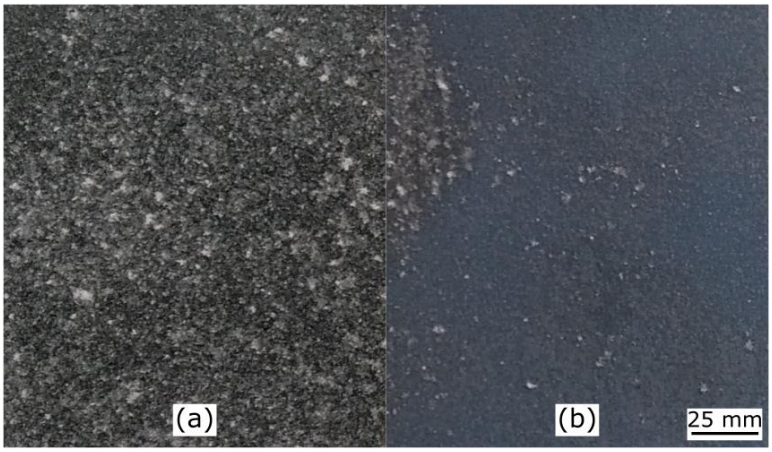

Figure 5-10 Ice formation on (a) Non-coated panel (b) Coated panel at -16 °C average temperature.

5.1.3. Ice removal modes

Onboard, water loading rate was variable over the day. Most of the sea spray was found to occur during late night hours and overnight. This makes it difficult to quantify water loading rate on the panels especially that the facility for accurate measurement was not available on board. Since the de-icing mode only requires the existence of ice on the panels, the mode was used in the early morning when the ice was already accumulated on the panels over the night. On the other hand, it was difficult to test the anti-icing mode during the day due to the lack of sea spray. As such, to perform anti-icing tests on the panels, an artificial spray was created during daytime using the ship fire hoses which sprays sea water with different rates.

In the early first test, the power supplied to the heaters when the controller was “on” was set to 30 W. The system was found to take around five minutes to melt the ice and reach the set temperature at an ambient temperature of -6 °C. A quicker ice removal effect was

desired in such environments especially for critical applications such as communication devices. As a result, the input power was changed to 78 W in the preceding tests to reduce the ice melting time. Table 5-1 summarizes the testing conditions for the anti/de-icing modes. The de-icing mode test was performed on two days with different ambient temperature while the anti-icing mode tests were performed over different hours through the same day.

Table 5-1 Test conditions, supplied power, mode of operation, test duration and average ambient temperature for each test.

Test No.	Mode	Duration (min)	Power (W)	T_{amb} (°C)	Notional water loading
1	De-icing	5	30	-6	-
2	De-icing	5	78	-16	-
3	Anti-icing	9	78	-17 to -10	Low
4	Anti-icing	9	78	-12	Medium
5	Anti-icing	9	78	-12 to -8	High

5.1.4. De-icing Mode

The first de-icing mode test was conducted at an average ambient temperature of -6°C where ice was already formed on the panels overnight. A plot of the temperature response of the panels over the course of the 5-minute test is shown in Fig. 5-11. From this we can observe that the non-coated panel (P2) just barely achieved the set temperature of 10 °C by the end of test. The long time needed by the non-coated panel to reach the set temperature is due to the effect of the thick layer of ice formed on the panels as shown in Fig. 5-9 (a). On the other hand, the coated panel was able to reach the set temperature in less than a minute. This was because there is less ice formed on the coated panels and the contact between the iced droplets and the panel is minimum with the coating.

Cumulative energy dissipated by panels P2 and P3 was calculated based on the power supplied to the panel and the duration of the "on" state in the control scheme; this result is plotted on the secondary axis of Fig. 5-11. The coated panel was found to consume only 76% of the energy consumed by the non-coating panel saving 24% of the energy. Similar levels of energy savings were observed in lab-based testing conditions by Antonini *et al.* [78] and Zhao *et al.* [79].

Figure 5-12 (a) and (b) shows both panels after the de-icing mode test. The residual ice on the middle of the non-coated panel and the sides of the coated panel was due to the location of the heating zones within the panels and the lack of heater wire directly under the two heated zones as described in Fig. 5-2 (b). However, the coated panel was able to clear the ice in the middle due to the less adhesion and accumulation of the particles on the surface.

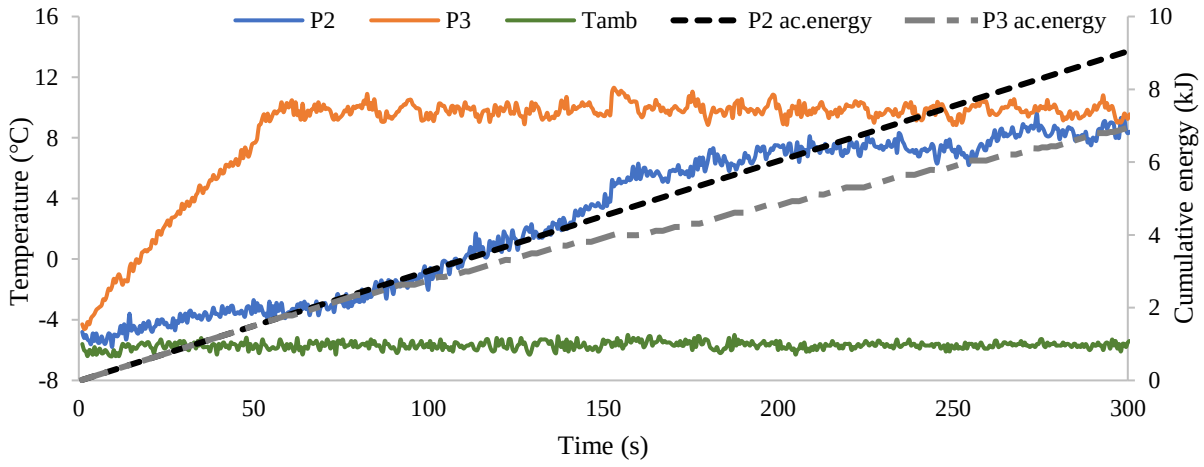

Figure 5-11 Average temperature of coated panel (P2), non-coated panel (P3) and ambient temperature with the cumulative energy of both panels for test No.1

The de-icing mode was tested again in the next day (test No.2) at a maximum input power of 78 W investigate the effect of the input power change. On this occasion, the ice layer was thinner compared to test No.1 as shown in Fig. 5-10 because the colder the temperature, the probability of formation of thick glaze ice is reduced. The two panels were able to reach the set temperature within the first minutes with the coated panel leading by 15 seconds. Figure 5-12 (c) and (d) shows the two panels after five minutes of testing. Again, the middle of the non-coated panel and the sides of the two panels were still covered with ice.

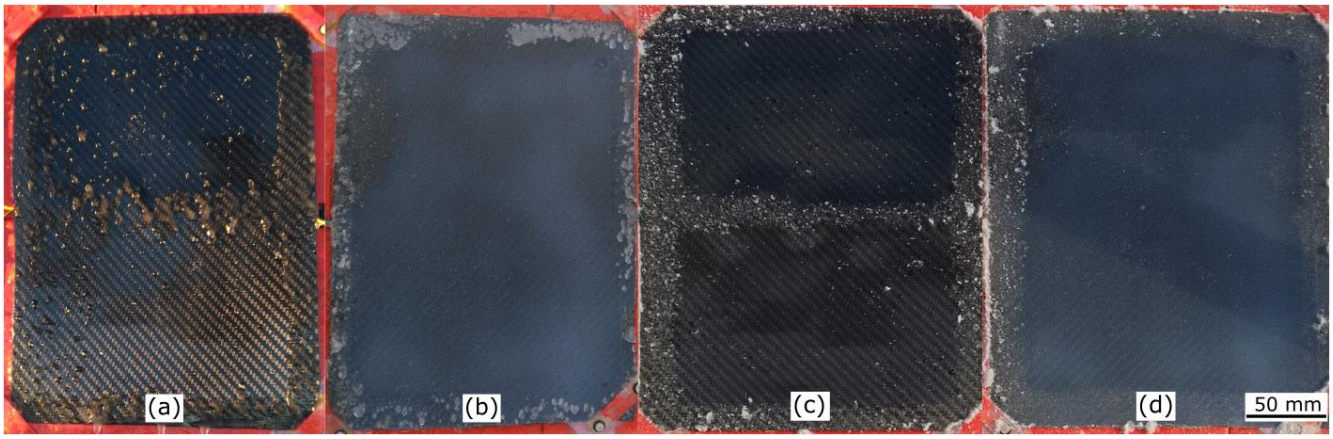

Figure 5-12 Images from coated and non-coated panels after five minutes of de-icing mode, (a) and (b) for test No.1, (c) and (d) for test No.2

It was observed that the hydrophobic coating was deteriorating with time especially with the sea salt collected on the panels. This supports the need for hydrophobic coatings that can withstand more contaminated environments. For applications where, hydrophobic coating independently can be sufficient to keep surfaces ice free, it also important to combine the coating with an electrothermal de-icing system which will aid the coating performance when the coating starts to deteriorate.

5.1.5. Anti-icing Mode

In this mode, the system was energized while the sea water was sprayed on the panels. The test was conducted under three different water loading rates; low, medium and high loading. The three loading rates were created by changing the frequency of directing the water spray toward the panels. Three power schemes were obtained through the three anti-icing tests. Due to the lack of the measuring facility of the water loading on the ship, the three loading rates were visually verified by observing three different droplet cloud intensities. The loading rates were also verified through obtaining three different power schemes for each test.

The temperature response of P2 and P3 for test no.3 is shown in Fig. 5-13. In which, the cumulative consumed energies by the panels were plotted on the secondary axis. Over the nine minutes of testing, the ambient temperature increased from -16 °C to -10 °C as recorded by the ambient thermocouple, which was still below freezing temperature. The temperature build-up slope was steeper in case of P3 causing the panel to reach the set temperature ten seconds before P2 since water droplets have a smaller contact area and shorter contact time with the coated panel. Cumulatively, P2 panel consumed almost 16 kJ of electric energy while P3 consumed only half of this value at the low water loading conditions. In addition, it was noticed that the coated panel showed a better temperature stability around the 10°C set temperature compared to the non-coated panel which reached a temperature as low as 4°C. This was probably caused by the quenching effect that the water exerts on P2 causing the temperature to drop more significantly. In contrast, the coating on P3 reduces this effect creating more stable temperature. Similar

temperature response was observed for tests no.4 and 5 with higher values of cumulative energies and less temperature stability on P2.

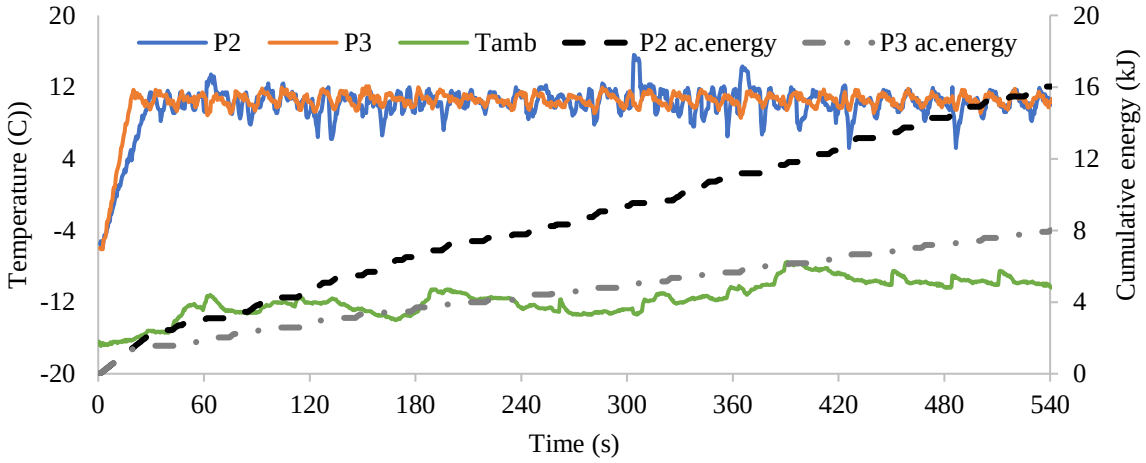

Figure 5-13 Average temperature of coated panel (P2), non-coated panel (P3) and ambient temperature with the cumulative energy of both panels for test No.3

By dividing the cumulative energy over the test duration, an equivalent average power can be calculated. The average power calculated gives the same ice prevention effect on the panels when supplied continuously. Figure 5-14 shows the average dissipated power for P2 and P3 at the three different water loading rates created. Generally, the coated panel utilized less average power than the non-coated one. The power saving depends to a certain degree on water loading and it was found that coated panel consumed around half of the power consumed by the non-coated one as shown in Fig. 5-14. The saving in the consumed energy by the coated system in the real-world scenario was found to be less than what was reported in a lab-based experiment. Antonini *et al.* [78] obtained up to 80% of energy saving by combining the electrothermal heating system with hydrophobic coating

while Zhao *et al.* [78]obtained up to 53% of energy saving. This can be due to the different testing conditions and the nature of the sea spray loading compared to constant water loading rates obtained in lab.

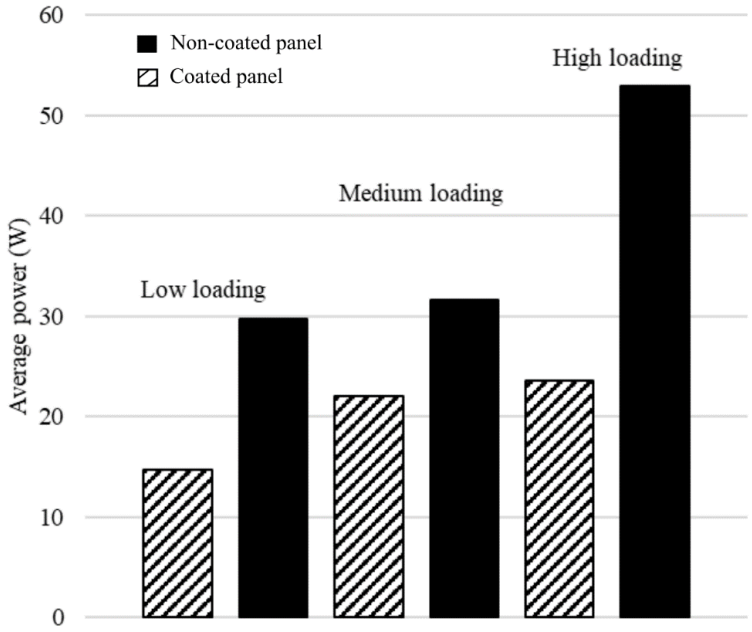

Figure 5-14 Average consumed power of coated and non-coated panels at three different loading rates.

5.5. Summary

A method of fabricating 3D printed heating elements was developed and used to fabricated heated panels for anti/de-icing application. Energized and non-energized panels were tested in real life scenario onboard of ship sailing in the Arctic Circle to investigate the feasibility of the heating system. The energized heater was effective in keeping the panel surface ice free and creating uniform temperature distribution on the panel. Hydrophobic coated panels were also tested to examine the effective of passive de-icing system under sea spray icing. Energized coated panel was sufficient in keeping the surface ice free with

less electrothermal energy compared to the non-coated panel. On the other hand, ice accumulated on the non-energized coated panel. With almost half energy consumption, the combination of the heating element and coating was the most effective method in keeping the panels ice free for both anti/de-icing modes compared to the usage of electrothermal anti/de-icing systems. The proposed manufacturing technique showed significant design flexibility and anti/de-icing action feasibility in real life conditions. This makes it a convenient choice for fabricating light weight, and complex shaped protective shields for valuable components subjected to icing conditions. Future work can investigate the use of higher melting temperature polymers to further expand the operational application range of this fabrication technique.

Chapter 6 Investigation of Effective Thermal Conductivity of CWPCs

CPWCs are expected to present higher thermal conductivity than composites with discontinuous fillers because they contain a continuous network of conductive filler. This network will aid heat transfer inside the material and reduce the effect of the interfacial resistance that exists between the filler and the matrix in case of discontinues filler. Many applications can make use of 3D printed conductive materials and especially heat exchanging applications. The ability of creating complex shapes as a single part without the need for further machining or welding make 3D printing of conductive materials very attractive for the heat exchangers industry. As well, polymers are less dense than metals which make them more suitable for light weight applications such as for electronic cooling and aerospace applications. We believe that replacing metals with conductive polymers can significantly reduce heat exchangers weight as well as improve their performance.

In this chapter, we investigated the effective thermal conductivity of CWPCs. We studied the effect of printing parameters such as printing direction, matrix material and wire volume fraction on the effective thermal conductivity of the composite. The thermal conductivity was experimentally measured using a steady-state testing facility which was designed to measure materials with low to medium thermal conductivity. In addition, the thermal conductivity modelled analytically using the rule of mixture thermal model. We also investigated the effect of the contact resistance on the measured thermal conductivity.

6.1. Design and Fabrication of AM CWPC Samples for Thermal Characterization

6.1.1. Wire Material and Diameter

Once again, the printing process developed in Chapter 3 was used to fabricate samples for thermal conductivity characterization. As demonstrated in the previous chapters, there are different options for wire material that can be used with this technique such as Nichrome, copper, and aluminum. Generally, copper and silver present the highest thermal conductivity of all metals which make them the best candidates for improving the thermal conductivity of the polymer. Since copper wires are more commonly used for electrical applications and commercially available with different sizes, it was selected as the filler material.

Material	Thermal conductivity [61]
Copper	398
Silver	419
Aluminium	167

Wire diameter along with the nozzle diameter will affect the effective thermal conductivity of CWPCs because it changes the volume fraction of the conductive filler. As shown previously, increasing wire diameter at the same nozzle diameter will increase the effective thermal conductivity of the composite. However, it is preferred that the wire diameter does not exceed one tenth of the nozzle diameter otherwise there might be insufficient amount of polymer to support the wire as described in Chapter 3. Here, we used a 30 AWG gauge copper wire (0.075 mm diameter) (McMaster-Carr, Ohio, USA) . The un-coated wires allow for potential thermal interaction between the wires and any discontinuous filler exist in the matrix or the adjacent wires which will aid the effective thermal conductivity. The wire volume fraction was varied by using two nozzle diameters (1 mm and 0.6 mm).

6.1.2. Printing parameters

Printing pattern is another key factor which dictates the material properties of the CWPC.

Usually, preferable properties are obtained along the wire axis direction because there are less phase transitions between polymer and wire in this direction. This will reduce the number of interfacial resistances in the heat flow direction and subsequently increase the effective thermal conductivity in this direction. We used two printing patterns to investigate its effect on the effective thermal conductivity. The first configuration is the lines pattern, in which the rasters are aligned unidirectionally (Fig. 6-1 (a)). This pattern is anticipated to offers the maximum thermal conductivity when the heat is conducted through the wires' axes (Parallel direction). However, in the transverse direction, minimal thermal conductivity will be obtained since the wire and polymer will be in series [80].The second pattern is the grid pattern, in which each layer of rasters is printed alternately such that half of the rasters are printed in the direction of heat flow while the other is printed in the transverse direction (Fig. 6-1 (b)). Although this pattern sacrifices half of the conductive filler in axial direction, it improves the effective thermal conductivity in the transverse direction. This will facilitate the fabrication of a material with similar in plane thermal conductivities (k_{xx}=k_{yy}) which in desired in some thermal applications.

Other printing parameters such as printing temperature and speed are expected to exert less effect on the effective thermal conductivity of the composite. These parameters will affect the mechanical properties of the composite more significantly by affecting the adhesion between the rasters and the amount of air voids content [25]. For CWPCs, matrix adhesion and air voids existence will have less effect on the effective thermal conductivity especially when heat is conducted along the wires' axes. The main printing parameters are summarized in Table 6-1.

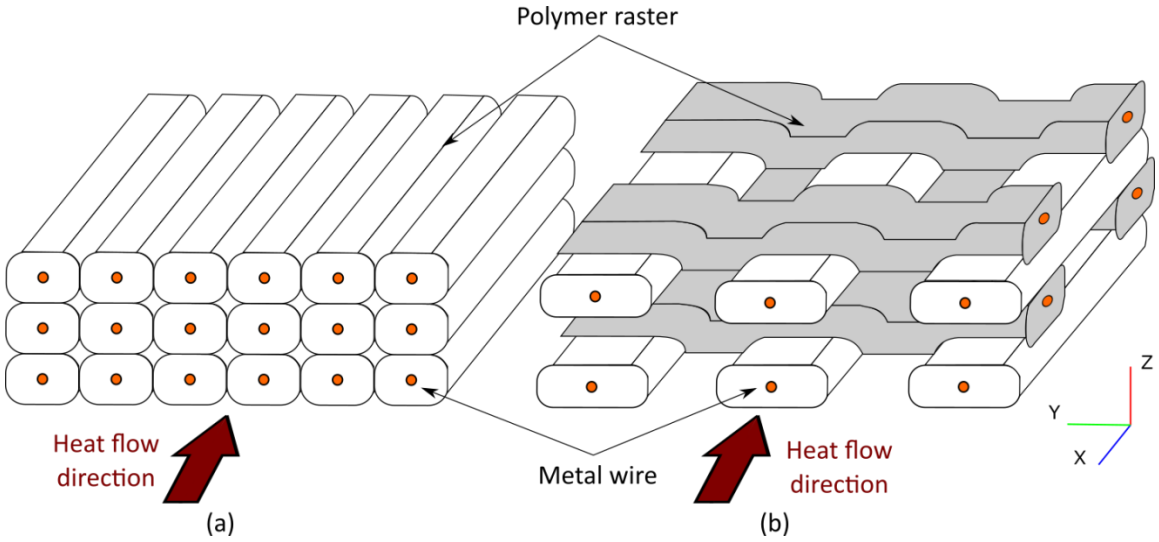

Figure 6-1 Schematic of printing patterns (a) lines (unidirectional) and (b) grid (bi-directional)

Table 6-1 Printing parameters

Layer height (mm)	0.2-0.6
Raster width (mm)	1.05- 0.65
Printing speed (mm/s)	10
Printing temperature (°c)	190
Printing angle (°)	0 – 0,90

6.1.3. Sample Dimensions

The outer dimensions of the printed samples designed to fit onto the used measurement facility. The samples have a cross-sectional dimension of 40 X 40 mm. The printed sample thickness was 25 mm (in the direction of heat flow) which was then reduced in thickness by multiple stages of grinding and polishing to prepare it for testing. The samples were designed on a CAD software (SolidWorks 2017, Dassault Systems, Waltham, MA).

Thereafter, the output model was imported into the printer slicing software (Slic3er, Prusa Research, Prague, Czech Republic) where the printing parameters are selected, and the printing g-code is generated.

6.1.4. Matrix Materials

Matrix material also has a significant role on the effective thermal conductivity of the composite. The more conductive the matrix is, the less anisotropic the composite will be. Since the wire volume fraction is limited, increasing the matrix thermal conductivity could further improve the effective thermal conductivity of the composite. Printing filaments with discontinuous conductive fillers are commonly used now to print more durable and better-looking 3D printed parts. Above percolation ratio, the discontinuous filler can boost the thermal conductivity of the matrix. As such, two base polymers and polymer composites where used for this study. The first is a transparent PLA which was chosen for the base matrix of the printed composites for its relative ease of printing and because its thermal conductivity has been well characterized [81].

The second base material was a discontinuous PLA composite consisting of 80% of copper particles. Although this percentage was not proved to be greater than the percolation threshold, it was anticipated that this matrix will present higher thermal conductivity than pure PLA. As such, we used the copper filled PLA matrix to investigate the effect of the matrix on the composite properties and explore any interaction between the continuous and the discontinuous filler to further improve the composite thermal conductivity. Additional details on these two matrix materials are presented in Table 2.

Table 6-2 Matrix materials and suppliers

Matrix material	Supplier	Discontinuous filler percentage (%)	Density (g/cm^3)
PLA	Spool 3d, Canada	-	1.25
PLA + copper	Formfutura, Nijmegen, Netherlands	80	3.5

6.1.5. Sample Configurations

Samples with different configurations, filler content and matrix material were printed to investigate the effect of these parameters on the effective thermal conductivity of the 3D printed CWPCs and these are summarized in Table 3. Three replicates of the wire reinforced samples were printed to verify the repeatability of the testing and the consistency of the printing process. Pure PLA and copper filled PLA samples were printed to obtain the thermal conductivity of the base matrix. The two matrixes are homogenous and have isotropic properties which means that their thermal conductivities will not be affected by the printing pattern. The continuous filler contents presented in Table 3 are based on the nominal dimensions of the wires and the matrix rasters.

Table 6-3 Summary of samples configuration

Sample No.	Matrix material	Discontinuous filler	Infill pattern	Infill percentage (%)	Continuous filler	Nominal Continuous filler content (%)

1	PLA	None	lines	100	None	None
2	PLA	copper	lines	100	None	None
3	PLA	None	lines	100	copper	0.68
4	PLA	None	Grid	100	copper	0.68
5	PLA	copper	lines	100	copper	0.68
6	PLA	None	lines	100	copper	1.7

6.2. Sample Preparation and Microscopy

The samples should have a very smooth surface in order to aid heat transfer into the samples and measure their thermal conductivity on a steady state test rig. This will require multiple stages of grinding and polishing for the samples. Otherwise, contact resistance in between the samples and the test rig will dominate the heat transfer and affect the measured values. Also, it was desired to investigate the internal structure of the printed samples using a microscope to get more insights on the wire-polymer configuration and to further understand the interaction between the two of them. As such the samples were sent through 5 stages of grinding and polishing. Using an auto polishing machine (Ultrapol End & Edge Polisher, ULTRA TEC Manufacturing Inc, USA), the samples were firstly grinded using a 60-grit polishing disc. Thereafter, 180,280,600 and 1200/400 polishing discs were used until obtaining smooth surface. Figure 6-2 demonstrates the printed samples after the grinding and polishing process. The surface roughness of the polished samples was then measured using an optical profilometer (Brucker, Massachusetts, USA) to ensure that the sample got similar polishing and was found to be closely similar for different samples.

Optical microscopy analysis was performed using the (LEICA MZ10 F, LEICA, Germany) optical microscope. The obtained images were imported into an image processing software

(ImageJ, National Institutes of Health, Bethesda, Maryland, USA) to accurately quantify the continuous filler content. The images were firstly thresholded to segment the wires from the adjacent polymer and the wires area was measured. Then, the percentage of the continuous filler was calculated based on the ratio between the wires area and the total area of the sample.

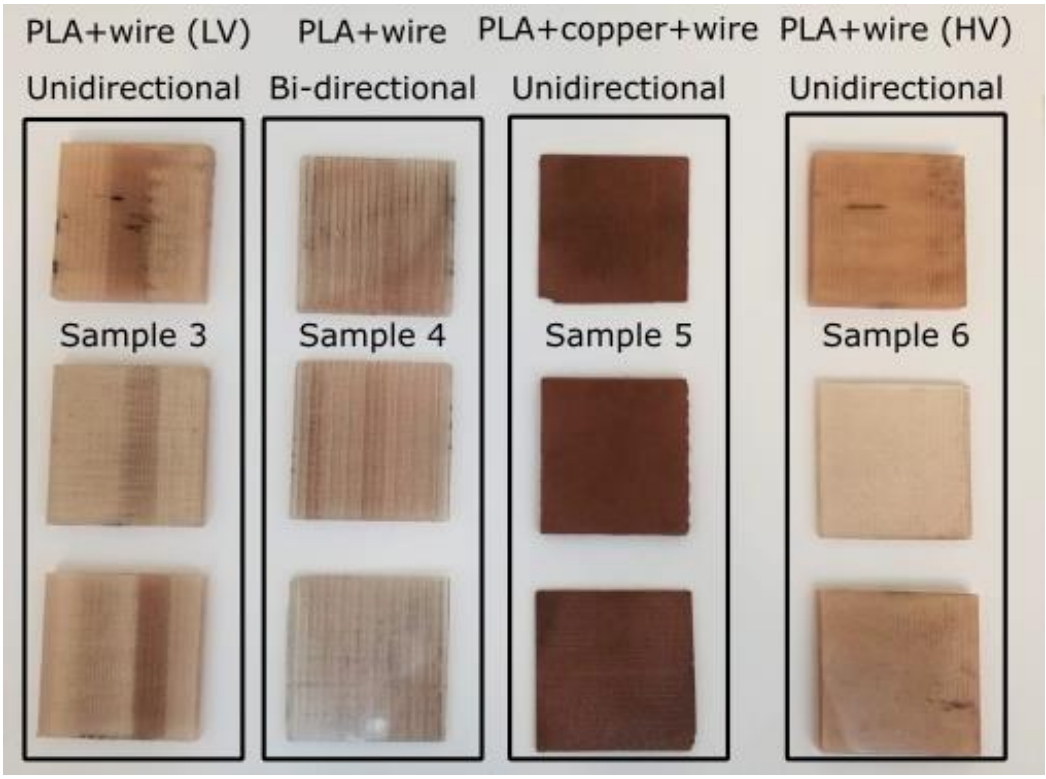

Figure 6-2 3D printed CWPCs thermal samples showing wire reinforced samples with low-volume fraction (LV) and high-volume fraction (HV)

6.3. Modelling the Effective Thermal Conductivity of CWPCs

The effective thermal conductivity of polymer composites can be predicted analytically

using theoretical models [38]. Depending on the filler material, shape and orientation, an analytical model can be chosen to predict the effective thermal conductivity. One basic model is the rule of mixture which describes the composite thermal conductivity as a function of only the constituents' thermal conductivity and volume fraction. The rule of mixture does not account for the interfacial resistance between the constituent phases. However, it can adequately describe CWPCs properties. In CWPCs, the three major material phases are the polymer, wires and air in the form of voids. The three constituents will influence the effective thermal conductivity based on their configurations. For the printing configurations used in the present study, the effective thermal conductivity of the CWPCs can be modelled using a using as a network of thermal resistances which are used to model the heat flow through the constituent components of the composite. These resistances will depend on the properties of the different phases and their geometrical configuration with respect to the direction of heat flow.

Conduction heat transfer in solid material is governed by Fourier's Law which can be put in the form of (6-1) for 1D steady state heat transfer. The thermal resistances can be obtained using a simple analogy between heat flow and electric current flow in a material. In heat transfer, the temperature difference (ΔT) represented the motive for the heat transfer (Q) like the voltage difference (ΔV) is the motive for current flow (I) . The thermal resistance of a material can be represented as in (6-2)

$$Q = kA * \frac{\Delta T}{L} \tag{6-1}$$

$$R_{thermal} = \frac{\Delta T}{Q} = \frac{L}{kA} \tag{6-2}$$

The total thermal resistance of a composite material will depend on the configuration of constituent materials. In the unidirectional samples, when the heat flows in the axial direction of the rasters, the thermal circuit can be represented as three parallel resistance of polymer, air and wires as shown in Fig. 6-4 (a). In such case, more heat will tend to pass through the smallest resistance (i.e. material with higher thermal conductivity) and minimal amount will pass through the air voids (i.e. lowest thermal conductivity). Nevertheless, if the heat flows perpendicular to the raster, this will result in a group of resistances in series as shown in Fig. 6-4 (b). Here, the heat flow in each pass will be dominated by the smallest thermal resistance. In other words, the effective thermal conductivity of the pattern in this case will be dominated by the matrix conductivity.

The bi-directional samples will have the combined effect of the parallel and series heat flow in the unidirectional samples. Since half of the rasters are in parallel with the heat flow direction and the rest are perpendicular, the thermal circuit of the pattern can be represented as in Fig. 6-4 (c).

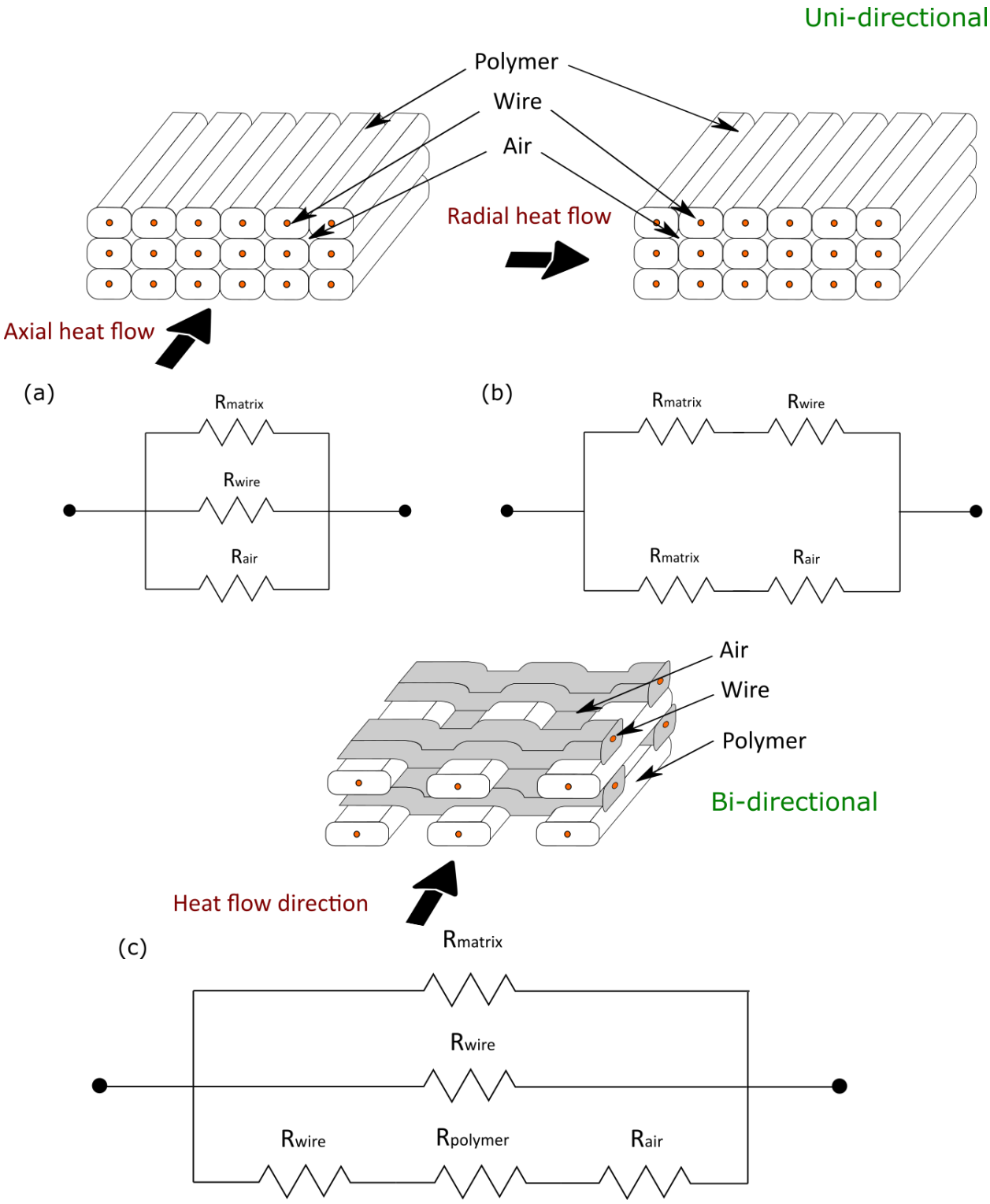

Figure 6-3 Schematic diagram for thermal circuit of unidirectional samples (a) axial heat flow, (b) transverse heat flow and (c) bidirectional samples

The equivalent resistance of the configurations shown in Fig. 6-4 can be evaluated using parallel and series resistances equations. Since air has a much lower thermal conductivity and volume fraction than that of the polymer or wire, its existence can be neglected when it is in parallel with a more conductive material as in Fig. 6-4 (a). As a result, the total resistance of the unidirectional samples when the heat is supplied parallel to the wire can be simplified to:

$$\frac{1}{R_{parallel}} = \frac{k_{eff}A}{L} = \frac{k_w A_w}{L} + \frac{k_m A_m}{L} \qquad (6\text{-}3)$$

This equation can be rearranged to obtain the effective thermal conductivity as a function of matrix and wire thermal conductivities and volume fractions.

$$k_{eff} = \left(1 - v_f\right)k_m + v_f k_f \qquad \text{Unidirectional Model (6-4)}$$

For the bi-directional configuration shown in Fig. 6-4 (c), the existence of the air with high volume fraction in series with the polymer and the wires will result in a much higher resistance and minimal heat pass through the perpendicular rasters. As a result, the contribution of the perpendicular rasters can be neglected, and the effective thermal conductivity of the composite can be represented as a function of the wire and polymer volume fraction parallel to the heat flow (v_{fp}):

$$k_{eff} = \left(1 - v_{fp}\right)k_m + v_{fp} k_f \qquad \text{Bi-directional Model (6-5)}$$

To perform accurate prediction of the effective thermal conductivity, the constituents' properties should be accurately measured. For the matrix material, Elkholy *et al.* [81] measured the thermal conductivity of PLA and PLA filled with copper particles using the

same facility and demonstrated that printing parameters such as raster width and height can influence the thermal conductivity. Thus, the matrix materials used in this study were measured independently to ensure that the printed samples have similar printing parameters to those of the CWPCs. The thermal conductivity of the copper wire was assumed to be 398 W/mK according to [61]. The wire and matrix volume fractions were evaluated based on the actual filler content obtained from optical analysis.

6.4. Thermal Conductivity Measurements

The effective thermal conductivity of the samples was characterized using an apparatus developed in [81] which based upon a modified guarded hot plate technique similar to ASTM C177 [82]. A schematic of this apparatus is shown in Fig. 6-3. The apparatus consists of one primary heater block guarded with a secondary heater block and one primary cooler block guarded with a secondary cooler. Thermal power from electrical heaters embedded in the primary heater block is conducted through the sample to the primary cold block. The secondary blocks isolate the primary ones from the clamping mechanism making sure that no heat is transferred from or to it. The steady-state temperature difference across the sample is measured using resistance temperature detectors (RTDs) inserted into each block and the measured thermal resistance of the sample, R_{meas}, is given by;

$$R_{meas} = \frac{(T_{hot} - T_{cold})}{Q} \tag{6-6}$$

The measured thermal resistance consists of the sum of the bulk sample resistance and the any thermal contact resistance between the sample and the apparatus given by

$$R_{meas} = R_{c,1} + R_{c,2} + R_{sample} = R_c + R_{sample} \quad (6\text{-}7)$$

$$= R_c + \frac{L}{k_{sample}A} \quad (6\text{-}8)$$

In this case, the thermal conductivity of the sample can be calculated by rearranging as;

$$k_{sample} = \frac{L}{A\left[\frac{(T_{hot} - T_{cold})}{Q} - R_c\right]} \quad 6\text{-}9)$$

The contact resistance can be obtained by measuring the total thermal resistance for several thicknesses of a given sample which have similar surface properties and extrapolating the measured resistance to zero thickness.

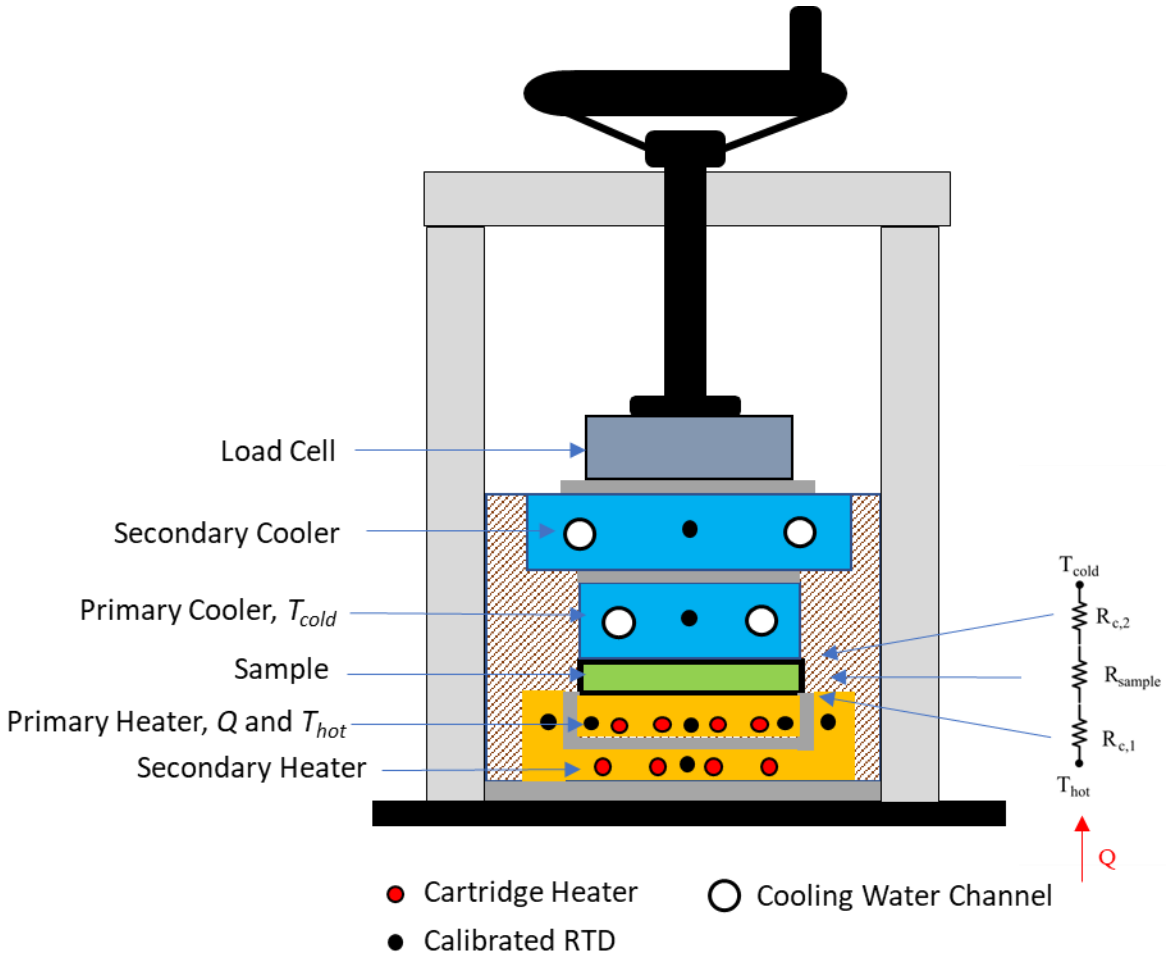

Figure 6-4 Thermal conductivity measuring apparatus showing main components

The primary and secondary (guard) blocks were machined from copper with the primary blocks having a contact area of 40 mm x 40 mm. Cartridge heaters energized by independently controlled DC power supplies (Aim TTi, CPX400D) were used to control the temperature of the primary and secondary heater blocks. To ensure that no heat is transferred to the clamping mechanism, the secondary heater temperature was set to be identical with the primary heater temperature. This was achieved by adjusting the secondary heater input power until the temperature matches. Similarly, the temperature of the secondary cooler was set to be the same as the primary one. Here, a U-channel was

machined into the primary and secondary coolers where a temperature-controlled water from a (Julabo F32-HE) water chiller flows.

The temperature of all blocks is measured using 1 mm x 15 mm RTDs (Omega, 1PT100KN1510) inserted into holes at the locations shown in Fig. 6-3 which were calibrated to within 0.01 K of each other.

The temperature measurements were logged using an Agilent 34970A data acquisition system while the input power to the primary heaters were quantified by measuring the voltage and current using two independent Agilent 34401A digital multimeters. A MATLAB script was customized to record all the measured values and to calculate the time gradient of the measured values. The system was considered in a steady state when the time gradient of the temperatures reaches 1e-5 K/s.

The input power to the secondary heater was controlled by MATLAB to ensure that the temperature difference between the primary and the secondary block does not exceed 0.01 K. This was achieved by varying the power to the secondary heater until its temperature was identical to the primary heater eliminating the thermal gradient and therefore heat loss from the primary heater.

The sample under test is clamped between the primary and secondary heating and cooling blocks using clamping screw, device frame and the load cell (KAF-S, AST, Dresden, Germany), as shown in Fig. 6-3. Samples were clamped with a pressure of approximately 3 MPa and a few droplets of mineral oil was used to minimize thermal contract resistance and to minimize constriction resistance. The entire assembly was encased with silica aerogel insulation which has a thermal conductivity of 0.014 W/mK. Additional details

regarding the data acquisition, temperature control, calibration and uncertainty analysis are provided in [81].

6.5. Results and discussion

6.4.1. Microstructure analysis

The microscopic cross-sectional images of the wire reinforced samples described in Table 6-3 (i.e. samples 3,4,5, and 6) are shown in Fig. 6-5 & 6 in which matrix, wires and air voids can be seen. For the lines pattern with the 1mm nozzle, the PLA matrix in Fig. 6-5 (a) had a better raster adhesion compared with the PLA with copper particles in Fig. 6-5 (b). Although the two samples were printed with the same printing parameters, bigger air voids and individual raster can be more clearly seen in the PLA with copper particles matrix. This may be caused by a difference in the amount extruded material generated by slight difference in the filament's diameter

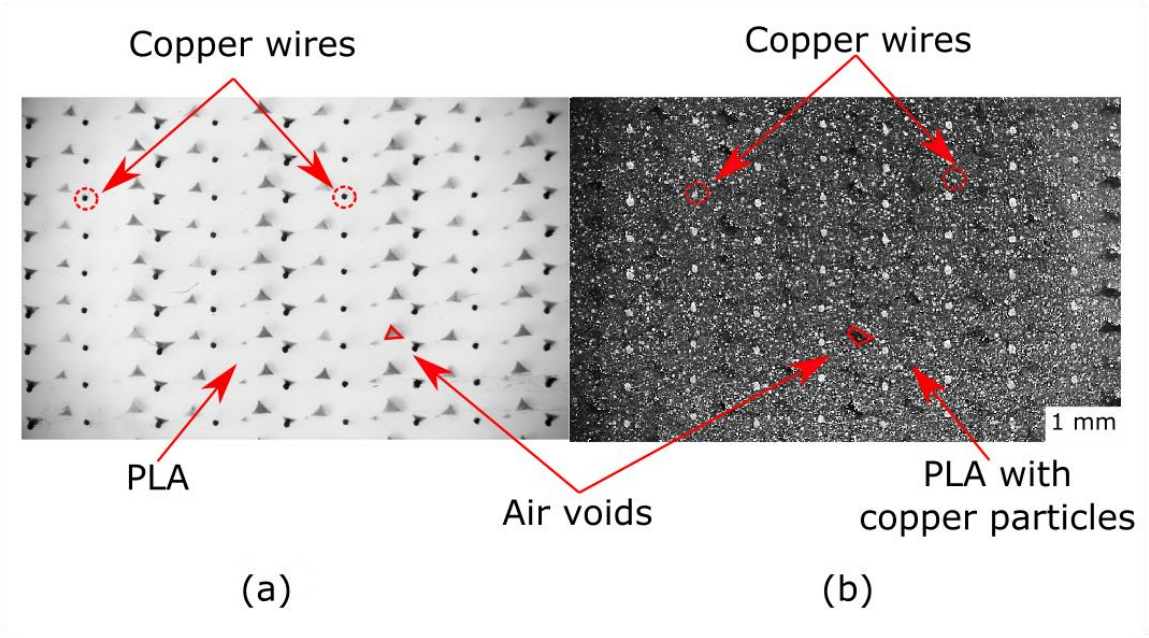

Figure 6-5 Cross-sectional view of (a) unidirectional PLA with wires (1 mm nozzle) and (b) unidirectional PLA + copper particles with wires (1 mm nozzle)

In the bidirectional sample shown in Fig. 6-6 (a), the axial, transversal wires as well as the air gabs between the axial rasters can be seen in the figure. Although the rasters have similar width to the one in the lines pattern, the grid pattern nozzle movement presses the previously printed rasters causing an increase in their thickness and a decrease in their height. The line pattern with the 0.6 mm nozzle shown in Fig. 7 (b) showed good adhesion between the rasters with the air voids closer to the wires compared to the 1mm nozzle.

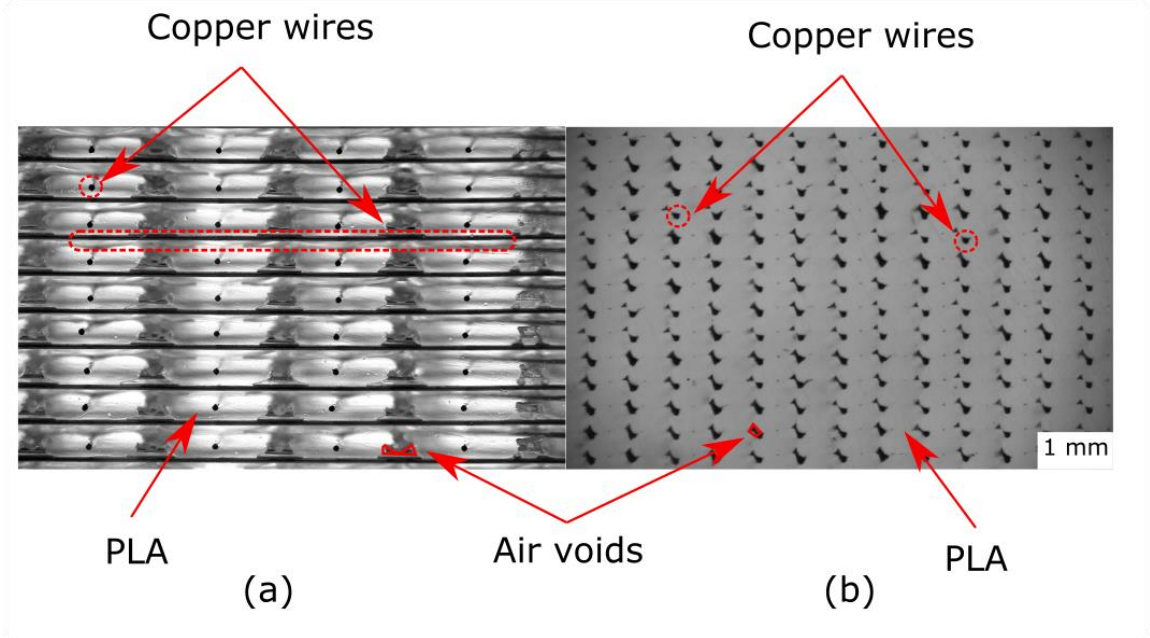

Figure 6-6 Cross-sectional view of (a) bi-directional PLA with wires (1 mm nozzle) and (b) unidirectional PLA with wires (0.6 mm nozzle)

Optical analysis of the images showed that the used metal wire has a diameter of approximately 100 um which will increase the percentage of the filler within the matrix.

Based on the area ratio, an actual continuous filler content was obtained. Table 6-4 summarizes the actual filler content for the different samples. The wire volume fraction of the bi-directional sample was calculated based on the area of the wires perpendicular to the cross-section which represents the wires parallel to the heat transfer direction. These actual filler content will increase the effective thermal conductivity prediction obtained from the analytical model.

Table 6-4 Wires' volume fraction based on image processing

Sample No.	Wires volume fraction (v_{fp}) %
3	1.07
4	0.538
5	1.07
6	2.7

6.4.2. Effective Thermal Conductivity

Thermal conductivity measurements were performed using the setup describe in Section 6.4. After polishing, each sample was tested before going through another set of grinding and polishing stages to reduce its thickness. Three or four thickness were tested for each sample and the temperature drop across each thickness was recorded.

The PLA and the copper filled PLA samples were tested first to evaluate their thermal conductivity and to use it as an input to the analytical model in order to predict the effective thermal conductivity of the wire reinforced samples. For the PLA sample as an example, the input power to the heaters was typically 0.5 W which resulted in a temperature differences across the sample of 6.2, 4.7 and 3.03 °C at 4.09, 3.07- and 2.02-

mm thickness respectively. Afterwards, the total thermal resistance of each thickness was evaluated using (6-2) and plotted against the sample thickness as shown in Fig. 6-7. Here, the uncertainty associated with the resistance calculation was at maximum 0.09 K/W. Thereafter, the trend line for the measured points was obtained using linear fitting. The copper filled PLA sample's results were processed similarly where Fig. 6-8 shows the relation between the measured resistance and the specimen thickness.

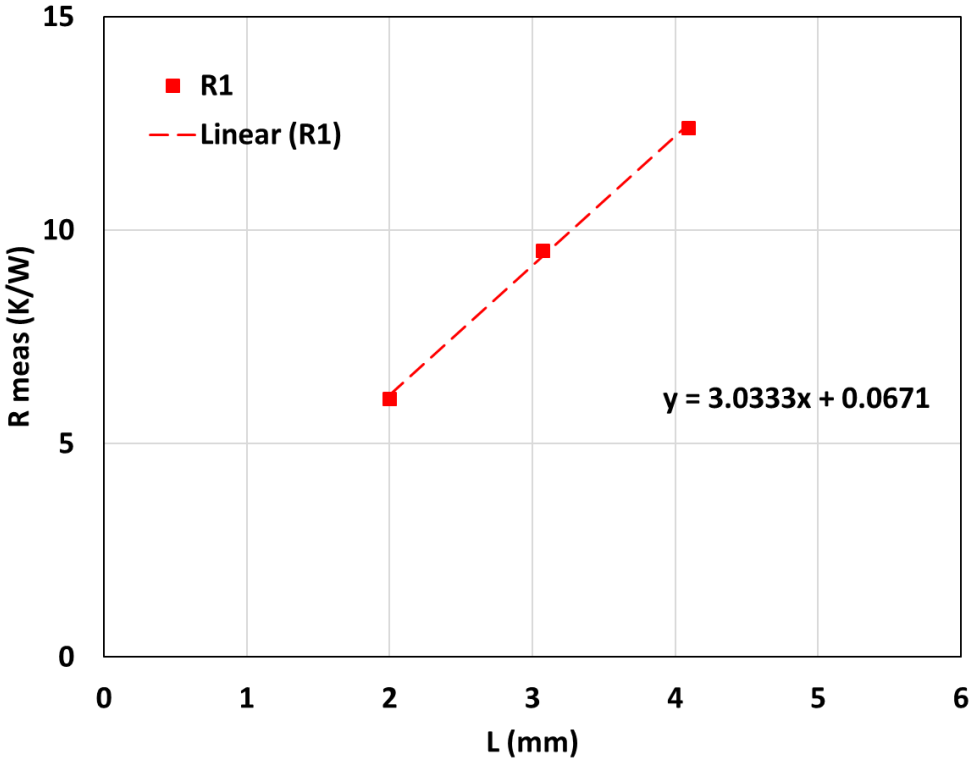

Figure 6-7 Measured resistance against samples thickness for PLA sample (Sample 1)

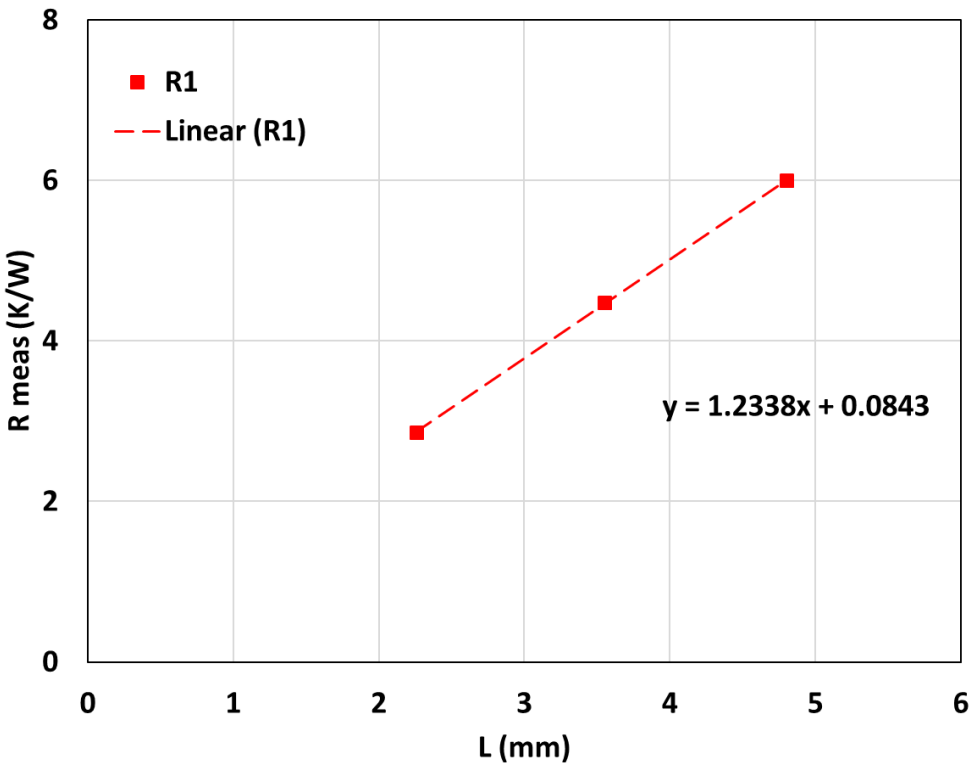

Figure 6-8 Measured resistance against samples thickness for PLA sample with copper particles (Sample 2)

The trend line follows the equation described in (6-8) where the intersection with the y axis represents the contact resistance while the slope of the curve is a function of the sample thermal conductivity and area. For PLA and copper filled PLA, the contact resistance was found to be less than 3% of the total measured resistance at the smallest thickness and as a result it can be neglected. This was also observed by Elkholy in [81] for materials with low thermal conductivity.

The copper filled PLA in Sample 2 showed improvement with a 0.5 W/mK compared to 0.22 W/m.K for the pure PLA. Although the composite matrix is filled with 80% of copper particles, the effective thermal conductivity was still dominated by the polymer phase.

Another drawback of the copper filled PLA is the high density (3.5 g/cm^3) which is greater than some conductive metals such as aluminum (2.705 g/cm^3). This means that the copper filled PLA also losses the advantage of being a light-weight material.

The same procedure was followed for the thermal conductivity evaluation of the wire reinforced samples. Figures 6-9 to 6-12 show relation between the measured thermal resistance and the specimen thickness for each replicate of the printed samples. Here, the effect of the contact resistance was more significant resulting in a bigger difference in the temperature drop across different thicknesses of the samples. The uncertainty within contact resistance value can greatly affect the calculated effective thermal conductivity as described in (6-8). For this reason, three or four thicknesses of multiple replicates (R1, R2, and R3) were tested to evaluate repeatability. The effective thermal conductivity of each sample was separately evaluated based on (6-9) and then the average value for the three replicates was calculated.

Generally, the results points showed good linearity with an R^2 greater than 0.98 for all of the samples. The equations shown on the figures represent the trend line equation where the constant represents the contact resistance value.

For the unidirectional PLA+wire samples (Sample 3), the contact resistance values of the three replicates were near 0.5 which represents around 40% of the total resistance of the thinnest sample. Figure 6-9 shows the relation between the total resistance and the specimen thickness for the three replicates of Sample 3.

For the bi-directional samples (Sample 4), higher contact resistance values were obtained.

The contact resistance values shown in Fig. 6-10 represents 68% of the total measured resistance for the least thickness sample. The greater influence of the contact resistance was anticipated to be caused by the nature of the grid pattern which creates more air voids within the sample (Fig. 6-6 (a)). Increased air voids in contact with the heater and cooler blocks of the apparatus results in higher the contact resistance.

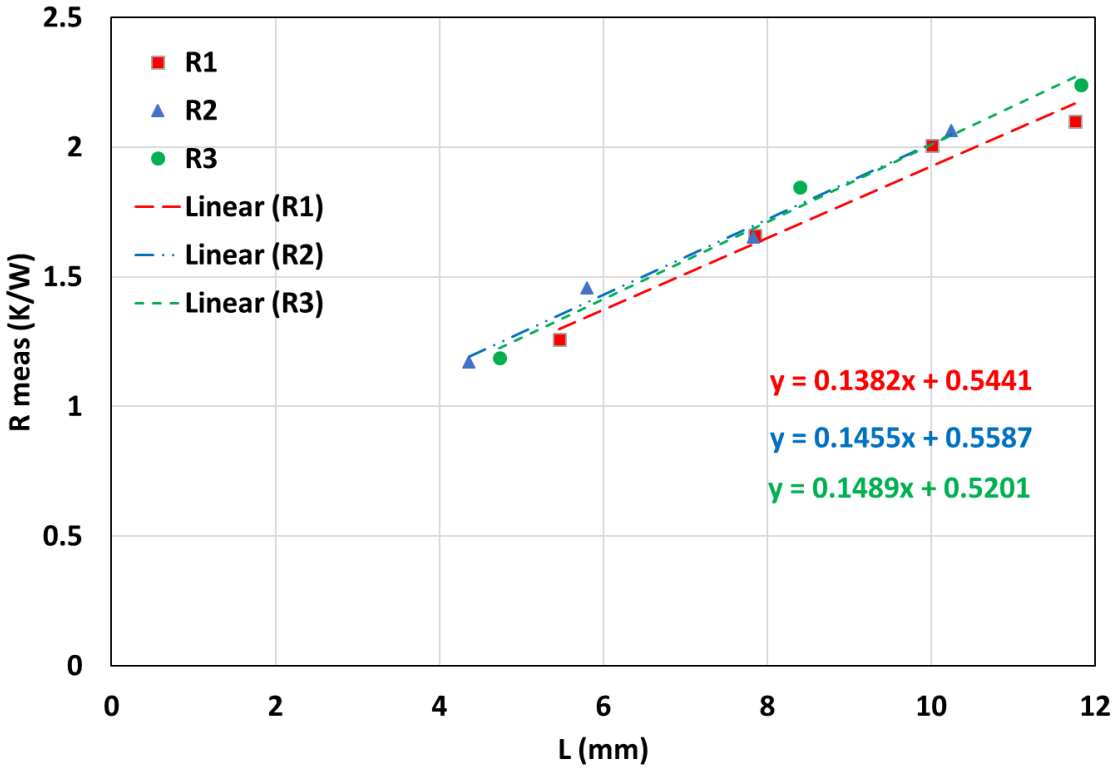

Figure 6-9 Measured resistance against samples thickness for three replicates (R1, R2 and R3) of Sample 3 (Unidirectional PLA+wire)

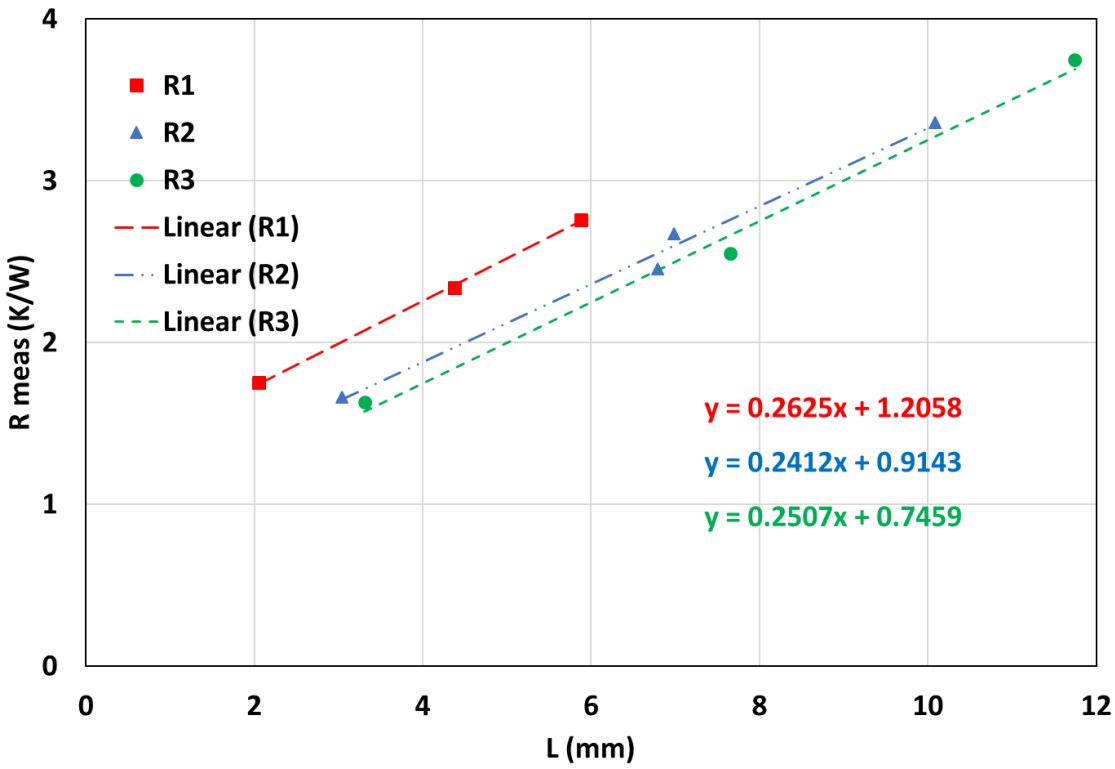

Figure 6-10 Measured resistance against samples thickness for three replicates (R1, R2 and R3) of Sample 4 (Bi-directional PLA+wire)

The unidirectional PLA+copper+wire samples (Sample 5) have a similar configuration to the PLA+wire (Sample 3) and the same wire volume fraction. Although the values of the contact resistance for copper filled matrix with wires were lower compares to the PLA+wire, the bulk resistance values were also lower causing more significant effect of the contact resistance on the total measured resistance as shown in Fig. 6-11. The difference in the contact resistance values is conjectured to be caused by irregularities in the grinding and polishing processes. However, the linearity of the trend lines shows that these irregularities are minimal for the same replicate.

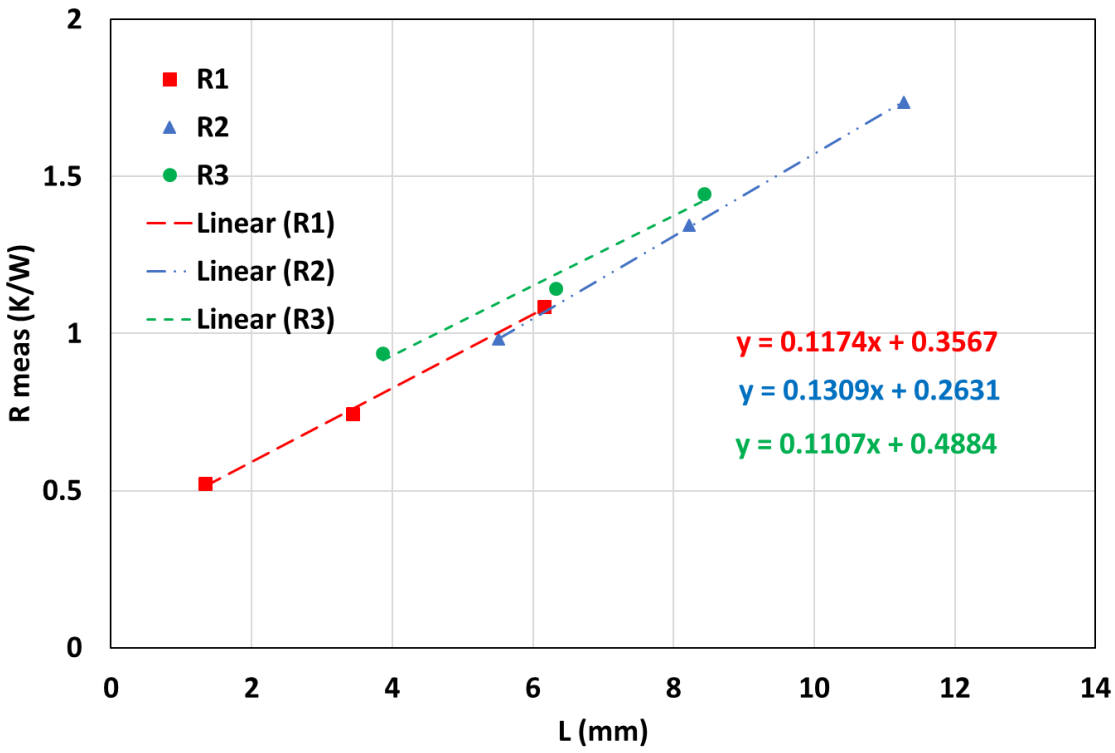

Figure 6-11 Measured resistance against samples thickness for three replicates (R1, R2 and R3) of Sample 5 (Unidirectional PLA+copper+wire)

The total resistance for the PLA+wire samples (Sample 6), which have the highest wire volume content, was measured and plotted against the thickness as shown in Fig. 6-12. Since these replicates were expected to have the highest thermal conductivities (and therefore lowest bulk resistance), the contact resistance was found to have the most significant effect on the total measured resistance with 85% for the least sample thickness.

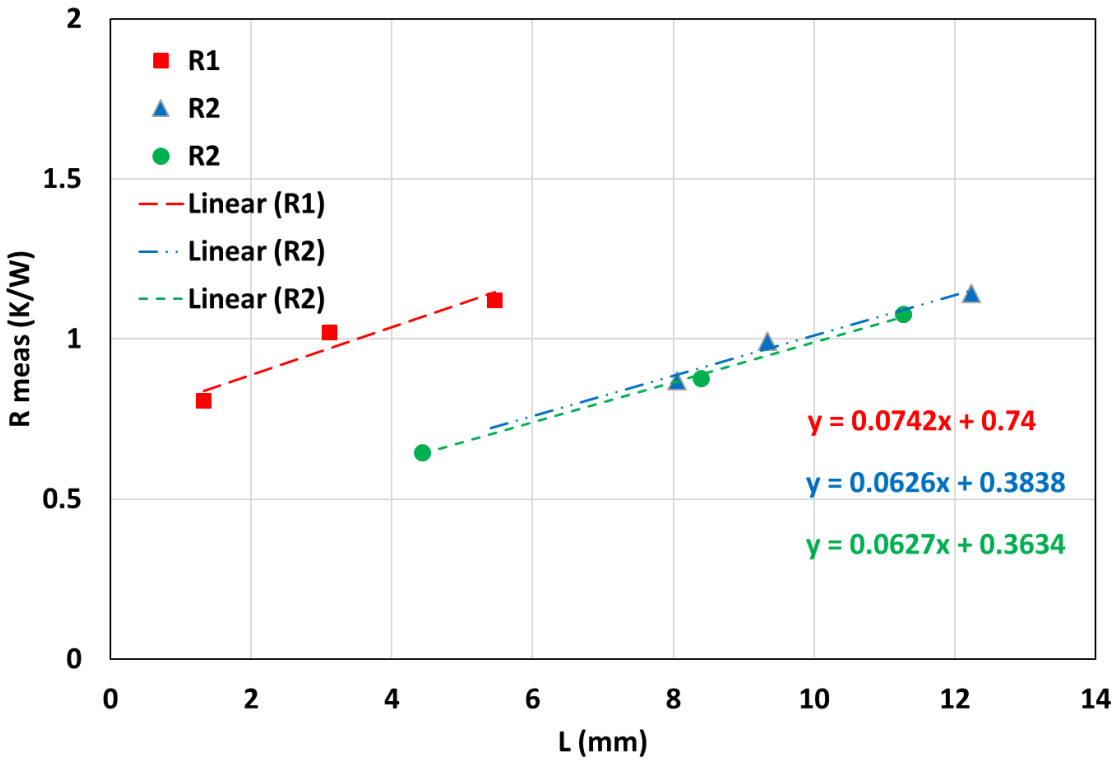

Figure 6-12 Measured resistance against samples thickness for three replicates (R1, R2 and R3) of Sample 6 (Unidirectional PLA+wire)

The uncertainty of the effective contact resistance was calculated based on twice the standard deviation of the three replicates values. Figure 6-13 summarizes the specific contact resistance (RA) values for the matrix and the wire reinforced samples. Here Samples 1 and 2 (PLA and PLA+Copper) which do not contain copper wires exhibit the lowest contact resistance. Meanwhile, the CWPC samples (Samples 3-6) exhibit significantly contact resistance suggesting this increase be due to the presence of the copper wires at the interface. It can be deduced from the figure that the contact area of the solid phase, which corresponds to fill ratio, greatly affect the contact resistance. This can be seen in the bi-directional sample (Sample 4) which has the lowest solid contact with the

measurement test rig and the highest value of contact resistance. This sample also exhibited high uncertainty because the ratio of copper wires to polymer at the cross-sections could have varied greatly because of nature of the bi-directional wires. The unidirectional CWPC samples (Samples 3, 5, 6) have more consistent cross-sections and therefore similar contact resistance values.

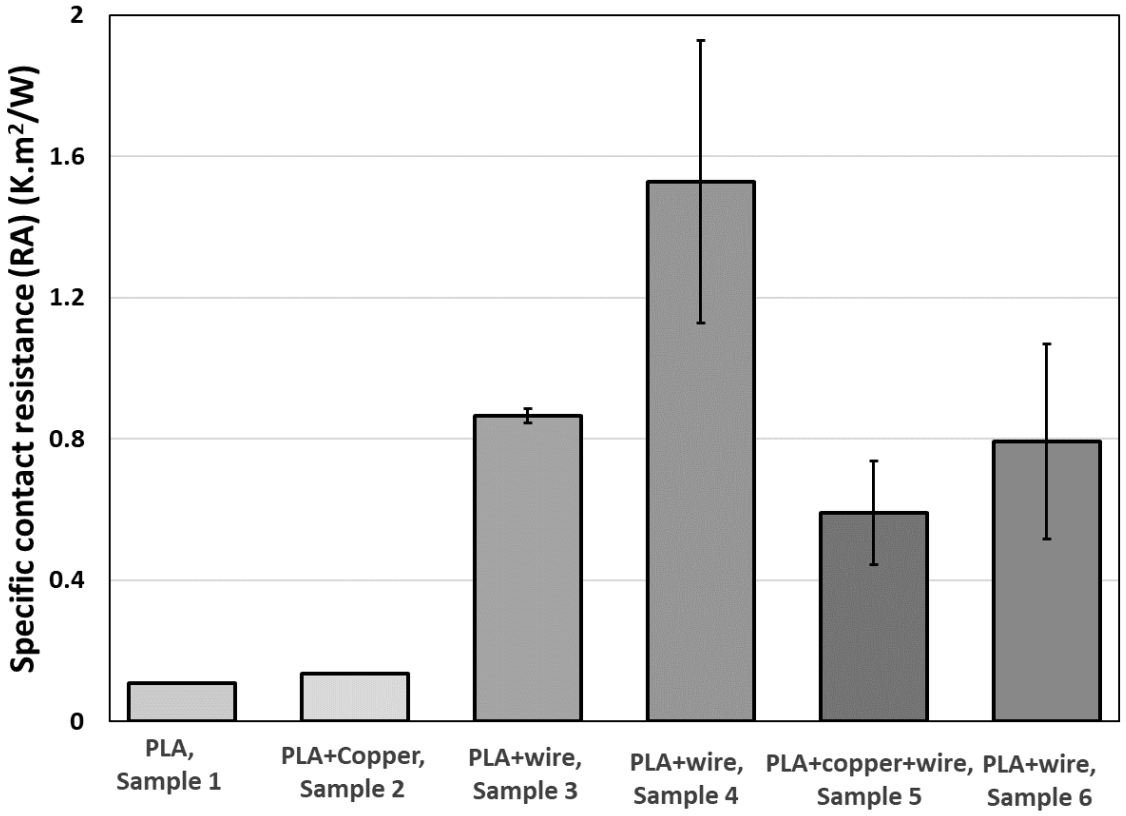

Figure 6-13 Specific contact resistance (RA) of matrix and wire reinforced samples

Figure 6-14 shows the effective thermal conductivity of the pure and wire reinforced samples. The Unidirectional configuration in Sample 3 boosted the effective thermal conductivity of the composite to 4.47 W/mK which represents 21 times greater thermal

conductivity with only 1.07% of continuous filler. This shows a very good consistency with the model prediction (4.44 W/mK). The Bi-directional configuration in Sample 4 showed an effective thermal conductivity of almost half of the line pattern (Uni-directional) in Sample 3 as was predicted by the model. The samples printed with the PLA matrix have a similar density to the pure PLA since the wire content is very small (1.07%). This means that, compared to the copper filled PLA, the continuous wire significantly improves the effective thermal conductivity without losing the light weight advantage.

The copper filled matrix with the wires in Sample 5 exhibited a slightly higher effective thermal conductivity compared to Sample 3 with an average of 5.2 W/mK which is higher than the model prediction. Here, the improved thermal conductivity is mainly caused by the more conductive matrix utilized in these sample

By increasing the wire volume content to 2.7% (Sample 6), the effective thermal conductivity of the unidirectional CWPC increased to 9.4 W/mK which represents almost 50 times the pure polymer conductivity. The high uncertainty associate with Sample 6 is caused by difference in contact resistance across the replicates which may have occurred due to difficulty reproducing identical contact surfaces during the grinding and polishing stages. Testing more replicates and ensuring similar surface finishing would help reducing this uncertainty.

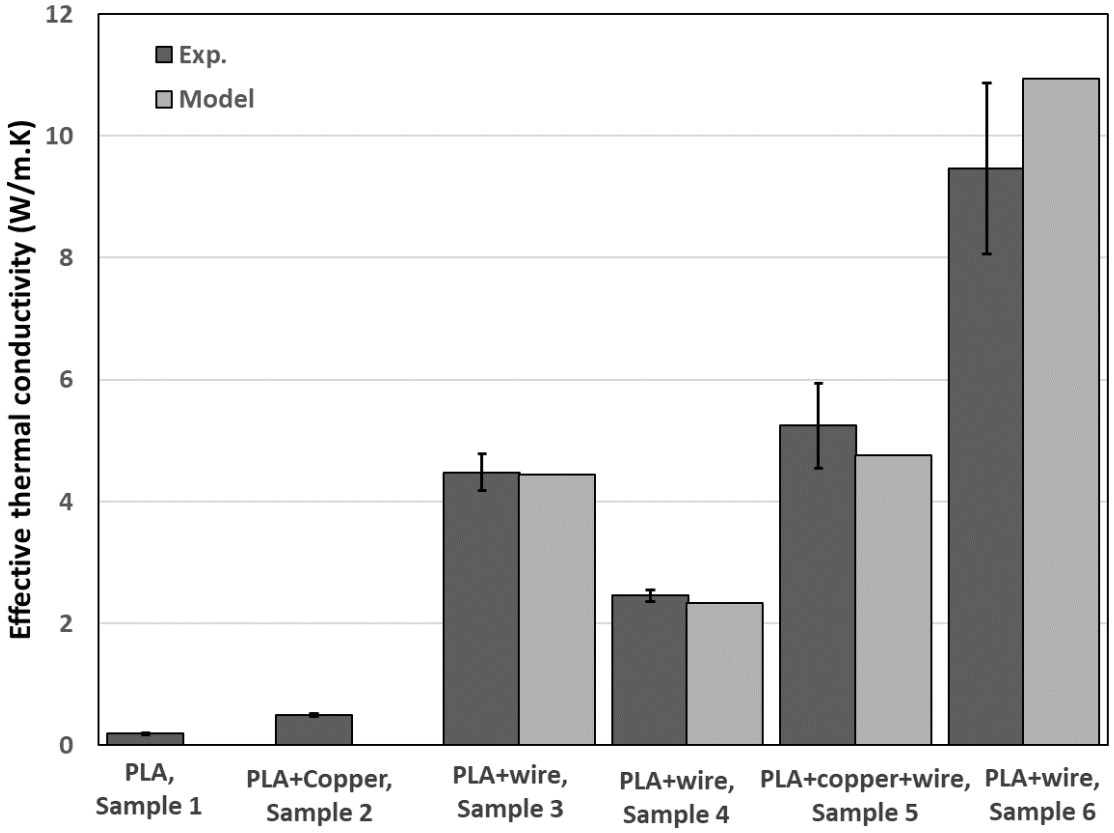

Figure 6-14 Effective thermal conductivity of matrix and wire reinforced samples

6.6. Summary & Outlook

Copper wire reinforced samples were printed to investigate the effective thermal conductivity improvement of several 3D printed CWPCs. The effective thermal conductivity of the printed composites was measured experimentally and predicted analytically using simple rule of mixture model. Firstly, the thermal conductivity of 80% copper particles filled PLA was measured and was found to be almost 2.5 times that of pure PLA. By introducing continuous copper wire into the composite, the thermal conductivity increased significantly to 23 times the thermal conductivity of the base polymer at 1.07% volume

content. In addition, replacing the PLA matrix with copper filled PLA (i.e. more conductive matrix) increased the thermal conductivity of the composite to 27 times the pure polymer. The printing pattern was found to have a significant effect on the effective thermal conductivity where the highest thermal conductivity is obtained when the wires are aligned in the heat transfer direction. Printing with a grid pattern reduced the thermal conductivity to almost a half which agrees with the model prediction.

This initial result demonstrates the potential use of 3D printed CWPCs as a component in polymer-based heat exchanger applications historically thermal conductivity of the solid phase can be a limiting performance factor. Further improvement to the printing processes can be incorporated to allow for higher volume fraction of wires. This includes implementing a wire feeding mechanism to over come the need for large a mount of polymer to pull the wires out of the nozzle.

Another option is to employ high-conductivity continuous fibers such as pitch-based carbon fibres (k=800 W/mK [80]) and carbon nanotubes to further increase the effective thermal conductivity. The foregoing results had validated the simple parallel thermal resistance network model to predict effective thermal conductivity of the CWPCs in the direction of the fibers. This model can be extended to predict effective thermal conductivity for other fibers and fill ratios. Figure 6-15 shows the anticipated thermal conductivity values with respect to the filler volume fraction using the parallel model. Here, a thermal conductivity of 167 W/m.K (similar to aluminum alloy 6061 which commonly used for heat sink applications), can be achieved with CWPCs having only 20% pitch-based carbon fibres. This helps indicate that the fabrication of complex shaped 3D printed

composite heat exchangers with good thermal performance is achievable.

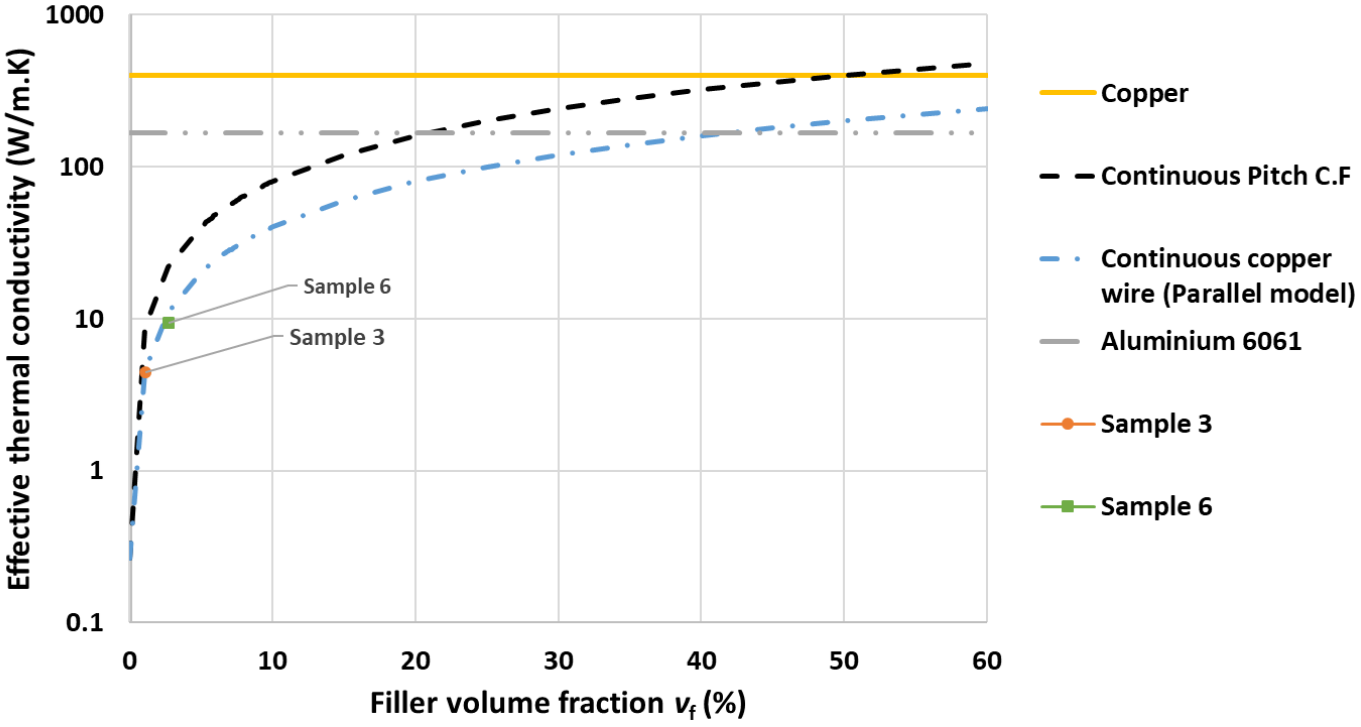

Figure 6-15 Predicted effective thermal conductivities using continuous fibres additives in the parallel direction

Chapter 7 Summary, Conclusions and Future Outlook

Polymer composites have been used for decades in various applications since they commonly offer enhanced properties compared with pure polymers. With additive manufacturing techniques such as 3D printing, polymer composites have been used to fabricate not only prototypes, but also more functional products. Discontinuous fillers such as chopped fibres and metal particles have been shown to improve both mechanical and thermal properties of the fabricated components. Yet, this improvement is limited by the interfacial properties of the composite. To address this shortcoming, continuous fillers such as carbon fibers were utilized.

The objectives of this study were to develop a feasible 3D printing technique which utilizes continuous metal wire as a reinforcement for polymer composites and to analytically and experimentally characterise the mechanical and thermal properties of these 3D printed CWPCs. A further objective was, to investigate the potential use of 3D printed CWPCs as configurable low-temperature heaters.

7.1. General Conclusions

A process and technique were developed whereby continuous wire polymer composite components could be fabricated using a modified, open-source printer which coextrudes wire and polymer. The process was designed to facilitate the variation of wire materials and volume fractions.

Mechanical testing of CWPCs demonstrated superior performance in comparison with the base polymer. A 0.7% volume fraction of nickel chromium wires resulted an improvement of up to 50% in tensile and flexural moduli were obtained. Overall the results were in good

agreement with some deviation with the analytical rule of mixture solid mechanics models. The model does not consider the effect interfacial ponding between the polymer and wire which can be incorporated in future work.

From a thermal standpoint, in the direction of wires, CWPCs demonstrated an increase in effective thermal conductivity of 4.2 W/mK which is corresponds to a 21-fold increase over the base polymer with a 1.07% volume fraction of continuous copper wires. One-dimensional series and parallel models for thermal resistance and effective thermal conductivity were adapted for the several configurations of 3D printed CPWC samples and provide good agreement with the experimental results.

The technique developed herein was also used to 3D print a CWPC heating element which were then used to fabricate a low-temperature heater panel. These 3D printed heated panels were field-tested on board a navy ship sailing in the arctic circle. The panel was able to maintain its surface ice free at different water loading conditions. In addition, with combining with hydrophobic coating, the consumed energy of the panels was reduced significantly.

7.2. Future Outlook

The following points lay the foundations for future work on 3D printed CWPC. These include:

1- Investigate the effect of the wire thermal conductivity and thermal expansion on the wire-polymer adhesion.

2- Perform wire pull-out test to quantify the adhesion between the wires and the matrix.

3- Further adaptation of the 3D printing technique to facilitate printing with higher filler content by coating metal wires prior to printing.

4- Utilization of cutting mechanism to allow for more control over the reinforcement direction.

5- Utilization of Ultra-high conductive fillers such a pitch-based carbon fibres and carbon nanotube yarns to further improve the thermal conductivity.

6- Use of this 3D printing technique for other active or passive electrical elements such as a range of 3D printed CWPC sensors

References

[1] C. González, J. J. Vilatela, J. M. Molina-Aldareguía, C. S. Lopes, and J. LLorca, "Structural composites for multifunctional applications: Current challenges and future trends," *Prog. Mater. Sci.*, vol. 89, pp. 194–251, 2017.

[2] A. K. Pathak, M. Borah, A. Gupta, T. Yokozeki, and S. R. Dhakate, "Improved mechanical properties of carbon fiber/graphene oxide-epoxy hybrid composites," *Compos. Sci. Technol.*, vol. 135, pp. 28–38, 2016.

[3] A.P. Sobha P.S. Srekala. Sunil.K. Narayanankutty, "Electrical, thermal, mechanical and electromagnetic interference shielding properties of PANI/FMWCNT/TPU composites," *Prog. Org. Coatings*, vol. 113, no. September, pp. 168–174, 2017.

[4] R. Atif, I. Shyha, and F. Inam, "Mechanical, thermal, and electrical properties of graphene-epoxy nanocomposites-A review," *Polymers (Basel).*, vol. 8, no. 8, 2016.

[5] A. C. De Leon, Q. Chen, N. B. Palaganas, J. O. Palaganas, J. Manapat, and R. C. Advincula, "High performance polymer nanocomposites for additive manufacturing applications," *React. Funct. Polym.*, vol. 103, pp. 141–155, 2016.

[6] U. Kalsoom, P. N. Nesterenko, and B. Paull, "Recent developments in 3D printable composite materials," *RSC Adv.*, vol. 6, no. 65, pp. 60355–60371, 2016.

[7] H. Chen *et al.*, "Thermal conductivity of polymer-based composites: Fundamentals and applications," *Prog. Polym. Sci.*, vol. 59, pp. 41–85, 2016.

[8] M. Nikzad, S. H. Masood, and I. Sbarski, "Thermo-mechanical properties of a highly filled polymeric composites for Fused Deposition Modeling," *Mater. Des.*, vol. 32, no.

6, pp. 3448–3456, 2011.

[9] S. Hwang, E. I. Reyes, K. sik Moon, R. C. Rumpf, and N. S. Kim, “Thermo-mechanical Characterization of Metal/Polymer Composite Filaments and Printing Parameter Study for Fused Deposition Modeling in the 3D Printing Process,” *J. Electron. Mater.*, 2015.

[10] W. Zhong, F. Li, Z. Zhang, L. Song, and Z. Li, “Short fiber reinforced composites for fused deposition modeling,” *Mater. Sci. Eng. A301*, vol. 301, pp. 125–130, 2001.

[11] F. Ning, W. Cong, J. Qiu, J. Wei, and S. Wang, “Additive manufacturing of carbon fiber reinforced thermoplastic composites using fused deposition modeling,” *Compos. Part B Eng.*, 2015.

[12] S. Dul, L. Fambri, and A. Pegoretti, “Fused deposition modelling with ABS-graphene nanocomposites,” *Compos. Part A Appl. Sci. Manuf.*, 2016.

[13] U. Kalsoom, A. Peristyy, P. N. Nesterenko, and B. Paull, “A 3D printable diamond polymer composite: a novel material for fabrication of low cost thermally conducting devices,” *RSC Adv.*, vol. 6, no. 44, pp. 38140–38147, 2016.

[14] C. Shemelya *et al.*, “Anisotropy of thermal conductivity in 3D printed polymer matrix composites for space based cube satellites,” *Addit. Manuf.*, vol. 16, pp. 186–196, 2017.

[15] Z. Quan *et al.*, “Printing direction dependence of mechanical behavior of additively manufactured 3D preforms and composites,” *Compos. Struct.*, vol. 184, no. July 2017, pp. 917–923, 2018.

[16] Y. Ibrahim, Garrett W. Melenka and Roger Kempers, “Additive Manufacturing of Continuous Wire Polymer Composites,” *Manuf. Lett.*, vol. 16, no. April, pp. 49–51, 2018.

[17] Y. Ibrahim, Garrett W. Melenka, Roger Kempers, “Fabrication and Tensile Testing of 3D Printed Continuous Wire Polymer Composites,” *Rapid Prototyp. J.*, 2018.

[18] Y. Ibrahim, Garrett W. Melenka and Roger Kempers, “Flexural Properties of Continuous Wire Polymer Composites,” *Compos. Struct.*, 2019.

[19] Y. Ibrahim, R. Kempers, and A. Amirfazli, “3D printed electro-thermal anti-icing system for composite panels,” *Cold Reg. Sci. Technol.*, 2019.

[20] X. Wang, M. Jiang, Z. Zhou, J. Gou, and D. Hui, “3D printing of polymer matrix composites: A review and prospective,” *Compos. Part B Eng.*, vol. 110, pp. 442–458, 2017.

[21] P. Dudek, “FDM 3D printing technology in manufacturing composite elements,” *Arch. Metall. Mater.*, vol. 58, no. 4, pp. 1415–1418, 2013.

[22] S. H. Masood and W. Q. Song, “Development of new metal/polymer materials for rapid tooling using Fused deposition modelling,” *Mater. Des.*, 2004.

[23] S. H. Masood and W. Q. Song, “Assembly Automation Thermal characteristics of a new metal/polymer material for FDM rapid prototyping process Thermal characteristics of a new metal/polymer material for FDM rapid prototyping process,” *Assem. Autom. Rapid Prototyp. J. Iss Rapid Prototyp. J.*, vol. 25, no. 11, pp. 309–315, 2002.

[24] F. Ning, W. Cong, Y. Hu, and H. Wang, “Additive manufacturing of carbon fiber-reinforced plastic composites using fused deposition modeling: Effects of process parameters on tensile properties,” *J. Compos. Mater.*, vol. 51, no. 4, pp. 451–462, 2017.

[25] M. Ivey, G. W. Melenka, J. P. Carey, and C. Ayranci, “Characterizing short-fiber-reinforced composites produced using additive manufacturing,” *Adv. Manuf. Polym. Compos. Sci.*, vol. 3, no. 3, pp. 81–91, 2017.

[26] R. T. L. Ferreira, I. C. Amatte, T. A. Dutra, and D. Bürger, “Experimental characterization and micrography of 3D printed PLA and PLA reinforced with short carbon fibers,” *Compos. Part B Eng.*, vol. 124, pp. 88–100, 2017.

[27] Y. H. Esterlin, M. del C. V. Vázquez, R. E. G. Junco, and C. M. C. Torres, “Diabetes mellitus y depresión psicológica en el adulto mayor,” *Rev. del Hosp. Psiquiatr. la Habana*, vol. 9, no. 3, p. 3, 2012.

[28] H. Wang, H. Wang, W. Li, D. Ren, and Y. Yu, “An improved microbond test method for determination of the interfacial shear strength between carbon fibers and epoxy resin,” *Polym. Test.*, vol. 32, no. 8, pp. 1460–1465, 2013.

[29] B. Strength and U. Indentation, “Interfacial Bond Strength in Fiber Reinforced Composites,” pp. 9–10.

[30] J. Cruz and R. Fangueiro, “Surface Modification of Natural Fibers: A Review,” *Procedia Eng.*, vol. 155, pp. 285–288, 2016.

[31] K. Kim, Y. C. Jung, S. Y. Kim, B. J. Yang, and J. Kim, "Adhesion enhancement and damage protection for carbon fiber-reinforced polymer (CFRP) composites via silica particle coating," *Compos. Part A Appl. Sci. Manuf.*, vol. 109, no. October 2017, pp. 105–114, 2018.

[32] T. Ramanathan, A. Bismarck, E. Schulz, and K. Subramanian, "Investigation of the influence of acidic and basic surface groups on carbon fibres on the interfacial shear strength in an epoxy matrix by means of single-fibre pull-out test," *Compos. Sci. Technol.*, vol. 61, no. 4, pp. 599–605, 2001.

[33] A. Li, C. Zhang, and Y. F. Zhang, "Thermal conductivity of graphene-polymer composites: Mechanisms, properties, and applications," *Polymers (Basel).*, vol. 9, no. 9, pp. 1–17, 2017.

[34] A. Bagchi and S. Nomura, "On the effective thermal conductivity of carbon nanotube reinforced polymer composites," *Compos. Sci. Technol.*, 2006.

[35] K. J. Lee GW, Lee JI, Lee SS, Park M, "Comparisons of thermal properties between inorganic filler and acid-treated multiwall nanotube/polymer composites.," *J. Mater. Sci.*, 2005.

[36] G. W. Lee, M. Park, J. Kim, J. I. Lee, and H. G. Yoon, "Enhanced thermal conductivity of polymer composites filled with hybrid filler," *Compos. Part A Appl. Sci. Manuf.*, 2006.

[37] "Berman R. Thermal conduction in solids. Oxford: Clarendon press; 1976."

[38] B. C. Hongyu Chena, Valeriy V. Ginzburgb, Jian Yangc, Yunfeng Yanga, Wei Liua, Yan

Huanga, Libo Dua, “Thermal conductivity of polymer-based composites: Fundamentals and applications,” *Prog. Polym. Sci.*, vol. 59, pp. 41–85, 2015.

[39] R. Prasher, “Acoustic mismatch model for thermal contact resistance of van der Waals contacts,” *Appl. Phys. Lett.*, vol. 94, no. 4, pp. 1–4, 2009.

[40] K. Pietrak and T. S. Wiśniewski, “Methods for experimental determination of solid-solid interfacial thermal resistance with application to composite materials,” *J. Power Technol.*, vol. 94, no. 4, pp. 270–285, 2014.

[41] M. I. Daniel and O. Ishai, *Engineering Mechanics of Composite Materials*. 2006.

[42] P. Parandoush and D. Lin, “A review on additive manufacturing of polymer-fiber composites,” *Compos. Struct.*, vol. 182, pp. 36–53, 2017.

[43] L. G. Blok, M. L. Longana, H. Yu, and B. K. S. Woods, “An investigation into 3D printing of fibre reinforced thermoplastic composites,” *Addit. Manuf.*, vol. 22, no. March, pp. 176–186, 2018.

[44] B. Brenken, E. Barocio, A. Favaloro, V. Kunc, and R. B. Pipes, “Fused filament fabrication of fiber-reinforced polymers: A review,” *Addit. Manuf.*, vol. 21, no. January, pp. 1–16, 2018.

[45] H. Prüß and T. Vietor, “Design for Fiber-Reinforced Additive Manufacturing,” *J. Mech. Des.*, vol. 137, no. 11, p. 111409, 2015.

[46] N. Li, Y. Li, and S. Liu, “Rapid prototyping of continuous carbon fiber reinforced polylactic acid composites by 3D printing,” *J. Mater. Process. Technol.*, vol. 238, pp.

218–225, 2016.

[47] Q. Hu, Y. Duan, H. Zhang, D. Liu, B. Yan, and F. Peng, “Manufacturing and 3D printing of continuous carbon fiber prepreg filament,” *J. Mater. Sci.*, vol. 53, no. 3, pp. 1–12, 2017.

[48] T. H. J. Vaneker, “Material Extrusion of Continuous Fiber Reinforced Plastics Using Commingled Yarn,” *Procedia CIRP*, vol. 66, pp. 317–322, 2017.

[49] J. Justo, L. Távara, L. García-Guzmán, and F. París, “Characterization of 3D printed long fibre reinforced composites,” *Compos. Struct.*, vol. 185, no. October 2017, pp. 537–548, 2018.

[50] M. Eichenhofer, J. C. H. Wong, and P. Ermanni, “Continuous lattice fabrication of ultra-lightweight composite structures,” *Addit. Manuf.*, vol. 18, pp. 48–57, 2017.

[51] M. Eichenhofer, J. C. H. Wong, and P. Ermanni, “Exploiting cyclic softening in continuous lattice fabrication for the additive manufacturing of high performance fibre-reinforced thermoplastic composite materials,” *Compos. Sci. Technol.*, vol. 164, no. March, pp. 248–259, 2018.

[52] Z. Hou, X. Tian, J. Zhang, and D. Li, “3D printed continuous fibre reinforced composite corrugated structure,” *Compos. Struct.*, vol. 184, no. July 2017, pp. 1005–1010, 2018.

[53] G. W. Melenka, B. K. O. Cheung, J. S. Schofield, M. R. Dawson, and J. P. Carey, “Evaluation and prediction of the tensile properties of continuous fiber-reinforced 3D printed structures,” *Compos. Struct.*, vol. 153, pp. 866–875, 2016.

[54] F. Van Der Klift, Y. Koga, A. Todoroki, M. Ueda, Y. Hirano, and R. Matsuzaki, "3D Printing of Continuous Carbon Fibre Reinforced Thermo-Plastic (CFRTP) Tensile Test Specimens," *Open J. Compos. Mater.*, vol. 06, no. 01, pp. 18–27, 2016.

[55] A. N. Dickson, J. N. Barry, K. A. Mcdonnell, and D. P. Dowling, "Fabrication of continuous carbon , glass and Kevlar fibre reinforced polymer composites using additive manufacturing," *Addit. Manuf.*, vol. 16, pp. 146–152, 2017.

[56] M. A. Caminero, J. M. Chacón, I. García-Moreno, and G. P. Rodríguez, "Impact damage resistance of 3D printed continuous fibre reinforced thermoplastic composites using fused deposition modelling," *Compos. Part B Eng.*, vol. 148, no. March, pp. 93–103, 2018.

[57] X. Tian, T. Liu, C. Yang, Q. Wang, and D. Li, "Interface and performance of 3D printed continuous carbon fiber reinforced PLA composites," *Compos. Part A Appl. Sci. Manuf.*, vol. 88, pp. 198–205, 2016.

[58] X. Tian, T. Liu, Q. Wang, A. Dilmurat, D. Li, and G. Ziegmann, "Recycling and remanufacturing of 3D printed continuous carbon fiber reinforced PLA composites," *J. Clean. Prod.*, vol. 142, pp. 1609–1618, 2017.

[59] C. Yang, X. Tian, T. Liu, Y. Cao, and D. Li, "3D printing for continuous fiber reinforced thermoplastic composites: mechanism and performance," *Rapid Prototyp. J.*, vol. 23, no. 1, pp. 209–215, 2017.

[60] G. D. Goh *et al.*, "Characterization of mechanical properties and fracture mode of

additively manufactured carbon fiber and glass fiber reinforced thermoplastics," *Mater. Des.*, vol. 137, pp. 79–89, 2018.

[61] MATWEB, "Material properties by MATWEB," 2017. [Online]. Available: http://www.matweb.com.

[62] D. Jiang and D. E. Smith, "Anisotropic mechanical properties of oriented carbon fiber filled polymer composites produced with fused filament fabrication," *Addit. Manuf.*, vol. 18, pp. 84–94, 2017.

[63] M. Ivey, G. W. Melenka, J. P. Carey, and C. Ayranci, "Characterizing short-fiber-reinforced composites produced using additive manufacturing," *Adv. Manuf. Polym. Compos. Sci.*, vol. 0340, no. June, pp. 1–11, 2017.

[64] ASTM, "Astm D3039/D3039M," *Annu. B. ASTM Stand.*, pp. 1–13, 2014.

[65] J. L. Thomason and M. A. Vlug, "Influence of fibre length and concentration on the properties of glass fibre-reinforced polypropylene: 1. Tensile and flexural modulus," *Compos. Part A Appl. Sci. Manuf.*, vol. 27, no. 6, pp. 477–484, 1996.

[66] ASTM Standard, "Standard Test Methods for Flexural Properties of Unreinforced and Reinforced Plastics and Electrical Insulating Materials 1," pp. 1–11, 2017.

[67] Q. Wu, R. Zhao, Q. Liu, T. Jiao, J. Zhu, and F. Wang, "Simultaneous improvement of interfacial strength and toughness between carbon fiber and epoxy by introducing amino functionalized ZrO2on fiber surface," *Mater. Des.*, vol. 149, pp. 15–24, 2018.

[68] M. Li, X. Yin, X. Zhou, and Q. Lin, "Surface treatment of single sisal fibers with

bacterial cellulose and its enhancement in fiber-polymer adhesion properties," *Compos. Interfaces*, vol. 6440, pp. 1–15, 2018.

[69] S. S. Rangaraj and S. B. Bhaduri, "A modified rule-of-mixtures for prediction of tensile strengths of unidirectional fibre-reinforced composite materials," *J. Mater. Sci.*, vol. 29, no. 10, pp. 2795–2800, 1994.

[70] S. Ahn, M. Montero, D. Odell, S. Roundy, and P. K. Wright, "Anisotropic material properties of fused deposition modeling ABS," *Rapid Prototyp. J.*, vol. 8, no. 4, pp. 248–257, 2002.

[71] G. W. Melenka, J. S. Schofield, M. R. Dawson, and J. P. Carey, "Evaluation of dimensional accuracy and material properties of the MakerBot 3D desktop printer," *Rapid Prototyp. J.*, vol. 21, no. 5, pp. 618–627, 2015.

[72] K. Álvarez, R. F. Lagos, and M. Aizpun, "Investigating the influence of infill percentage on the mechanical properties of fused deposition modelled ABS parts," *Ing. e Investig.*, vol. 36, no. 3, p. 110, 2016.

[73] G. J. Turvey, "CFRP stiffened GFRP continuous beams – A simple closed-form analysis and its experimental verification for serviceability limit deformations," *Compos. Struct.*, vol. 153, pp. 952–960, 2016.

[74] T. W. Forest and E. P. Lozowski, "Estimating marine icing on offshore structures using RIGICE04 NRC Publications Archive (NPArC) Archives des publications du CNRC (NPArC) Estimating marine icing on offshore structures using RIGICE04

Forest , T . W .; Lozowski , E . P .; Gagnon , R . E," no. May, 2014.

[75] E. M. Samuelsen, K. Edvardsen, and R. G. Graversen, "Modelled and observed sea-spray icing in Arctic-Norwegian waters," *Cold Reg. Sci. Technol.*, vol. 134, pp. 54–81, 2017.

[76] S. R. Dehghani, G. F. Naterer, and Y. S. Muzychka, "Droplet size and velocity distributions of wave-impact sea spray over a marine vessel," *Cold Reg. Sci. Technol.*, vol. 132, pp. 60–67, 2016.

[77] M. Mohseni and A. Amirfazli, "A novel electro-thermal anti-icing system for fiber-reinforced polymer composite airfoils," *Cold Reg. Sci. Technol.*, vol. 87, pp. 47–58, 2013.

[78] C. Antonini, M. Innocenti, T. Horn, M. Marengo, and A. Amirfazli, "Understanding the effect of superhydrophobic coatings on energy reduction in anti-icing systems," *Cold Reg. Sci. Technol.*, vol. 67, no. 1–2, pp. 58–67, 2011.

[79] Z. Zhao, H. Chen, X. Liu, H. Liu, and D. Zhang, "Development of high-efficient synthetic electric heating coating for anti-icing/de-icing," *Surf. Coatings Technol.*, vol. 349, no. March, pp. 340–346, 2018.

[80] Y. Ibrahim, A. Elkholy, J. S. Schofield, and R. Kempers, "Effective thermal conductivity of continuous fiber polymer composites," *Adv. Manuf. Polym. Compos. Sci. (Under Prep.*, 2019.

[81] A. E. M. Rouby, R. Kempers, "Experimental and Numerical Investigation of

Anisotropic Thermal Conductivity of Additively Manufactured Components by Fused Deposition Modeling," *Prog. Addit. Manuf. (under Rev.*, 2019.

[82] "ASTM C177, Standard Test Method for Steady-State Heat Flux Measurements and Thermal Transmission Properties by Means of the Guarded-Hot-Plate, ASTM Int. (2013) 1–23. doi:10.1520/C0177-13.2."